

Stephen F. Austin State University

SFA ScholarWorks

Electronic Theses and Dissertations

Spring 5-13-2017

Gravitational Study of the Hastings Salt Dome and Associated Faults in Brazoria and Galveston Counties, Texas

Francis C. Okocha

Stephen F. Austin State University, okochofrancis@yahoo.com

Follow this and additional works at: <https://scholarworks.sfasu.edu/etds>



Part of the [Geology Commons](#), [Geomorphology Commons](#), [Geophysics and Seismology Commons](#), and the [Tectonics and Structure Commons](#)

[Tell us](#) how this article helped you.

Repository Citation

Okocha, Francis C., "Gravitational Study of the Hastings Salt Dome and Associated Faults in Brazoria and Galveston Counties, Texas" (2017). *Electronic Theses and Dissertations*. 80.

<https://scholarworks.sfasu.edu/etds/80>

This Thesis is brought to you for free and open access by SFA ScholarWorks. It has been accepted for inclusion in Electronic Theses and Dissertations by an authorized administrator of SFA ScholarWorks. For more information, please contact cdsscholarworks@sfasu.edu.

Gravitational Study of the Hastings Salt Dome and Associated Faults in Brazoria and Galveston Counties, Texas

Creative Commons License



This work is licensed under a [Creative Commons Attribution-Noncommercial-No Derivative Works 4.0 License](https://creativecommons.org/licenses/by-nc-nd/4.0/).

GRAVITATIONAL STUDY OF THE HASTINGS SALT DOME AND
ASSOCIATED FAULTS IN BRAZORIA AND GALVESTON COUNTIES,
TEXAS

By

FRANCIS CHIEDU OKOCHA, BS

Presented to the Faculty of the Graduate School of
Stephen F. Austin State University

In Partial Fulfillment
Of the Requirements

For the Degree of
Master of Science

STEPHEN F. AUSTIN STATE UNIVERSITY

May, 2017

GRAVITATIONAL STUDY OF THE HASTINGS SALT DOME AND
ASSOCIATED FAULTS IN BRAZORIA AND GALVESTON COUNTIES,
TEXAS

FRANCIS CHIEDU OKOCHA, BS

APPROVED:

Dr. Wesley Brown, Thesis Director

Dr. Chris Barker, Committee Member

Dr. R. LaRell Nielson, Committee Member

Dr. Walter L. Trikosko, Committee Member

Richard Berry, D.M.A

Dean of the Graduate School

ABSTRACT

Salt domes are important geological structures because they are potential major hydrocarbon traps and have a profound effect on overlying strata in the subsurface. Over five hundred salt domes have been located on the United States Gulf Coast region, including the Hastings Salt Dome. Hastings Oil Field is located about 40.2 km (25 miles) southeast of Houston, Texas. The Hasting oil field was discovered in 1934 and it was considered the largest oil reserve on the Gulf Coast. Its peak production of 75,000 BOPD (barrels of oil per day) was recorded in 1977 and it had a cumulative production of 582 MMBO (million barrels of Oil) as at February 2011.

Gravity surveying is a geophysical method of investigating subsurface features based on differences in rock densities. This is carried-out by using a gravimeter, which is an instrument that measures variations in gravitational attraction over the surface of the earth. Five hundred and thirty-seven gravity readings (including base station readings) were collected along roads and accessible routes in the study area by using a CG-5 Scintrex Autograv Gravimeter. Gravity readings were collected at every one-third to one-fourth of a mile. The CG-5 Autograv instrument measures relative gravity readings of the earth's gravitational fields.

Geographical coordinates for each of the gravity station was determined with the aid of a Trimble NOMAD GPS unit. A Digital Elevation Model over the study area was

generated from LiDAR data and this provided elevation values for each gravity stations. These elevation values were used for elevation corrections (free-air correction and Bouguer correction), which is an important aspect of gravity correction in creation of a Bouguer Anomaly map. Bouguer Anomaly reveals lateral variation in density of rocks at the subsurface. Two oval gravity low anomalies were found and interpreted as Hastings and Manvel Salt Domes. Data retrieved from the Texas Natural Resources Information System database revealed a series of normal faults within the area of the Hastings Salt Dome. Well log correlation, application of the concept of creekology, and a detailed gravity study accurately revealed the location and other physical characteristics of the Hastings Salt Dome. Well log correlation also revealed evidence of uplift of the overlying sedimentary beds over the Hastings Salt Dome. The flow pattern of the Clear Lake creek over Hastings Salt Dome supports the evidence of the presence of a subsurface feature. The Digital Elevation Model revealed surface imprints (isolated highs) associated with the presence of Blue Ridge, Pierce Junction and Webster salt domes but this was not observed over the Hastings Salt Dome.

This study will ultimately lead to a better understanding of the size, geometry, depth and structure of the Hastings Salt Dome.

ACKNOWLEDGEMENT

I am thankful to God, my family and friends for their prayers and supports. I thank Mrs. Vera for her support during field work and data collection phase of this research.

I also thank my adviser, Dr. Wesley Brown, and my thesis committee members. I am grateful to the Geology Department Scholarship Committee at Stephen F. Austin State University for providing funds for logistics during the research. To the entire faculty and staff of the SFA geology department who has made my period of study indeed a wonderful one.

DEDICATION

This thesis research is dedicated to my family “THE GREAT OKOCHAS” for your care, concern, sacrifice, love and prayers. I would not have achieved this goal without you. I am grateful.

TABLE OF CONTENTS

ABSTRACT.....	iii
ACKNOWLEDGEMENT	v
DEDICATION	vi
LIST OF FIGURES	x
LIST OF EQUATIONS	xvi
LIST OF TABLES.....	xvii
INTRODUCTION	1
HASTINGS OIL FIELD.....	4
STUDY OBJECTIVES.....	6
LITERATURE REVIEW	7
TECTONIC EVOLUTION AND REGIONAL STRUCTURAL SETTINGS.....	7
REGIONAL STRATIGRAPHIC SETTINGS OF THE GULF COAST	12
PALEOZOIC SYSTEM OF THE GULF COAST	15
TRIASSIC SYSTEM OF THE GULF COAST.....	15
JURASSIC SYSTEM OF THE GULF COAST	15
CRETACEOUS SYSTEM OF THE GULF COAST	16
TERTIARY SYSTEM OF THE GULF COAST.....	17

LOUANN SALT.....	19
ROCK SALT AND TYPES OF SALT DOME STRUCTURES	20
FAULT STRUCTURES ASSOCIATED WITH SALT DOMES	26
ECONOMIC SIGNIFICANCE OF ROCK SALTS AND SALT DOMES.....	27
SUBSIDENCE.....	30
OBSERVATIONS FROM SUBSIDENCE DATA	31
GRAVITY THEORY	36
LAWS AND PRINCIPLES	36
GRAVITY CORRECTIONS APPLIED	37
METHODOLOGY	46
INSTRUMENTATION	46
SOFTWARE	50
DATA COLLECTION AND DATA PROCESSING	51
GRAVITY FIELD SURVEY	51
ELEVATION DATA.....	57
MAGNETIC DATA	59
SATELLITE IMAGERY	60
WELL LOGS	61

RESULTS AND INTERPRETATION.....	66
ELEVATION.....	66
GRAVITY MAPS.....	71
MAGNETIC ANOMALY MAP	88
WELL LOG INTERPRETATION	91
ESTIMATING THE DEPTH TO HASTINGS SALT DOME.....	97
CREEKOLOGY	98
GRAVITY MODEL	105
DISCUSSION AND CONCLUSION.....	115
LIMITATIONS.....	118
FUTURE WORK.....	119
CITATIONS	120
APPENDIX A – GRAVITY DATASET FOR STUDY AREA.....	126
APPENDIX B – PACES GRAVITY DATASET IN NAD 83.....	141
APPENDIX C – PACES MAGNETIC DATASET	154
VITA.....	160

LIST OF FIGURES

- Figure 1 - Location of study area on the Gulf Coastal Plain of Texas (Study area in red rectangle).3
- Figure 2 - Map of Harris county area showing the approximate location of salt domes. Data on salt dome locations from two sources; 2004 salt dome shapefile (Lopez, 1995; Ewing and Lopez, 1991; Martin, 1980) and 1984 salt dome shapefile (Martin, 1980) modified from Zheng et al., 2011) 5
- Figure 3 - (From top to bottom, left to right) Early Triassic (245 Ma) shows after the assemblage of Pangea, Late Jurassic (150 Ma) shows the opening of the Atlantic Ocean due to the break-up of Pangea. This process led to the formation of the GOM in the late Triassic, Paleogene (~ 35 Ma) shows after the Rocky Mountain was formed from Laramide Orogeny, Pleistocene (~ 12 – 15 Ka) shows the present day North American plate and the GOM. *Source: Ron Blakey* 8
- Figure 4 - Structural settings and features of the Gulf of Mexico. Some structural features peculiar to study area include: (18) Rio Grande embayment (19) San Marcos arch (20) East Texas basin and (21) Sabine uplift (from Salvador, 1991)..... 9
- Figure 5 – Diagram showing the cross section along the central part of Texas Gulf coast and northern Gulf of Mexico basin showing depositional and structural styles (Bruce, 1973; Solis, 1981). It shows generally gulfward thickening of sedimentary beds..... 11
- Figure 6- Stratigraphic Column of Gulf Coastal Plain of Texas (modified from Baker, 1995). Highlighted in red rectangle is the stratigraphic sequence peculiar to study area. 13
- Figure 7- Continuation of Stratigraphic Column of Gulf Coastal Plain of Texas (modified from Baker, 1995). Highlighted in red rectangle is the stratigraphic sequence peculiar to study area. 14
- Figure 8 - Schematic illustration of a salt dome and its relationship with surrounding rocks; a potential source for oil and gas, limestone, gypsum, anhydrite and Sulphur (from Martinez, 1991)..... 22
- Figure 9 - The Structural Evolution and different types of salt structures formed during salt diapirism (modified from Jackson and Talbot, 1986)..... 23

Figure 10 - Diagrammatic illustration of salt dome classification based on piercement and depth of burial (from Halbouty, 1976). Salt dome are classified into shallow, intermediate, and deep seated based on their depth of burial.	25
Figure 11 - Development of graben structure over salt dome. Slide A indicated a simple dome, Slide B indicates a growing dome creating a simple offset fault, Slide C indicates the formation of simple graben and slide D shows the formation of a complex graben (from Halbouty, 1976).	29
Figure 12 - Google earth imagery showing the spatial distribution PAM's GPS used in monitoring of rate of subsidence in Gulf Coast of Texas. PAM 21 and PAM 33 (identified by brown stars) lies within the study area. Data collected from Harris-Galveston Subsidence District database.....	33
Figure 13 - A regression plot of rate of subsidence measured in PAM 21 and PAM 33 from the year 2003 to 2016. Data from PAM site 21 shows that an average subsidence rate of 0.24 cm / year occurred, while PAM site 33 shows an average subsidence rate of 0.3 cm / year occurred, <i>Source: http://mapper.subsidence.org/Chartindex.htm</i>	34
Figure 14 - Contour lines represent the amount of subsidence that occurred from 1906 - 1987 in Harris and Galveston regions in Texas (modified from Zilkoski et al., 2003). Study area highlighted in red rectangle.	35
Figure 16 – A graph showing gravity values (mGal) against time (sec) for instrument drift calibration. This graph shows a linear trend of gravity measured to determine the drift co-efficient, which is applied automatically by the software to correct for the effect of drift on to gravity values measured.....	41
Figure 15 - (left to right) (a) Top view of CG-5 Scintrex Autograv (b) displaying field set-up of the CG-5 gravity meter before gravity measurement is taken. Gravity meter is mounted on a tripod which comes with a rotating foot screw used for adjusting for tilt. When adjusted within a range of ± 10 arcsec a cross hair and an icon is displayed as shown in figure 15a.	40
Figure 17 – (left to right) (a) A display of the Trimble Nomad GPS Unit; (b) display of GPS unit used in acquiring geographic coordinates for a gravity station in the field.	48
Figure 18 – Shows the spatial distribution of the 537 gravity readings (red and yellow circles) that was collected in the field and the location of the absolute gravity base station located in south-west of Harris County. The red circle represents the first phase gravity dataset collected between 5/7 to 6/4 and was restricted to Brazoria and Galveston Counties, while	

the yellow circle represents the second phase of gravity dataset collected between 07/17 to 8/24.	54
Figure 19 - Absolute Gravity Base Station database containing pre-established absolute gravity readings at different location. Highlighted in red rectangle is the closest to the study area and also, it is an open access absolute gravity base station. This location was used to tie all 537 gravity readings that were collected in the field. Data source: Internationale Gravimetric Bureau (retrieved August, 2016).	55
Figure 20 – Showing the location and the absolute gravity base station readings closest to the study area and located SW Houston as represented by the red star in Figure 18. Data source: Internationale Gravimetric Bureau (retrieved August, 2016).....	56
Figure 21 - Gravity data points overlain on DEM and the elevation value assigned to the pixel is obtained. These elevation values is recorded and used for elevation correction. Gravity data point highlighted in light blue circle displays the elevation values assigned to the pixel where the gravity station intersects with the DEM. The elevation value for the highlight gravity station represented with a blue circle 10.8 meters. The DEM was generated from LiDAR dataset over the study area.	58
Figure 22 - Structural map of Frio Formation at Hasting Oil Field Yellow dash lines represent the north-west trending normal fault that divides the oil field into two arms; Hastings West (left) and Hastings East (right) Oil Fields. There are also series of minor southwest to northeast trending normal faults (modified from Thomas, 1953).	63
Figure 23 – Cross-section of well-to-well correlation of well logs data. Study area in black rectangle. <i>www.gpsvisualizer.com</i> . Well #1 (Pierce Junction), #2 (Hastings), #3 (Manvel), #10 (Danbury), and #11(Danbury) are associated with the presence of salt domes, while well #4, #5, and #6 are located in Hastings Oil Field.	64
Figure 24 – A regional ETOPO1 elevation map extracted from NOAA database (Amante and Eakins, 2009). Elevation high values are observed in the northwest portion with gradual decrease in elevation values towards the Gulf of Mexico in a southeast trend. Study area highlighted in black rectangle.	68
Figure 25 – ETOPO1 elevation map (study area) extracted from NOAA database (Amante and Eakins, 2009). Elevation high values of 21.9 meters are located to the west and decreasing in a south-east direction at a minimum value of 5 meters.	69

Figure 26 - Elevation map from gravity data collected from the field. Elevation high values of 18.4 meters observed in the west and lowest elevation of 5.5 meters at the southeast of study area.	70
Figure 27 - Observed gravity map created from corrected gravity data collected in the field. High gravity values at 979280.1mGal are observed at the northern portion and gradually decreasing towards the southwest portion with gravity low values at 979259.3mGal.	73
Figure 28 - Observed gravity map of Houston area created from gravity data collected from PACES database. Gravity high values of 3303 mGal are observed at the northeast which gradually decreases in a southwest direction and a gravity low value of 3256.1 mGal. Black rectangle shows the extent of the study area and 42 gravity data points lies within it.	74
Figure 30 - Theoretical gravity map from gravity data collected from the field. High gravity values at 97998.2mGal are observed at the north and gradually decreases towards the southwest with a gravity low of 979269.8 mGal.	76
Figure 31- Theoretical gravity map of Houston area created from gravity data collected from the PACES database. Gravity high values at 981064.8 mGal observed at north portion and decreases gradually southwards with a gravity low at 980969.7 mGal. Black rectangle shows the extent of the study area.	77
Figure 32 - Residual Gravity Anomaly created from field gravity data. Gravity low anomaly values of -21.7 mGal at northcentral and west portions which decreasing southwards with a gravity high anomaly values of -9.9 mGal at southeast of the study area.....	79
Figure 33 - Free Air Gravity Anomaly map shows a gravity low anomaly values of -18.4 mGal at the northeast and increasing in a southeast direction to a gravity high anomaly values of -6.6 mGal of the study area.	80
Figure 34 - Simple Bouguer Anomaly map created from gravity dataset collected from the field. Gravity low anomaly values range between -24.9 mGal to -23.5 mGal are observed at north-central and west portions of the study area. This has been interpreted as the Hastings and Manvel Salt Dome respectively.	83
Figure 35 - Complete Bouguer Anomaly map of Houston area created from the PACES gravity dataset. Black rectangle shows extent of study area and black circles represent gravity stations used to create the map. Note the widely spaced gravity reading between gravity stations.	85

Figure 36 - A zoomed-in view of the oval shaped, gravity low anomaly which has been interpreted as the Hastings Salt Dome. Also shown is the uneven distribution of density within the Hastings Salt Dome.	86
Figure 37 – Showing the simple Bouguer Anomaly map overlain on county and road network shapefiles using ArcGIS 10.3. It shows that the Hastings Salt Dome is located at the border between Harris and Brazoria Counties, while the Manvel Salt Dome is located in Brazoria County. The Hastings Oil Field as represented by the georeferenced structural map is located to the south-eastern flank of the Hastings Salt Dome.	87
Figure 38 – The total Magnetic Intensity map of Texas showing the distribution of magnetic anomalies. Black arrow shows the approximate location of the study area. Magnetic dataset is extracted from the PACES database. The geosyncline is located to the southeast of the map and represented by an eastward trending magnetic anomaly.	89
Figure 39 - Total Magnetic Intensity map of study area. High magnetic values at -240.8 nT are observed at the north and gradually decreases southwards, and an abrupt magnetic low at the southeast at value of -417.1 nT is observed. Black circles represent magnetic data and spacing.	90
Figure 40 – Stratigraphic correlation map showing correlated Frio and Miocene Shale. In well #2, the interval sedimentary beds in between the Miocene and Frio Shales show evidence of sediment compaction. This observation can explain for subsidence within this region. Cross section can be found in Figure 20.	94
Figure 41 - Structural map of the top of the Frio Shale shows a south-eastern ward increase and maximum depth of 6,300 feet in well #9. Generally, depth of the Frio Shale is increasing towards the Gulf.	95
Figure 42 - Isopach map shows the distribution of thickness of the Frio Shale. Well # 4 shows the least thickness of approximately 540 feet, while the maximum thickness occurred at well #8 with a thickness of 1,950 feet south-east of study area.	96
Figure 43 - Land Cover map showing high concentration of urban settlement to the north and north-east, and more agricultural activities in the south and southwest. Study area highlighted in red rectangle.	102
Figure 44 - Digital Elevation Model showing the distribution of elevation. The creeks are controlled by the general topography of the region. Study area highlighted in red rectangle.	103

- Figure 45 – Showing the local effect of the presence of the salt dome and relative to the flow pattern of the creeks around the salt domes. To the west of the Study area, the Dickinson bayou responds to the presence of the Manvel Salt Dome by wrapping around it. The Clear Creek flow can be seen flowing across the Hastings Salt Dome but wraps around it towards the east portion of the salt dome. Study area in red rectangle. 104
- Figure 46 – Three cross sections A-A' (Hastings Salt Dome, B-B' (Manvel Salt Dome) and C-C' were drawn and used to create the hypothetical gravity models. The fault shapefile extracted, lies within Hastings Salt Dome and these faults are normal faults. 108
- Figure 47 – A 2D hypothetical gravity model of cross section A-A' shows that the Hastings Salt Dome has an asymmetric geometry. The Hastings Salt Dome is bounded by series of normal faults (in black broken lines) which cuts across the Cretaceous and Tertiary layers. Gulf-ward dipping of Quaternary and Tertiary layers in a south-east direction is observed. Vertical Exaggeration is 0.89 110
- Figure 48 – A 2D hypothetical gravity model of cross-section B-B' shows that the Manvel Salt Dome has a near symmetric geometry. The Manvel Salt Dome is a diapiric type of salt structure and it is a deep seated salt dome at a depth of 4,285 meters. 112
- Figure 49 – A 2D hypothetical gravity model of cross section C-C' shows salt withdrawal process west-wardly (represented by black arrow direction) and resulting in a significant thinning of the Jurassic salt layer. The overlying Cretaceous, Tertiary and Quaternary rock layers shows thickening towards the east of the model. This observation supports for the process of sediment differential loading. 114

LIST OF EQUATIONS

1.	$F = \frac{Gm_1m_2}{r^2}$	36
2.	$G_n = 978032.68 \frac{(1+0.00193185138639\sin^2\phi)}{\sqrt{(1-0.00669437999013\sin^2\phi)}} mGal$	42
3.	<i>Free Air Correction FAC = 0.3086 h</i>	43
4.	<i>Free Air Anomaly FAA = G_{obs} – G_n + FAC</i>	44
5.	<i>Bouguer Correction = 0.04193ρh</i>	44
6.	<i>Elevation Correction = 0.3086 – 0.04193ρh mGal</i>	45
7.	$BA = G_{obs} - (G_n \pm FAC \pm BC)$	81
8.	$BA = G_{obs} - G_{corrected}$	81
9.	$z = 1.305x^{1/2}$	97

LIST OF TABLES

Table 1 - Well Log Data obtained from Texas Railroad Commission.	65
Table 2 - Formations in Harris County and its vicinity with assigned density values (From Murray, 1961; Meyer, 1939).....	107

INTRODUCTION

The study area is located on the Gulf Coastal Plain of Texas and is approximately 680 km². It extends from southeast Houston to north-east of Brazoria and northwest of Galveston County along state Highway 35 in Texas (Figure 1). The region is generally characterized by flat to low relief topography. The average elevation is 12 meters and the study area is approximately 76 km from the Gulf of Mexico coastline. The climate of the study area is humid subtropical.

Gravity surveying is a passive, geophysical method used for investigating subsurface structural features based on differences in rock densities. This is done using a gravimeter, which is an instrument that measures variations in the earth's gravitational pulls at the earth's surface. Five hundred and thirty-seven gravity readings (including base station readings) were collected in the field with a CG-5 Scintrex Autograv Gravimeter. The gravity data were corrected for elevation and latitude effects to produce a simple Bouguer Anomaly Map of the study area. Geosoft OASIS Montaj version 9.0 was used to create grid maps that represent the data and a GM-SYS model was used to create 2D hypothetical geological models that depict the subsurface geology based on gravity and magnetic response. Salt domes show gravity low anomalies relative to the rocks around and over them. This is due to the density contrast between salt and other types of rocks in the subsurface. Additional gravity and magnetic data were obtained from PACES database (Pan American Center for Earth and Environmental Studies) at the

University of Texas at El Paso, UTEP. These gravity data were used for comparison with field data, while the magnetic data was used as an additional control measure for the 2D hypothetical gravity model. A gravity survey is based on the variation of naturally occurring gravitational fields of the earth from one point to another; hence, it is a passive measurement. The gravitational attraction of low-density rocks in the subsurface will respond to gravitational attraction differently from a higher density rock. Salt domes are low-density rocks and they retain their characteristic rock density even when subjected to burial at depth. The gravity survey was successfully used in identifying the presence of a salt dome in the subsurface.

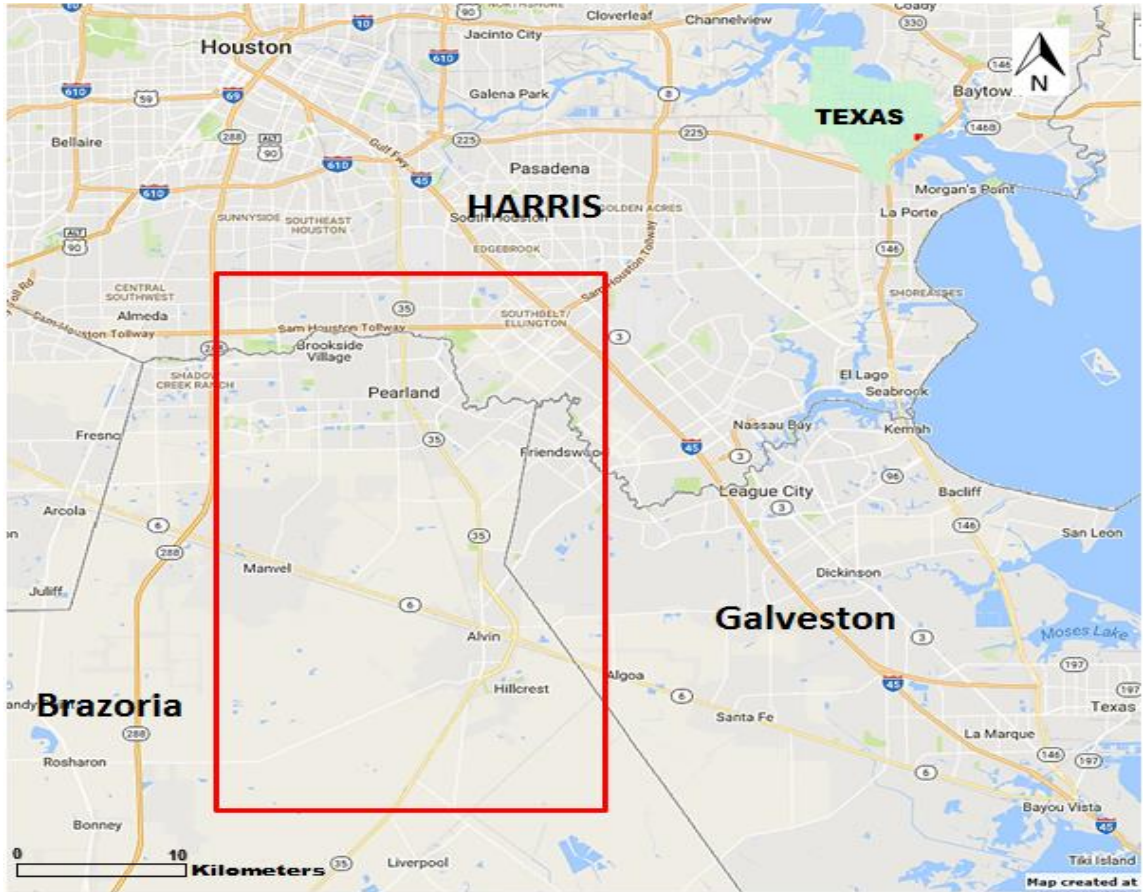


Figure 1 - Location of study area on the Gulf Coastal Plain of Texas (Study area in red rectangle).

HASTINGS OIL FIELD

Hastings Oil Field is located on the Gulf Coastal Plain of Texas and it is 40.2 km (25 miles) to the southeast of Houston on the Highway 35 in Texas (Figure 2). The Hastings Oil Field is located to the northeast of Brazoria County and northwest of Galveston County. Hastings Oil Field was discovered in December 23, 1934 by Stanolind Oil and Gas Company. The Hastings Oil Field reached its peak production in the year 1977 with an oil production output of 75,000 BOPD (barrels of oil per day) and a cumulative oil production of 582 MMBO (million barrels of Oil) as at February 2011 (Denbury, 2011). The main production zone in the Hastings Oil Field (reservoir rock) is the Frio Sandstone of the Frio Formation at a depth range of 1,640 meters (5,390 feet) to 2,080 meters (6,840 feet) in L.F McKibben "A" No. 6 (Thomas, 1953). The Hastings Oil Field has well counts of 80 producers, 5 water injectors, 6 CO₂ injectors, and 3 SWD (Salt Water Disposal) (Denbury, 2011). On February 2009, the Hastings Oil Field was acquired from Venoco Incorporated by Denbury (present oil field operator). Denbury Resources Incorporation is an independent oil and gas company, which uses CO₂ Enhanced Oil Recovery (CO₂ EOR) method to reactivate oil production from matured and depleted reservoirs. CO₂ EOR is a tertiary oil recovery method and it can increase recoverability of original oil in place by 50% - 60%.

Thomas (1953) described the structure of the Hastings Oil Field as a roughly circular and deep-seated body, which is intersected by a northwest trending normal fault with a maximum throw of 210 meters (700 feet).

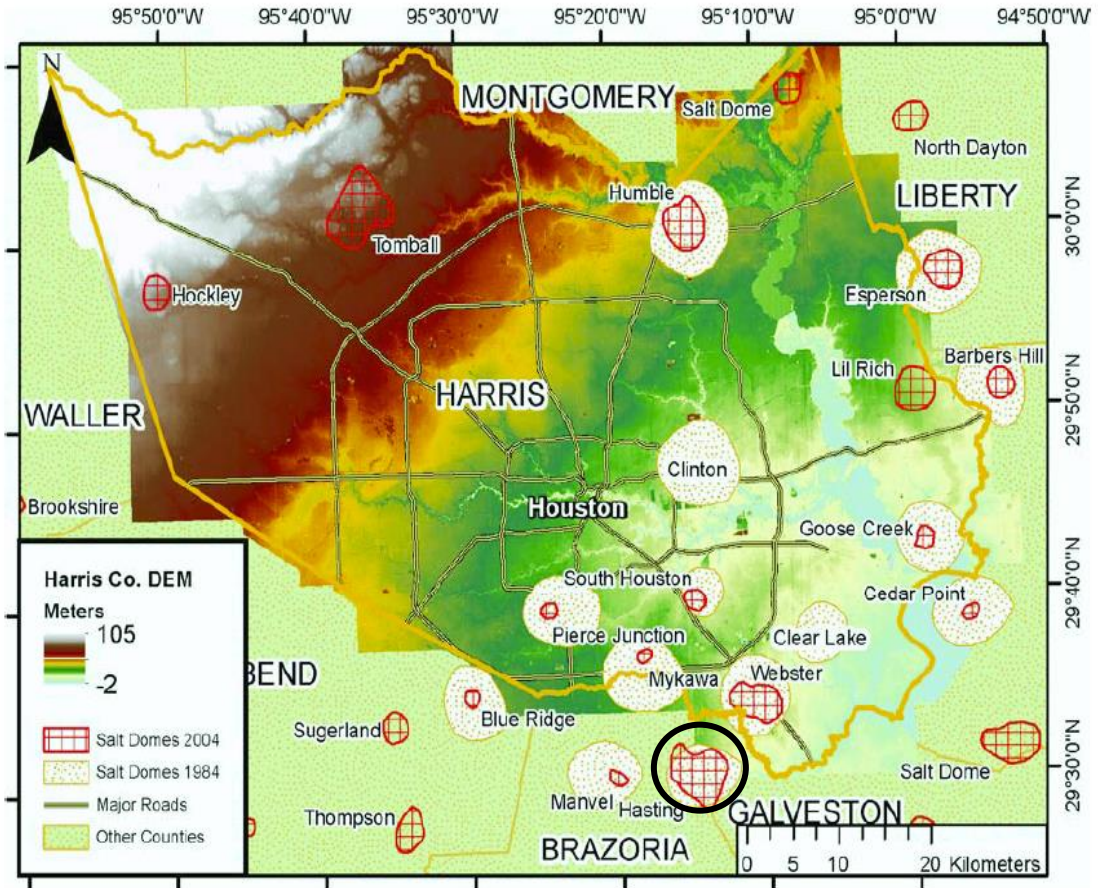


Figure 2 - Map of Harris County area showing the approximate location of salt domes. Data on salt dome locations from two sources; 2004 salt dome shapefile (Lopez, 1995; Ewing and Lopez, 1991; Martin, 1980) and 1984 salt dome shapefile (Martin, 1980) modified from Zheng et al., 2011). Highlighted in black circle is the location of Hastings Salt Dome as represented by the above data sources.

STUDY OBJECTIVES

Using gravity survey method, this thesis aims to address the objectives below;

1. To apply and evaluate the use of gravity techniques in investigating subsurface features based on their densities e.g. salt domes.
2. To determine and resolve the location and geometry of the Hastings Salt Dome and to confirm its relationship with Hastings Oil Field.
3. To generate a Bouguer Anomaly map and a 2D hypothetical gravity model that depicts the subsurface geology.
4. To analyze the effect of salt diapirism as it relates to uplifts and subsidence around Hastings Salt Dome.
5. To investigate surface features associated with salt diapirism by applying the concept of creekology and by using remote sensing techniques.

LITERATURE REVIEW

TECTONIC EVOLUTION AND REGIONAL STRUCTURAL SETTINGS

The initial stage of the Gulfian tectonic cycle began during the early Mesozoic Era (late Triassic) about 220 mya, when the European and African-South American plate (Gondwana) collided with North American plate (Byerly, 1991) (Figure 3). This collision led to the formation of the Ouachita Mountains and it was at this time that most of the development of the coastal plain of Texas began. The Gulf of Mexico Basin was formed by downfaulting and downwrapping of the Paleozoic basement rocks during the break-up of Pangaea as a result of the opening of the North Atlantic Ocean in the late Triassic (Byerly, 1991; Hosman & Weiss, 1991). The Gulf of Mexico basin began to form because of the rifting of the Yucatan microplate and the North American plate during the Triassic – early Cretaceous (Hudec et al., 2013) (Figure 3). During the Cenozoic time, the present day Brazoria and Galveston counties were depressed to a depth of about 9,100 to 10,600 meters (Meyer, 1939).

The major structural features in the Gulf Coastal Plain that have influenced changes in facies are: East Texas Basin, Sabine Uplift and Houston Embayment (east coastal plain); San Marcos Arch (Central Coastal plain); and Rio Grande Embayment (south coastal plain) (Figure 4). The San Marcos Arch divides the Houston Embayment from the Rio Grande Embayment.

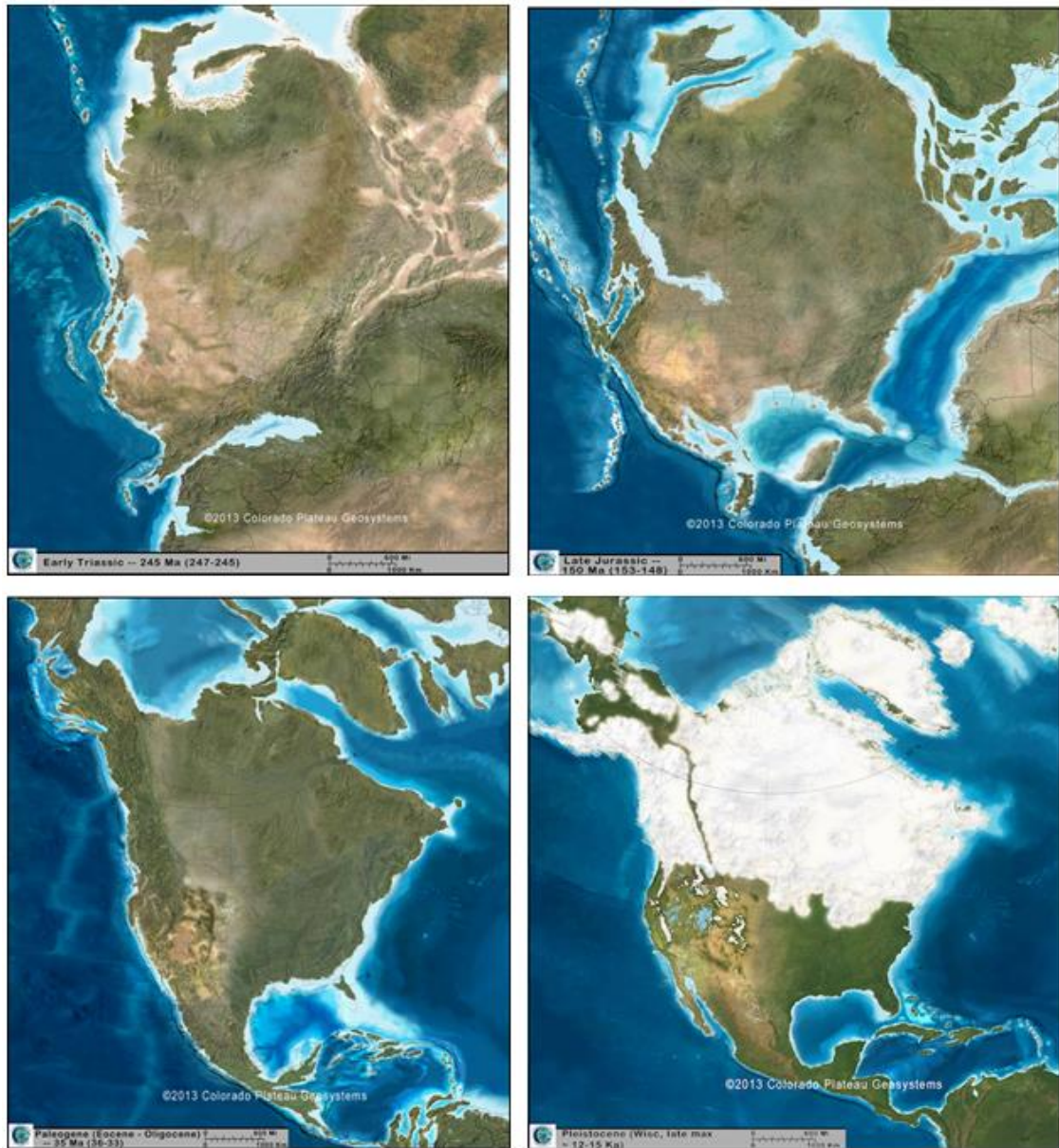


Figure 3 - (From top to bottom, left to right) Early Triassic (245 Ma) shows after the assemblage of Pangea, Late Jurassic (150 Ma) shows the opening of the Atlantic Ocean due to the break-up of Pangea. This process led to the formation of the Gulf of Mexico in the late Triassic, Paleogene (~ 35 Ma) shows after the Rocky Mountain was formed from Laramide Orogeny, Pleistocene (~ 12 – 15 Ka) shows the North American plate and the Gulf of Mexico which is similar to present day. *Source: Ron Blakey*

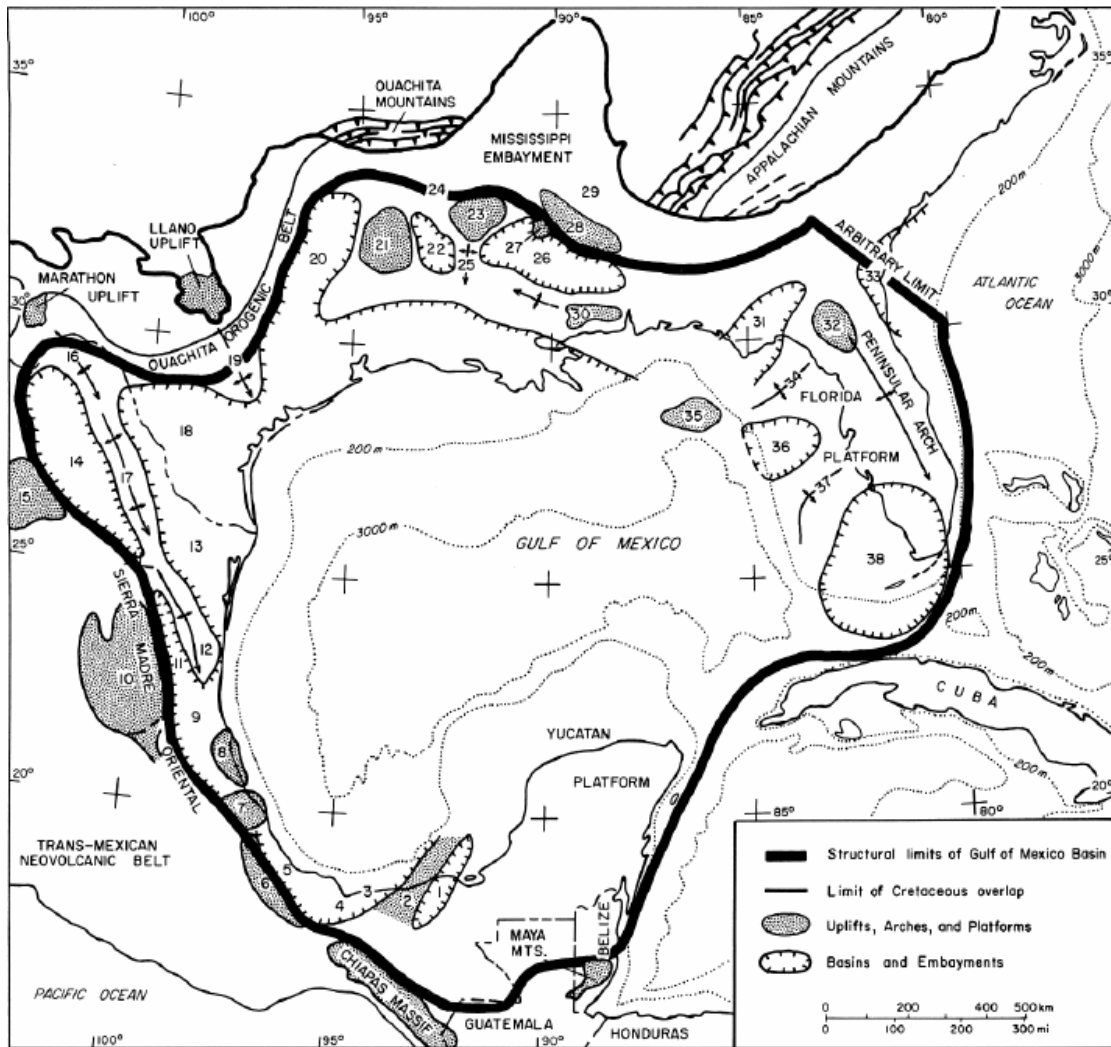


Figure 4 - Structural settings and features of the Gulf of Mexico. Some structural features peculiar to study area include: (18) Rio Grande embayment (19) San Marcos arch (20) East Texas basin and (21) Sabine uplift (from Salvador, 1991).

The study area (south Harris, north-east of Brazoria, and north-west of Galveston) lies within the Houston Embayment (Figure 4). The deposition of Callovian Louann Salt of Jurassic age was caused and followed by crustal extension over a lengthy period. This tectonic activity resulted in the thinning and wide distribution of the salt (Hudec et al, 2013). The results of this process lead to the distribution and formation of the Hastings Salt Dome and other identified salt bodies in the Gulf coast and its vicinity.

Meyer (1939) observed that the angle of dip of sediments in the southern part of Harris county was greater than that observed in the north of Harris County. This regional dip was observed to extend adjacent to the coastal shore line in the eastern part of Texas and into Louisiana. The sudden increase in regional dip and the thickness of the sediments suggested the presence of a geosyncline (Figure 5). The geosyncline is characterised as an extra-cratonic basin that was formed under conditions of rapid subsidence and was accompanied by intensified sediment loading (Galloway, 1982). Bornhauser (1958) suggested that most regional structures, embayments, arches and flexes in the Gulf Coast were created by a combination of differential subsidence of the basin floor and thick sediment that flowed as viscous fluids on sloping surfaces. These structural features control sediment accumulation patterns and the bedding planes thin towards and over the arches and are thickest in the embayment (Grubb, 1998) (Figure 5). The geosyncline is a depocenter which is filled with sediments in an elongate depression of the earth's surface (Meyer, 1939) (Figure 5).

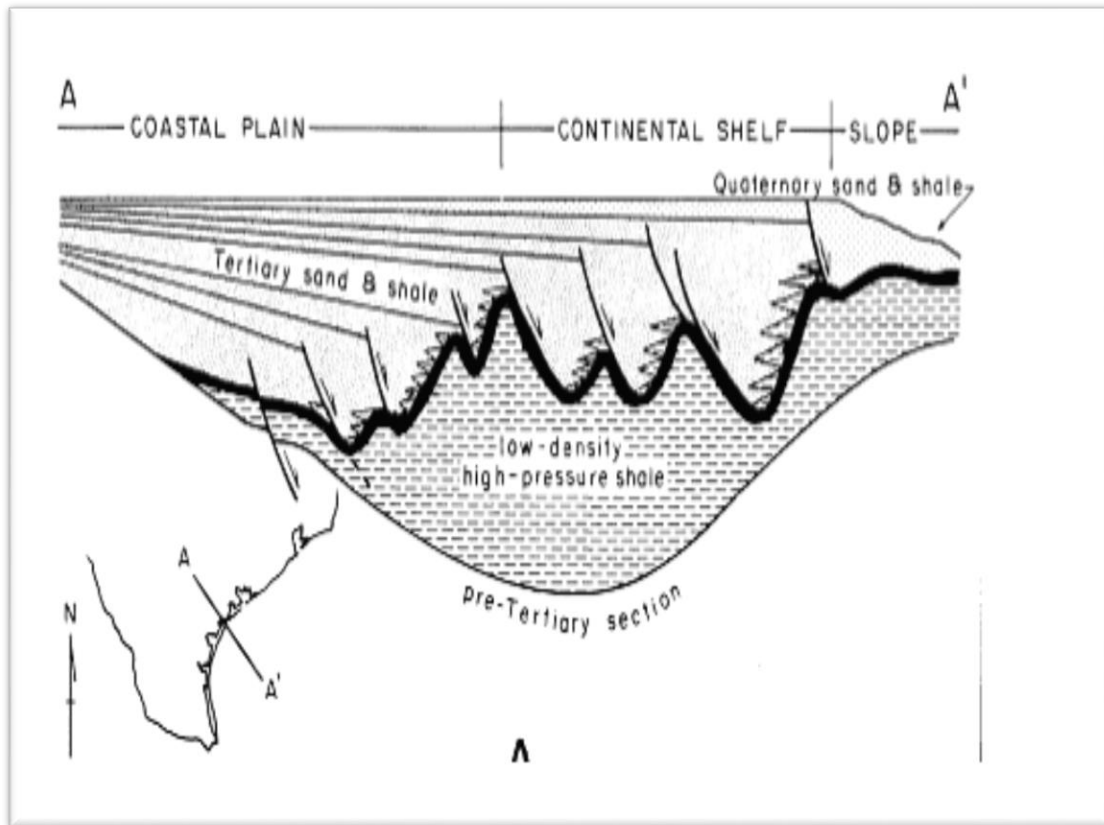


Figure 5 – Diagram showing a cross section along the central part of the Texas Gulf Coast and northern Gulf of Mexico basin showing depositional and structural styles (Bruce, 1973; Solis, 1981). It shows generally Gulf-ward thickening of sedimentary beds.

REGIONAL STRATIGRAPHIC SETTINGS OF THE GULF COAST

The stratigraphic units of the Gulf Coastal Plains are mostly Mesozoic and Cenozoic age, plus sediments from the quaternary system in the upper parts. Underlying all are deformed Paleozoic rocks of Ouachita facies (Baker, 1995) (Figure 6 and Figure 7). The sedimentary rocks of Mesozoic and Cenozoic age in the Gulf Coastal plain of Texas and near the coastline are estimated to be between thickness of 15,200 to 18,200 meters (50, 000 - 60, 000 feet) (Baker, 1995).

Global fluctuations of sea level coincided with cyclic deposition sequences in the Mesozoic and Cenozoic sedimentary rocks of the Gulf Coastal region (Murray, 1961). Pigott and Bradley (2014) observed that the Oligocene to Miocene sedimentary rocks at the northern margin of the Gulf Coast of Texas correspond to a third order global sea level cycle and a half, which consists of three limbs. This cycle began with a Rupettian global sea level rise, which was recorded by the Vicksburg formation as well as thousands of feet of under-compacted slope and basinal mudstone (Pigott & Bradley, 2014). This cycle was followed by a Chattian global sea level fall, which was recorded by the Frio Formation, and characterized by fluvial-deltaic deposit (Galloway, 1982). This cycle ended with an Aquitanian global sea level rise, which was recorded by the transgressive marine Anahuac Shale (Lawless et al., 1997). The stratigraphic section of the northern Gulf of Mexico is discussed based on major geologic systems.

ERA	SYSTEM	SERIES	SW	SE	SW	SE	SW	SE	
			SOUTH COASTAL PLAIN (includes Rio Grande embayment)		CENTRAL COASTAL PLAIN (includes San Marcos arch)		EAST COASTAL PLAIN (includes East Texas Basin, Sabine uplift, and Houston embayment)		
CENOZOIC	Quaternary	Holocene	Alluvium		Alluvium		Alluvium		
		Pleistocene	Beaumont Formation		Beaumont Formation		Beaumont Formation		
			Lissie Formation	Lissie Formation	Montgomery Formation	Lissie Formation	Montgomery Formation		
					Bentley Formation	Bentley Formation			
		Willis Sand	Willis Sand	Willis Sand					
	Tertiary	Pliocene	Goliad Sand		Goliad Sand		Goliad Sand		
		Miocene	Fleming Formation		Fleming Formation		Oakville Sandstone	Fleming Formation	
			Oakville Sandstone		Oakville Sandstone			Fleming Formation	
			Catahoula Tuff	Upper part of Catahoula Tuff	Catahoula Tuff or Sandstone	Upper part of Catahoula Tuff or Ss.	Catahoula Sandstone	Upper part of Catahoula Ss.	
				Anahuac Formation		Anahuac Formation		Anahuac Formation	
		Frio Formation	Frio Formation	Frio Formation	Frio Formation				
		Oligocene	Frio Clay	Vicksburg Fm. (subsurface)	Frio Clay	Vicksburg Fm. (subsurface)	Vicksburg Fm. (subsurface)		
			Jackson Group	Jackson Group	Whitsett Fm. Manning Clay Wellborn Ss. Caddell Fm.	Jackson Group	Jackson Group		
		Eocene	Chalbarne Group	Yegua Formation		Yegua Formation		Yegua Formation	
				Laredo Formation	Cook Mountain Fm.	Cook Mountain Formation		Cook Mountain Formation	
					Sparta Sand	Sparta Sand		Sparta Sand	
				El Pico Clay	Weches Formation	Weches Formation		Weches Formation	
					Queen City Sand	Queen City Sand		Queen City Sand	
			Bigford Formation	Reklaw Formation	Reklaw Formation		Reklaw Formation		
			Wilcox Group	Carrizo Sand		Carrizo Sand		Carrizo Sand	
Indio Formation	Calvert Bluff Formation			Calvert Bluff Formation		Calvert Bluff Formation			
	Simsboro Formation			Simsboro Formation		Simsboro Formation			
	Hooper Formation		Hooper Formation		Hooper Formation				
Paleocene	Midway Group		Midway Group		Midway Group				
MESOZOIC	Cretaceous	Gulfian	Navarro Group	Escondido Formation	Escondido Formation	Kemp Clay	Kemp Clay		
				Olmos Formation	Olmos Formation	Corsicana Marl	Corsicana Marl		
			Nacatoch Sand	Nacatoch Sand	Neylandville Marl	Neylandville Marl			
		Taylor Marl	Upper part Taylor Marl	Upper part Taylor Marl		Upper part Taylor Marl			
			San Miguel Formation	Anacacho Limestone	Anacacho Limestone	Pecan Gap Chalk	Pecan Gap Chalk	Annona Chalk	
Wolfe City Sand	Wolfe City Sand								
Upson Clay	Lower part Taylor Marl	Lower part Taylor Marl		Lower part Taylor Marl					

Figure 6- Stratigraphic Column of Gulf Coastal Plain of Texas (modified from Baker, 1995). Highlighted in red rectangle is the stratigraphic sequence relevant to the study area.

ERA	SYSTEM	SERIES	SW	SE	SW	SE	SW	SE				
			SOUTH COASTAL PLAIN (Includes Rio Grande embayment)		CENTRAL COASTAL PLAIN (Includes San Marcos arch)		EAST COASTAL PLAIN (Includes East Texas Basin, Sabine uplift, and Houston embayment)					
MESOZOIC—Continued	Cretaceous—Continued	Gulfian—Continued	Austin Group		Austin Group		Austin Group	Gober Chalk Brownstown Marl Blossom Sand Bonham Marl Ector Tongue Sub-Clarksville Sc				
			Eagle Ford Shale		Eagle Ford Shale		Eagle Ford Shale					
			Woodbine Sand		Woodbine Sand		Woodbine Sand	Maness Shale				
		Comanchean	Fredericksburg Group	Washita Group	Buda Limestone		Buda Limestone		Buda Limestone			
					Del Rio Clay		Del Rio Clay	Grayson Marl	Grayson Marl			
				Georgetown Ls.	Salmon Peak Formation	Georgetown Ls.	Person Formation	Georgetown Limestone	Georgetown Limestone	Main Street Limestone Pawpaw Formation Waco Clay Denison Clay Fort Worth Limestone Duck Creek Formation		
					McKnight Formation	Regional Dense Member	Person Formation	Regional Dense Member	Kamichi Formation	Kamichi Formation		
				Fredericksburg Group	West Nueces Formation	Kainer Formation	Kainer Formation	Edwards Limestone	Edwards Ls.	Goodland Ls.		
					Edwards Group	Edwards Group	Edwards Group	Edwards Group	Edwards Group	Edwards Group		
				Trinity Group	Trinity Group	Trinity Group	Paluxy Sand		Paluxy Sand		Paluxy Sand	Mooringsport Fm.
							Glen Rose Limestone		Glen Rose Limestone		Glen Rose Limestone	Ferry Lake Anhydrite Rodeasa Fm.
							Pearsall Formation	Hensell Sh. Mbr. Cow Creek Ls. Mbr. Pine Island Sh. Mbr.	Pearsall Formation	Hensell Sh. Mbr. Cow Creek Ls. Mbr. Pine Island Sh. Mbr.	Pearsall Formation	Hensell Sh. Mbr. James Ls. Mbr. Pine Island Sh. Mbr.
							Comanche Peak Ls.	Keys Valley Marl Mbr. Cedar Park Mbr. Bee Cave Mbr.	Comanche Peak Ls.	Keys Valley Marl Mbr. Cedar Park Mbr. Bee Cave Mbr.	Comanche Peak Ls.	Walnut Fm.
		Coahuilan	Amarillo Group	Silgo Formation		Silgo Formation		Silgo (Pettit) Formation				
				Houston Formation		Houston Formation		Houston Formation				
Jurassic	Upper Jurassic	Cotton Valley Group		Cotton Valley Group	Schuler Formation Boesler Formation	Cotton Valley Group	Schuler Formation Boesler Formation					
		Gilmer Limestone		Gilmer Limestone		Gilmer Limestone						
		Buckner Formation		Buckner Formation		Buckner Formation						
		Smackover Formation		Smackover Formation		Smackover Formation						
	Norphlet Formation		Norphlet Formation		Norphlet Formation							
	Louann Salt		Louann Salt		Louann Salt							
	Werner Formation		Werner Formation		Werner Formation							
Triassic	Upper Triassic	Eagle Mills Formation		Eagle Mills Formation		Eagle Mills Formation						
PALEOZOIC		Ouachita facies		Ouachita facies		Ouachita facies						

Figure 7- Continuation of Stratigraphic Column of Gulf Coastal Plain of Texas (modified from Baker, 1995). Highlighted in red rectangle is the stratigraphic sequence relevant to the study area.

PALEOZOIC SYSTEM OF THE GULF COAST

In the pre-Triassic period, during the Cambrian-Ordovician, the north rim of the Gulf Coast Basin, Llanoria-Appalachian, was a passive landmass with carbonate deposit (Rainwater, 1967). Foote et al. (1988), observed the presence of clay and fine grained sands in sediments of Mississippian age and that the sediments became coarser in size as it transits to the Pennsylvanian aged rocks (Foote et al., 1988).

TRIASSIC SYSTEM OF THE GULF COAST

In the Triassic period, the present-day Gulf of Mexico was basically a stretched pseudo-continent crust (Walper and Miller, 1985), with sediment (Sand, Gravel, red shale) in a seaward propagation sequence derived from uplifted rock and deposited as Eagle Mill Formation (Foote et al., 1988) (Figure 7).

JURASSIC SYSTEM OF THE GULF COAST

The first marine incursion from the Pacific into the incipient Gulf of Mexico basin occurred during late Triassic and early Jurassic (Walper and Miller, 1985). By mid-Jurassic period, the first transgression of highly saline marine water deposited a marine sequence (Foote et al., 1988). The Louark Group signifies the end of evaporite precipitation indicated by an unconformity that denotes marginal uplift and subsequent

erosion (Nichols, 1964) (Figure 7). The depositional environment of Norphlet Formation ranges from uplands to fluvial floodplains (Newkirk, 1971). An influx of marine water resulted in deposition of marine sediments of the Smackover Formation, which represents the first marine transgression of the north Gulf Coast (Walper and Miller, 1985). The deposition of Smackover Formation experienced two separate sedimentological sea level regimes resulting in the lower unit of the Smackover Formation having a source rock characteristic, and the upper unit having reservoir rock characteristics. The upper unit is comprised of organically rich clay and dolomite beds of packstone and grainstone sizes respectively (Presley & Reed, 1984). The Cotton Valley Group represents a shift from carbonate sedimentary rocks units of the Haynesville Formation to clastic sedimentary rock of the Bossier Formation (Foote et al, 1988). The shales of the Bossier Formation mark the boundary between Jurassic and lower Cretaceous sedimentary units (Braunstein et al., 1988) (Figure 7).

CRETACEOUS SYSTEM OF THE GULF COAST

As a result of the uplift and then erosion of the Ouachita tectonic belt, silicate clastic sediments were deposited as delta plain, alluvial plain, shallow to deep marine, and transitional environment as Hosston and Travis Peak Formation in the East Texas Basin (Bushaw, 1968). Towards the interior of the basin, progradation of the deltaic system produced a younger depocenter. Rodessa sediments deposited on the Sabine Uplift are sub-divided from oldest to youngest into: Young, Dees, Mitchell, Gloyd, and

Hill Formation (Bushaw, 1968). Calcarenite, dolomite, limestone reefs, and shell mounds were deposited in carbonate environments around the East Texas Basin. The Rusk and Glen Rose formations of East Texas signifies a major withdrawal of sea water level and this led to the deposition of the overlying Paluxy Formation (Nichols, 1964). Sediments of the Gulfian Series of the Cretaceous rest on an up-dip area and in a low angular unconformity with Comanchean, Coahulian, Jurassic and older rocks within the Gulf Coast region. The Gulfian Series is divided into Woodbine, Eagle Ford, Austin Chalk, Taylor, and the Navarro group (Figure 6 and Figure 7).

TERTIARY SYSTEM OF THE GULF COAST

This period recorded a major regression of the Gulf of Mexico between the Paleocene – Eocene with some widespread transgression (Foote et al, 1988). The facies of the fluvial system of the Wilcox Group are alternating sandstone, siltstone and shale, which were deposited in an alluvial transitional, shallow marine environment. In the Claiborne Group, three major marine transgressions took place in the Eocene (Rainwater, 1967), which began with the deposition of Carrizo and Reklaw Formation (Foote et al., 1988) (Figure 6). The Jackson Group was deposited during the Oligocene and this marks the last deposition of the Tertiary period sediments in a fluvial and deltaic depositional environment (Bushaw, 1968). Frio Formation strata consist of ashy clays, sandy and silty clays and sandstone with a marine and non-marine environment of deposition (Meyer, 1939). The Frio clay in the eastern and central parts of the Texas Coastal Plains is

characterized by a light green color appearance with some minute amount of red and gray clays. The Frio Sandstone of the central and eastern part of Texas coastal plain was deposited by south flowing streams. Sand grain sizes are angular to sub-angular with glassy luster (Meyer, 1939). Sandstones in the up-dip part of the Frio formation occur in lenses with individual thickness of sands ranging from a few inches to over 30 meters (100 feet) (Meyer, 1939). The Frio strata dominate the Paleogene Gulf in volume and rate of sediment input (Galloway, 2005).

The Frio Sandstone is the main reservoir rock for petroleum exploration in the Gulf Coastal Plain of Texas. In the Hastings Oil Field, hydrocarbon is extracted from the upper Frio Sandstone occurring at a varying depth of 1,500 meters to 1,800 meters and separated by a shale layer of 76 meters (Thomas, 1953). The Frio Sandstone formation is characterized by grain size of fine-medium and underlain by the Vicksburg shale (Thomas, 1953) (Figure 6). Thomas (1953) interpreted a north-west trending and north-east dipping normal fault. This fault has a displacement of about 210 meters (700 feet) in the Hastings Oil Field. The lateral continuity of the Frio Sandstone (reservoir rock) in the Hastings Oil Field is abruptly interrupted by a series of smaller faults (Thomas, 1953). The upper and lower Frio Sandstone are productive in the up-thrown southwest segments but at the northeastern segment of the oil field, only the upper Frio reservoir is productive (Thomas, 1953).

Regional studies of the Gulf Coast indicate that Mesozoic and Cenozoic deposits in the geosyncline accumulated in an arcuate belt of varying thicknesses along the Gulf of Mexico continental borders (Murray, 1961) (Figure 5). The cyclic depositional

sequences in the Mesozoic and Cenozoic coastal province coincide with the widespread fluctuation of sea level, resulting in natural divisions of Mesozoic and Cenozoic strata (Murray, 1961).

LOUANN SALT

The Jurassic Louann Salt is referred to as the “mother bed” and the source of all salt domes and salt structures in the Gulf Coast Basin. An initial average thickness of the Louann salt, when it was precipitated, is estimated to be approximately 1,500 meters (5,000 feet) (Parker and McDowell, 1955). The Louann Salt is of mid-Jurassic age and it is part of the evaporite sequence of the Gulf Coastal Basin. The ages of underlying and overlying rock formations were used to estimate the age of the Louann Salt because the evaporite lacked fossils. The Louann Salt unconformably overlies Paleozoic sequences and is overlain unconformably by the Norphlet and Smackover Formations of Upper Jurassic age (Bushaw, 1968). Warren (2006) suggested that the Louann Salt was formed from rich saline marine water which was isolated from the open ocean; under favorable climate conditions and latitude, it became saline enough to deposit halite.

Salt domes form both structural and stratigraphic traps for oil and gas accumulation. The formation of salt domes often causes the development of faults as the salt migrates vertically upwards. This upward migration is caused by the following factors: buoyancy of salt to be mobilized, gravity spreading of the thick salt mass basin-

ward, differential sediment loading (prograding deltaic sand on pro-delta mud) and thermal convection (Jackson and Galloway, 1984; Williamson and Grubb, 2001).

ROCK SALT AND TYPES OF SALT DOME STRUCTURES

The Gulf of Mexico contains some of the most studied salt structures in the world (Worrall and Snelson, 1989). Over 500 identified salt domes exist on the Gulf Coastal Plains. Salt domes mostly consist of halite with minor traces of gypsum and/or anhydrite. Salt domes often form geologic structural traps for hydrocarbon accumulation and are often associated with formation of potash and sulphur (Jackson and Talbot, 1986) (Figure 8). Jackson and Talbot (1986) explained the effect of differential loading as a more effective salt diaper mechanism than buoyancy in the formation of salt domes, especially in its early stage. Differential loading as a result of sediment progradation has been proposed to be the major cause of the deformation of both autochthonous and allochthonous salt in the Gulf of Mexico Basin (Humphris, 1979).

Rock salt is generally mechanically weak and viscous, and when subjected to pressure, it is easily mobile in its solid state. The diffusive rate of a salt body depends on factors such as temperature, confining pressure and impurities such as water (Jackson and Talbot, 1986). When subjected to diagenetic processes, rock salt is almost incompressible throughout deposition, accumulation, burial and diagenetic stages, unlike other sedimentary rocks. Consequently, the average density of rock salt remains at about 2.1 g/cm³ throughout their changes, while sedimentary rocks increase in density due to

lithification, compaction and de-watering as it lithifies from sediments to sedimentary rocks. The low-density contrast of a salt body at the subsurface and relative to its surrounding rocks is a reason why the gravity survey method is suitable for salt dome prospecting. A salt dome is a subsurface structural feature that can occur at various depths as rock salt accumulates and then is displaced vertically upward to form a dome.

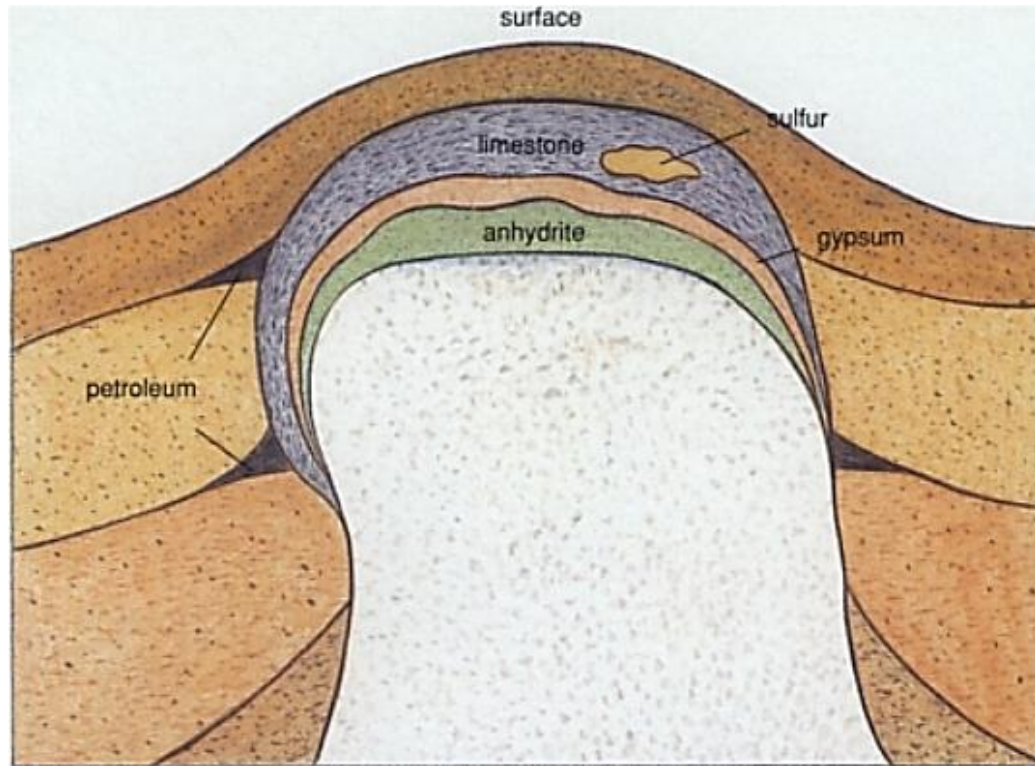


Figure 8 - Schematic illustration of a salt dome and its relationship with surrounding rocks. The dome is a potential source for oil and gas and sometimes is capped with limestone, gypsum, anhydrite and sulphur (from Martinez, 1991).

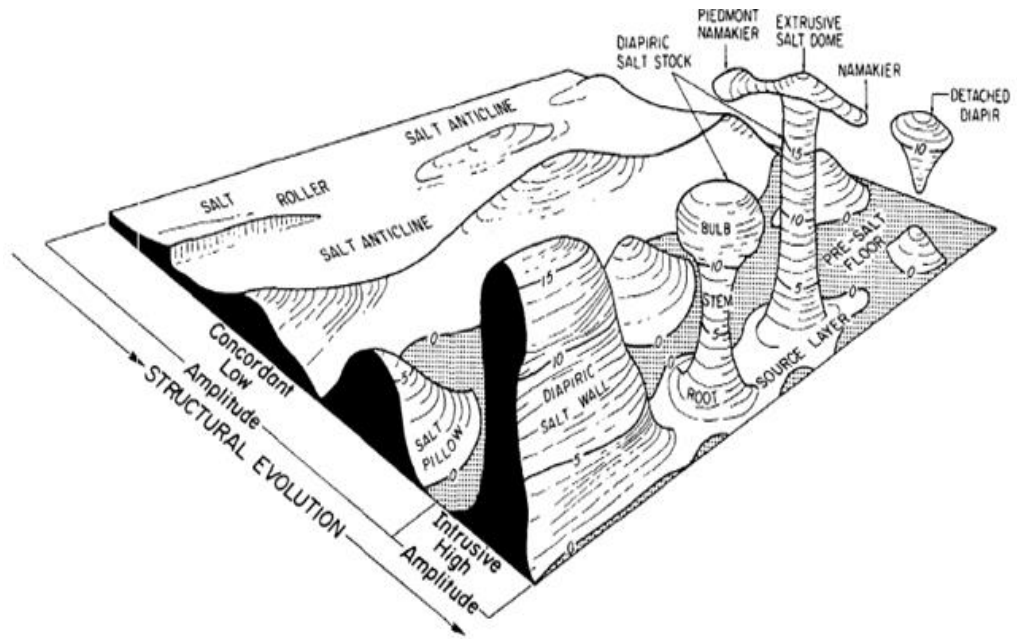


Figure 9 - Different types of salt structures, non-diapiric and diapiric (from Jackson and Talbot, 1986).

This is dependent on the degree of vertical movement of the salt, pressure of overlying denser rock acting vertically downwards and buoyancy of the salt layer being displaced. Subsurface salt structures are either: (i) diapiric, which is when a salt body pierces into the overlying surrounding rock (Figure 9), and (ii) non-diapiric, which is when a salt body lies conformably in contact with the overlying rock (O'brien, 1968). Diapiric salt intrusion results in the formation of different salt components such of salt wall, salt stock, salt nappes and detached tear drop-shaped diapir (Jackson and Talbot, 1986) (Figure 9). Salt buried at depth rises vertically upward to create diapirs that can be rod-like, domal, anticlinal, or ridge-like in form. During upward movement of salt, the surrounding sedimentary rocks are often disrupted by normal faults and some rare occurrences of reverse faults, which form a complex fault pattern over the salt body (Withjack and Schneiner, 1982) (Figure 11).

Halbouty (1976) classified salt domes based on their burial depth. Intrusive salt domes occurring from the surface to a depth of about 600 meters are classified as shallow salt domes, while those found at a depth of 600 – 1800 meters are classified as intermediate salt domes (Figure 10). Deep-seated salt domes occur at depths below 1800 meters (Halbouty, 1976). This classification applies to both diapiric and non-diapiric salt domes.

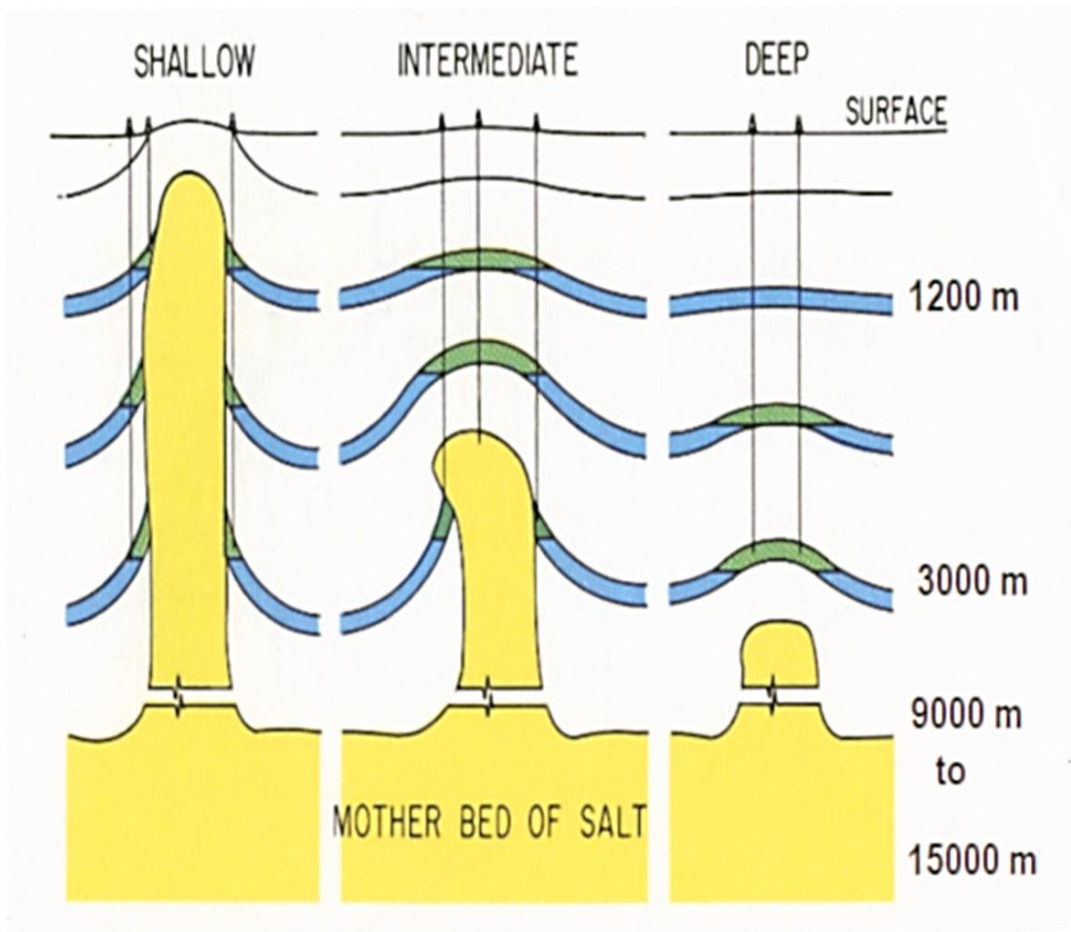


Figure 10 - Diagrammatic illustration of salt dome classification based on piercing and depth of burial. Salt dome are classified into shallow, intermediate and deep seated based on their depth of burial (from Halbouty, 1976).

FAULT STRUCTURES ASSOCIATED WITH SALT DOMES

Salt diapirism accounts for the formation of several hundred of salt domes in the Gulf Coast region and in similar areas, such as the Zechstein Basin of northwest Germany (Withjack and Schneiner, 1982). As an active diapir forcefully intrudes its overburden rocks, it gradually overcomes the resistance strength of the overburden rock layers (Schultz-Ela et al., 1993). A force balance of density contrast between rock salt and sedimentary rock overburden, demonstrates that, for an active and substantial diapirism to occur, the thickness of the salt layer must be more than two-third to three-quarter of the thickness of the surrounding overburden (Schultz-Ela et al., 1993).

Many faults form over salt domes (Figure 11). Two important factors that may influence the fault pattern are the outline and shape of the dome, and the presence of regional strain (either extension or compression) during diapirism (Withjack and Schneiner, 1982). Circular domes are characterized by more radial normal faults than elliptical domes especially on the crest of the dome. Most of the normal faults observed on the crest of elliptical domes trend parallel with the long axis of the salt body. Long and listric normal fault such as the Bancroft system of southern Texas and Louisiana, and the narrow graben Talco system of northern Texas also deformed the Gulf Coast sediments (Withjack and Schneiner, 1982) (Figure 11). The presence of normal faulting is evidence that most of the Gulf Coastal region experienced regional extension in the geological past (Closs, 1968), possibly contemporaneously with salt diapirism.

The outcome of an analytical and experimental model conducted by Withjack and Schneiner (1982) shows that doming was simultaneous to both compression and extensional regional strain. This regional strain significantly affected the fault patterns that were produced during the salt dome diapirism process. The study by Withjack and Schneiner (1982) also shows that, salt domes formed during regional extension develop several normal faults on the crest and flanks that are perpendicular to the extension direction; whereas, salt domes formed during regional compression, develop many normal faults on the crest and flanks which strike parallel to the compressional direction. An example is the Conroe dome of Montgomery County and Elk Basin dome from Rocky Mountains foreland (Withjack and Schneiner, 1982).

ECONOMIC SIGNIFICANCE OF ROCK SALTS AND SALT DOMES

Salt domes have economic values and are sometimes associated with one or more other rocks or minerals such as limestone, sulfur and gypsum, which can accumulate above the salt dome. (Martinez, 1991) (Figure 8). When all three substances are present, they typically occur in the order of limestone at the top, then gypsum, then anhydrite, and they form the cap rock (Figure 8). Most salt domes do not have any of these secondary minerals at all. The chemical composition of most Gulf Coast salt domes consists of mostly halite, often with some amount of calcium sulfate (CaSO_4) and gypsum ($\text{CaSO}_4 \cdot 2\text{H}_2\text{O}$) (Martinez, 1991). Calcite can form as a result of the conversion of calcium sulfate to carbonate with the assistance of bacteria, and gypsum is created by

percolation of water at the interface between limestone and anhydrite and it is probably the last mineral to be formed. Faulting and fracturing of the salt dome cap rock may create a migration path for mineral-rich fluids which are responsible for the formation of gypsum and limestone (Martinez, 1991). Economic concentrations of these minerals are mined above some salt domes.

Salt domes form anticlinal structural traps for hydrocarbon accumulation and are very often associated with faults (Figure 11).

Large caverns can form in salt domes when salt is leached out by groundwater. These caverns can be used as underground storage for hydrocarbon reserves. They are also proposed to be disposal sites for hazardous and radioactive wastes (Martinez, 1991). These large caverns are formed through salt cavern leaching or solution mining, which involves the injection of fresh water into salt dome in the subsurface. This process dissolves salt crystals and the solution is extracted and then pumped as brine water. This practice was permitted by the U.S Congress in 1970 and under the nation's Strategic Petroleum Reserve program (SPR) (Martinez, 1991). Examples are the West Hackberry site in Lake Charles, Louisiana and Pierce Junction south of Houston, Texas, which have storage capacities of 227 million barrels (Martinez, 1991) and 76 million barrels respectively.

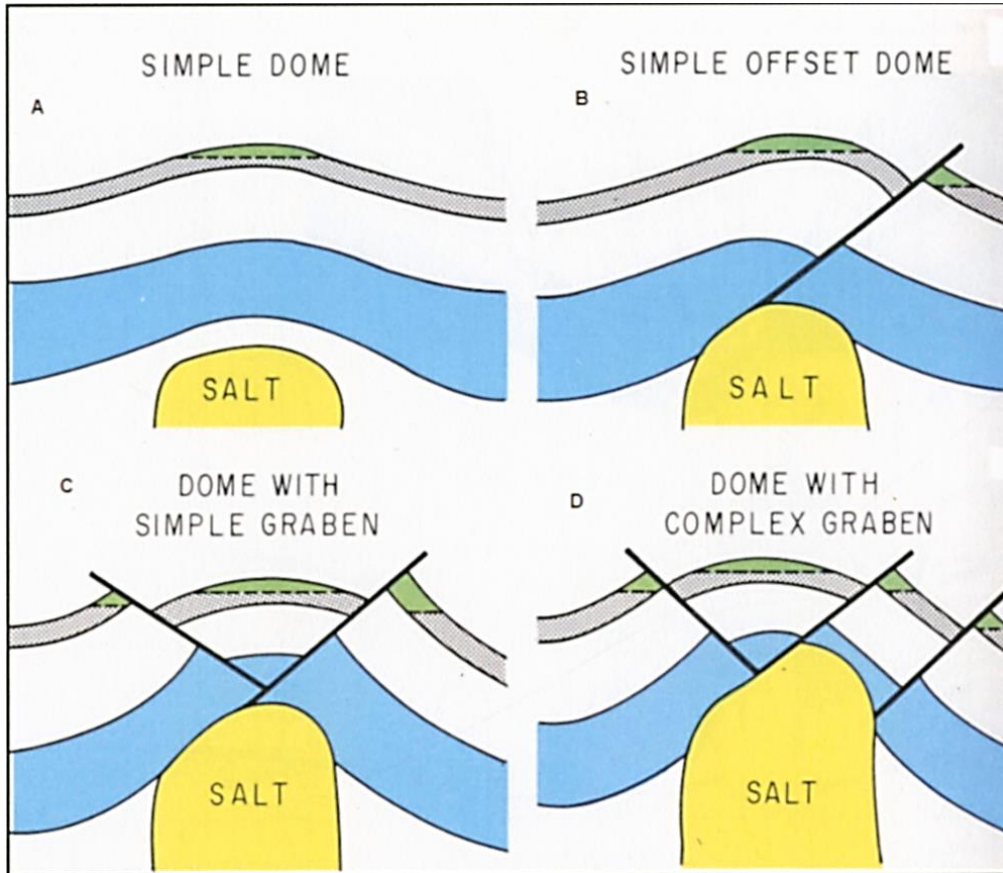


Figure 11 - Development of graben structure over a salt dome. Drawing A indicates a simple dome; Drawing B indicates a growing dome creating a simple offset fault; Drawing C indicates the formation of simple graben and Drawing D shows the formation of a complex graben (from Halbouty, 1976).

SUBSIDENCE

Land subsidence is the gradual lowering of the land surface due to removal or alteration of the subsurface support mechanism. Anthropogenic activities have been concluded to be the major cause of subsidence in the Houston-Galveston areas. Recent studies show that ground water withdrawal is a more significant contributing factor than the effect of oil and gas removal exploration activities to regional subsidence (Khan et al., 2014; Holzer and Bluntzer, 1984). Holzer and Bluntzer (1984) observed a decrease in thickness in the Evangeline aquifer toward the top of the Pierce Junction salt dome. The location was not affected by the regional subsidence observed in the region and relative to its surrounding. This observation led to the suggestion that the upward movement of the Pierce Junction salt dome acted as an additional support mechanism to offset the effect of subsidence. The large decline in reservoir pressure in oil fields was noted but there was not enough information about that due to the lack of data from early wells drilled (Holzer and Bluntzer, 1984).

Subsidence due to excessive ground water withdrawal can occur as a result of a decline in the potentiometric surface in an unconsolidated confined aquifer (Galloway et al, 1999). A decline in the potentiometric surface results in a decrease in hydraulic pressure. This process results in a re-stabilization of pressure in the subsurface (Galloway et al., 1999). Pressure equilibrium is easily attained in sand units, unlike the clay and silt

units, during the compaction and de-watering process. The amount of compaction of sediments is less in sand units as compared to clay and silt units (Galloway et al., 1999).

As of 1979, data collected from GPS Continuously Operating Reference Station (CORS) and GPS Port-A-Measure (PAM's) stations within the Houston and Galveston regions recorded subsidence of approximately 8,200 km² of the 28,400 km² of that area. The affected areas subsided more than 0.3 meters (Coplin and Galloway, 1999) as compared to data collected in 1943-1973, during which the same area subsided more than 0.15 meters (Gabrysch and Bonnet, 1975).

Rates of subsidence were calculated based on measurements taken from permanent stations such as local GPS Continuously Operating Reference Stations (CORS) and GPS Port-A-Measure (PAM's) in the Gulf Coast regions (Figure 12). Zilkoski et al., (2003) revealed that a monument northwest of downtown Houston is subsiding at a rate of 7cm/year.

OBSERVATIONS FROM SUBSIDENCE DATA

PAM and CORS stations monitor the effect and rate of groundwater withdrawal within the area where they are installed. This information is used to monitor the rate of subsidence by measuring groundwater level and rate of ground water withdrawal with the aid of GPS. PAM sites 21 and 33 are within the study area and are closest to Hastings Salt Dome and Hastings Oil Field respectively (Figure 12). This information was

extracted from the Harris-Galveston Subsidence District webpage;

<http://mapper.subsidence.org/Chartindex.htm>.

Subsidence data from PAM 21 (Figure 13) shows a decrease in groundwater level from approximately 0.015 meters to -0.030 meters (0.05 feet to -0.1 feet) from 2002 to 2016. A subsidence rate of 0.045 meters (0.15 feet) had occurred at approximately 0.3cm/year. Subsidence data from PAM 33 (Figure 13) shows a decrease in groundwater level from approximately -0.0060 meters to -0.030 meters (-0.02 feet to -0.1 feet) from 2007 to 2016. A rate of subsidence of 0.024 meters (0.08 feet) had occurred, which is approximately 0.24 cm / year. Zilkoski et al., (2003) created a regional contour map (Figure 14) representing the amount of subsidence that occurred from 1906 - 1987 in Harris and Galveston Counties in Texas. Highlighted in a red rectangle in Figure 14 is the present study area which shows that the location of PAM 21, closest to Hastings Salt Dome, subsided by 1.22 meters (4 feet), while the location of PAM 33, closest to the Hastings Oil field, subsided by 0.9 meters (3 feet) Zilkoski et al., (2003).

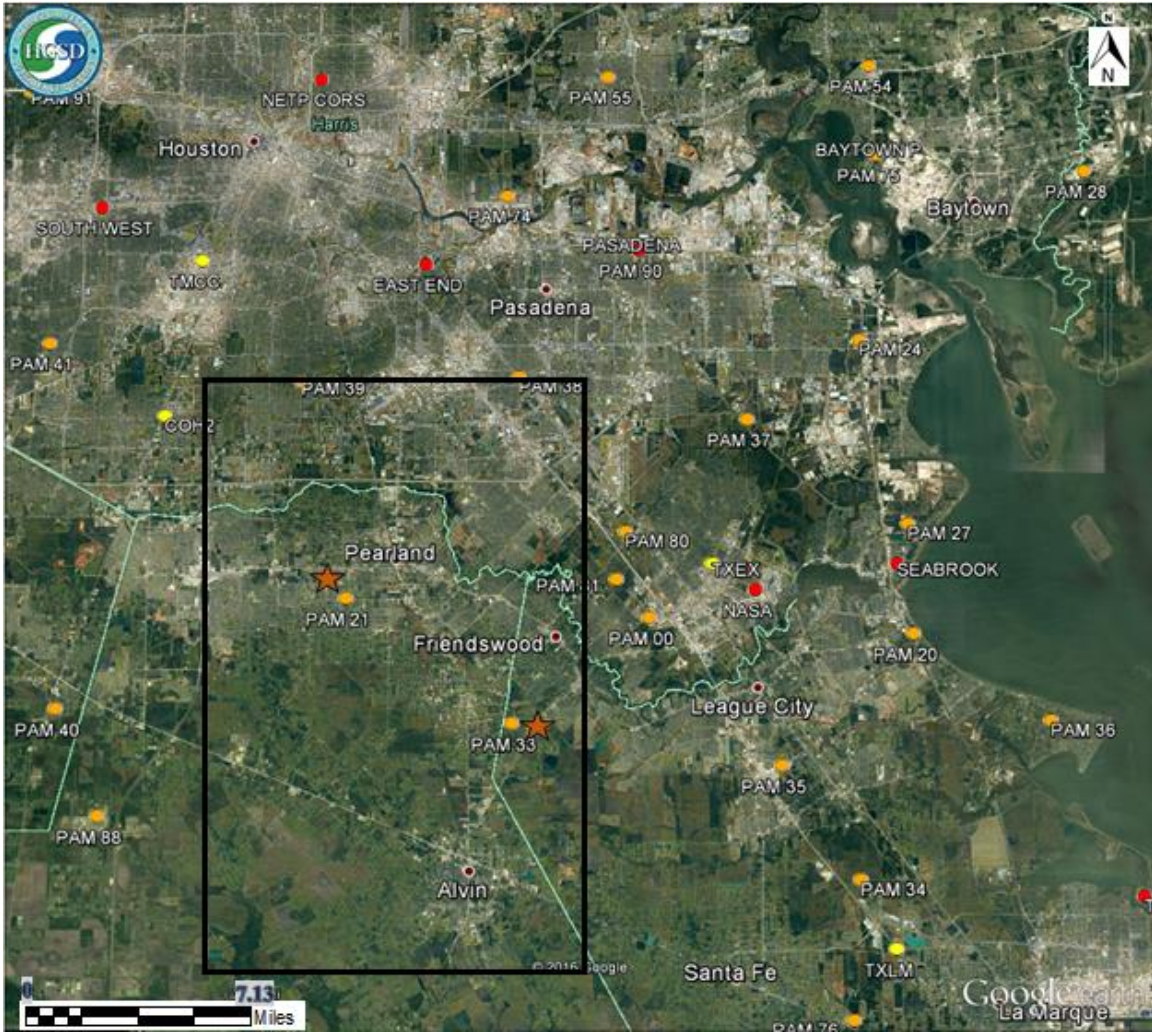


Figure 12 - Google earth imagery showing the spatial distribution of PAM's GPS used in monitoring of rate of subsidence in Gulf Coast of Texas. PAM 21 and PAM 33 (identified by brown stars) lies within the study area. *Data source: Harris-Galveston Subsidence District; <http://hgsubsidence.org/subsidence-data/database>.*

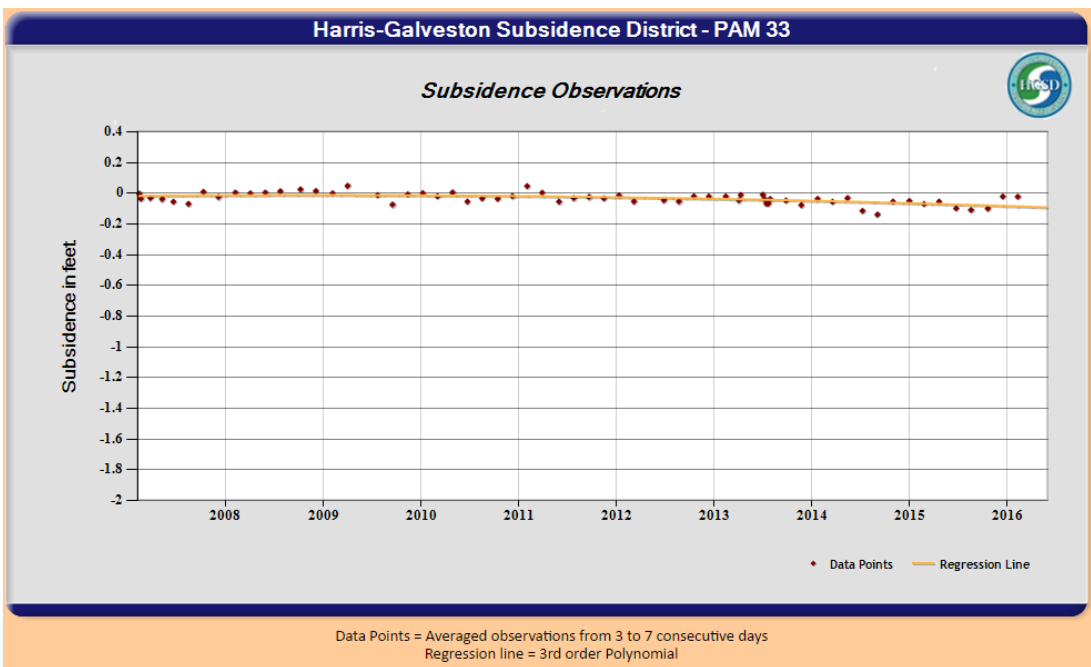
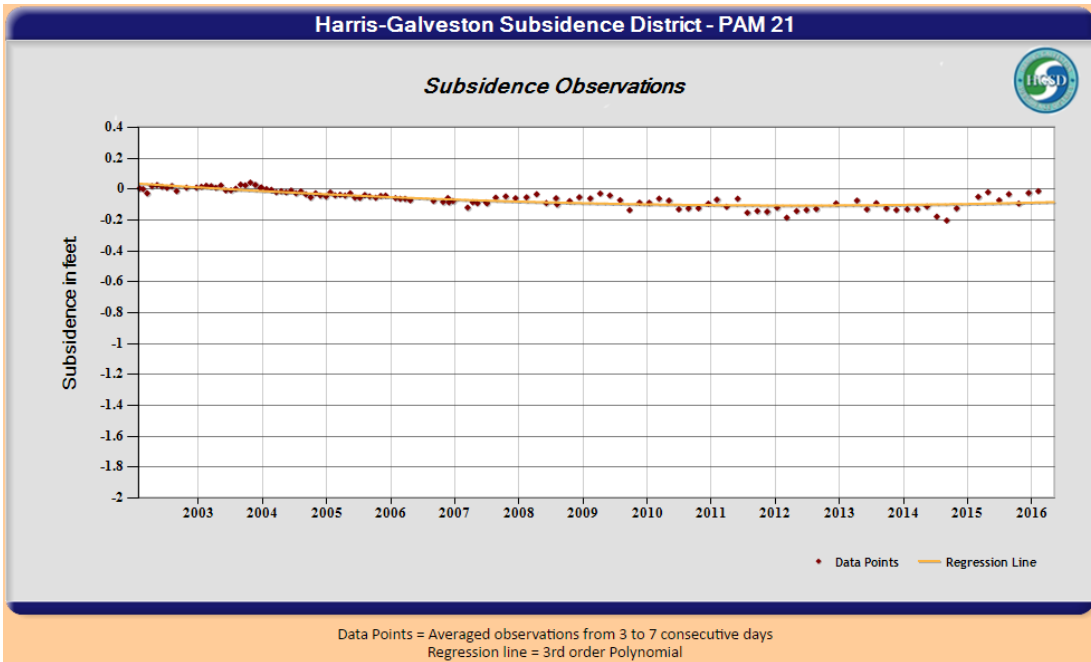


Figure 13 - A regression plot of rate of subsidence measured in PAM 21 and PAM 33 from the year 2003 to 2016. Data from PAM site 21 shows that an average subsidence rate of 0.24 cm / year occurred, while PAM site 33 shows an average subsidence rate of 0.3 cm / year occurred; data source: <http://mapper.subsidence.org/Chartindex.htm>

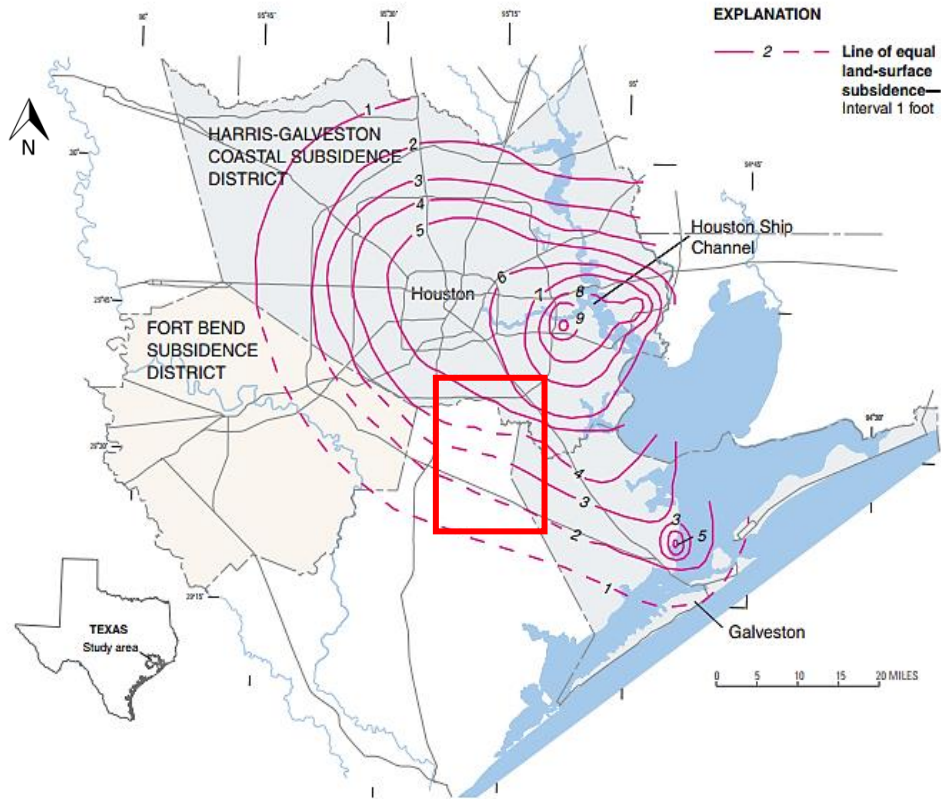


Figure 14 - Contour lines represent the amount of subsidence that occurred from 1906 - 1987 in Harris and Galveston regions in Texas (modified from Zilkoski et al., 2003). Study area highlighted in red rectangle.

GRAVITY THEORY

LAWS AND PRINCIPLES

Gravity Surveying involves the measurement of variations in the gravitational fields of the Earth. The gravity principle is based on Newton's Law of Universal Gravitation which states that the attraction of two masses, m_1 and m_2 , to each other is directly proportional to the product of their masses but inversely proportional to the square of the distance between the centers of the masses (Telford et al., 1990).

$$F = \frac{Gm_1m_2}{r^2} \dots \dots \dots \text{Equation 1}$$

Where G is the universal gravitational constant $6.673 \times 10^{-11} \text{m}^3 \text{kg}^{-1} \text{s}^{-2}$, while m_1 and m_2 are two masses in kg and r is the distance between the centers of each mass.

Gravitational force is not constant all over the surface of the earth because of the inhomogeneous nature of rock masses and the near-spherical shape of the earth. The magnitude of gravity readings is influenced by five factors; latitude, elevation, topography of the surrounding terrain, earth tide and density variations in the surface (Telford et al., 1990). Density increases with depth but not with lateral variation, which is a reason that the geoid and reference spheroid do not coincide.

There are two gravity measurement methods are; absolute and relative gravity measurements.

(a) Absolute Gravity Measurement: This involves measurement of the absolute gravity at a location. This can be carried out using: (i) Falling mass, where gravitational acceleration is determined by carefully measuring the distance and time of a falling mass and

(ii) Pendulum, where gravitational acceleration is determined by measuring the time of an oscillating pendulum (Telford et al., 1990).

(b) Relative Gravity Measurement: This involves measurement of variation in gravitational field. These are based on zero length spring or quartz spring concepts, and are generally sensitive instrument that can measure slight changes in gravity variation of 1 microGal. Examples are the CG-5 Scintrex Autograv and the Lacoste and Romberg gravity meter. Gravimeters are designed to measure the difference in gravity rather than the actual magnitude.

It is not possible for a gravity meter to measure both absolute gravity and the change in gravity variation. The absolute and relative gravity instruments measure the vertical components, which is the maximum of the total gravitational fields.

GRAVITY CORRECTIONS APPLIED

Gravity surveying is a passive geophysical method of investigation that measures forces of gravitational field in the earth. This gravitational field is neither generated nor influenced by the observer. The earth is not a perfect sphere and it is not homogenous in

nature. Due to these reasons, it is expected that the gravitational acceleration would differ from one location to another over the surface of the earth. The removal of unwanted components from gravity readings collected in the field is known as gravity correction or gravity reduction. The gravity corrections that are applied to raw gravity datasets are discussed below:

Drift Correction

This correction accounts for the changes caused by the instrument itself. It is expected that if a gravimeter is placed stationary at a point, and that gravity readings are taken at intervals, then the gravity measurement would not be consistent over this period. Prior to the invention of modern gravity meters, base stations were revisited every two to three hours to effectively calculate and correct for drift and tidal effects. The gravity meter (CG 5 Autograv) used for this study is equipped to automatically correct for tide and drift on measured gravity readings.

The sensor used by the CG-5 Autograv is made of a non-magnetic fused quartz which is not affected by the magnetic field variation of less than ten times the earth's magnetic field of $\pm 0.5\text{mT}$ (Scintrex, 2012). The stable operating environment of the quartz elastic system allows for long term drift of the sensor to be predicted accurately and the software applies the corrections to be less than 0.02mGal per day. It is due to this reason that the gravity readings observed at the base stations, at the start and end of the daily survey remains the same. It is recommended that a 12-24 hours' instrument drift

calibration be carried out on the instrument prior to field survey. This calibration procedure calculates a drift co-efficient that is applied to gravity readings to correct for drift and tidal effect (See Figure 16) for drift calibration graph plot).



Figure 15 - (left to right) (a) The top view of CG-5 Scintrex Autograv (b) displays the field set-up of the CG-5 gravity meter before a gravity measurement is taken. The gravity meter is mounted on a tripod which comes with a rotating foot screw used for adjusting for tilt. When adjusted within a range of ± 10 arcsec, a cross hair and an icon is displayed as shown in figure 15a.

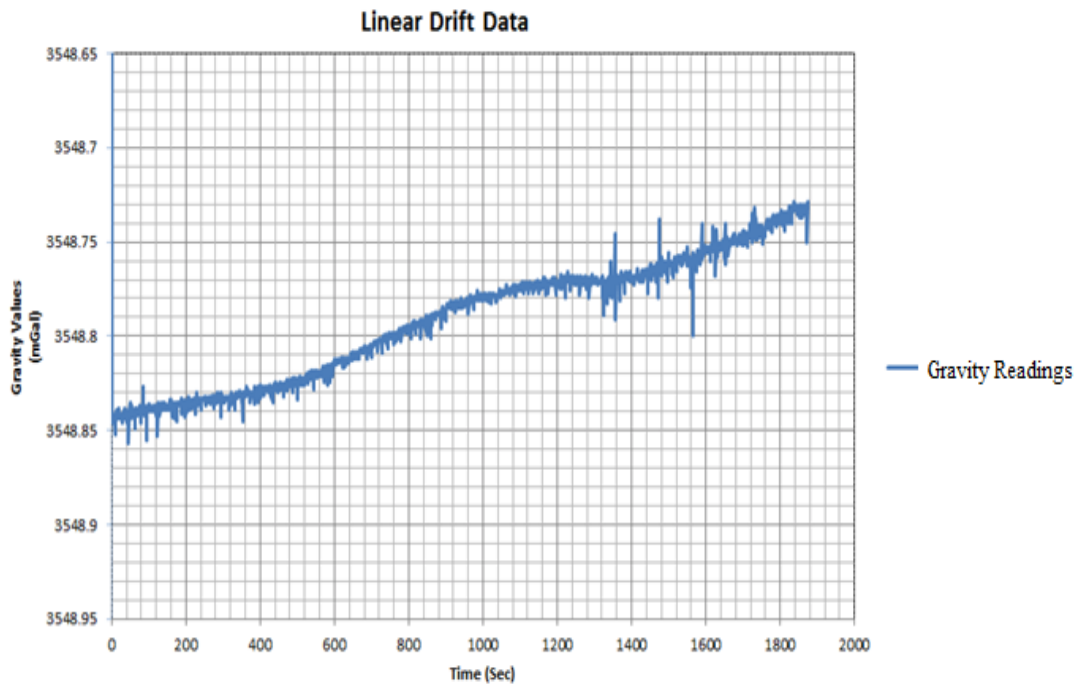


Figure 16 – A graph shows gravity values (mGal) measured against time (sec) for instrument drift calibration. This graph shows a linear trend of gravity measured to determine the drift co-efficient which is applied automatically by the software to correct for the effect of drift on gravity values measured.

Earth-Tide Correction

The Earth-Tide correction takes into consideration changes in gravity due to movement of the sun and moon which is also depends on time.

Latitude Correction

The latitude correction is also referred to as the Theoretical Gravity Correction (G_n). This correction considers the ellipsoidal shape of the earth, the rotation of the earth around its geographical axis, and the resulting bulge at the equator. This effect results in the smallest gravitational forces on the equator (maximum centrifugal force) and the largest gravitational forces at the poles (Telford et al., 1990). The effects listed above were removed by applying the International Gravity Formula (IGF) 1987 based on WGS 84 (World Geodetic System) as stated below:

$$G_n = 978032.68 \frac{(1+0.00193185138639\sin^2\phi)}{\sqrt{(1-0.00669437999013\sin^2\phi)}} mGal \dots \dots \dots \text{Equation 2}$$

The angle ϕ is the latitude angle in degrees that describes the shape of the earth from the point on the referenced ellipsoid (Arafin, 2014).

Elevation Correction

Elevation corrections are applied to gravity reading to correct for topographic effects resulting from the difference in elevation between a gravity station and the selected datum. There are generally three types of elevation corrections applied during gravity correction: Free-air, Bouguer and terrain corrections.

(a) Free-air correction: This is the initial process taken to correct for effects due to elevation. Recall from Newton's law of gravity equation (Equation 1), gravity decreases with the square of the distance. In other words, it is expected that there will be a change in gravity readings when the gravimeter is raised; hence that gravity data has to be reduced to a datum in order to compare and tie gravity readings collected at different elevations within the study area. When the elevation of a gravimeter is raised, the measured gravity reading is decreased by a vertical gradient of 0.3086 mGal/m. To measure within an accuracy of 0.01 mGal/m, the elevation of the gravity meter is measured with an accuracy of 3 cm. Free-air correction is added to the gravity field data if the gravity station is above the datum, and it is subtracted if the gravity station is below the datum. The datum used for this study is the mean sea level because that is the datum used by the LiDAR from which elevation values were extracted. All elevation values were above the datum; hence they were added to the measured gravity readings. Free-air correction (in mGal) values were calculated using the equation below:

$$\text{Free – air correction (FAC)} = 0.3086 h \dots \dots \dots \text{Equation 3}$$

h = elevation (in meters).

The free-air anomaly is the difference between theoretical and observed gravity. A free-air anomaly is most applicable during a marine gravity survey where topographic corrections cannot be applied.

$$\text{Free – air anomaly (FAA)} = G_{obs} - G_n + FAC \dots \dots \dots \text{Equation 4}$$

Where: G_{obs} is the gravity values corrected for drift and tide (in mGal)

G_n is theoretical gravity, corrected for latitude (in mGal)

(b) Bouguer correction: The Bouguer correction is another type of elevation correction applied to a gravity dataset. This correction removes the effect of rock density in between the measured gravity point and the referenced datum (mean sea level). This effect was not put into consideration in the free-air correction equation. This mass effect (density) causes measured gravity values to be greater at higher elevation than at lower elevation; however, the effect is removed from gravity readings. An assumed horizontal slab with an average density of the surrounding rock is added, hence the name Bouguer correction, named after the French geophysicist and geodesist, Pierre Bouguer. The Bouguer correction is shown below:

$$\text{Bouguer Correction} = 0.04193\rho h \dots \dots \dots \text{Equation 5}$$

Rho (ρ) is the average density of the surrounding Bouguer slab, and h is the elevation in meters. An average rock density value of 2.65g/m³ was assigned to the Bouguer slab based on the geologic composition (sand and silt) of the study area.

Free-air correction and Bouguer correction are often combined to generate a generalized gravity elevation correction as shown below:

$$\textit{Elevation correction} = (0.3086 - 0.04193\rho)h \textit{ mGal} \dots \dots \dots \textit{Equation 6}$$

(c) Terrain correction: Due to the earth's curvature and the irregular topographic nature, the assumption of a horizontal and infinite Bouguer slab in Bouguer correction is not always valid. Therefore, a correction for the effect of topography is accomplished by the use of Terrain correction. This correction takes into consideration the irregularities in terrain from one location to another and in respect to the gravity station. Hills or topographic high surfaces that are located above the elevation of gravity station exert an upward pull on the gravimeter, thereby decreasing the gravity acceleration, while valley and low-lands that are located below the elevation of the gravity station fails to pull it down (Telford et al., 1990). These topographic surfaces such as hills and valleys affect gravity measurements; therefore, terrain correction is added to the gravity station values.

Terrain correction was not applied to the gravity dataset collected for the field because the study area is characterized by a flat to low-lying topography.

METHODOLOGY

INSTRUMENTATION

Scintrex CG-5 Autograv (Gravimeter)

Scintrex CG- 5 Autograv is a microprocessor-based automated gravity meter that has a measurement range of over 8000 mGal without reset. It has a reading resolution of 0.001 mGal with a standard deviation that is <5 mGal. These advantages allow the use of the autograv for both field investigations and large scale regional or geodetic surveys (Scintrex, 2012). The sensor system is made from a non-magnetic, fused, quartz spring with a spring co-efficient of approximately -130 mGal / °K, so that the spring becomes stronger as the temperature increases. The spring is protected from ambient temperature, so that it maintains its spring temperature constant to within 0.5 mK under normal operating conditions (Scintrex, 2012).

The gravity meter is composed of an electronic tilt sensor which can automatically compensate for errors in instrument tilt during a measurement. The Scintrex CG- 5 Autograv calculates and applies a real time tidal correction based on the geographical location and time zone entered by the operator or GPS (Scintrex, 2012). It has an incorporated seismic filter that removes micro-seismic noises due to locally induced shocks (Scintrex, 2012).

Trimble NOMAD GPS

The Trimble NOMAD GPS unit is an outdoor, handheld computer with an integrated GPS receiver for navigation applications (Figure 17). This unit is equipped with a Marvell PXA320 XScale 806 MHz processor and Windows Mobile 6.1 software which can run a wide range of third-party applications. This has one of the fastest processors in the Windows Mobile device market (Figure 17). It is integrated with quad-band GSM GPRS/EDGE and GPS (WAAS / SBAS) capability (Trimble, 2011). The Trimble NOMAD GPS unit is also enabled with 5-megapixel camera resolution that can capture and geotag images with an integrated GPS receiver.

The Trimble NOMAD GPS unit was used to determine the geographic locations for each of the gravity readings collected during the field survey. The geographic coordinates attached to each of the gravity data points were displayed on a map to determine the spatial distribution and extent of the gravity data coverage.



Figure 17 – (left to right) (a) A display of the Trimble Nomad GPS Unit; (b) display of GPS unit used in acquiring geographic coordinates for a gravity station in the field.

LiDAR

LiDAR (Light Detection and Ranging) is a remote sensing technology that measures vertical distances by illuminating a target with a laser and analyzing the reflected light. This data was collected using the LH systems ALS50 light detection and ranging (LiDAR) system with a ground sample distance of 1.4m. The LiDAR data for Texas was acquired by Sanborn Mapping Company Incorporation for six different day intervals between April 9 – May 13, 2006. The data was collected on behalf of Texas Water Development Board (TWDB) and Federal Emergency Management Agency (FEMA). This dataset was in laz file format and it contains elevation estimated values (in meters) using LiDAR technology. The LiDAR dataset has a vertical positioning accuracy of $\pm 18\text{cm}$ in open terrain and a vertical altitude resolution of 1 cm.

The LiDAR dataset was used to create a DEM, Digital Elevation Model, of the study area. DEM represents terrain surface and it displays areas of highs and lows within the study area. The DEM is also used to investigate for elevation surface especially over the gravity low derived from Bouguer anomaly.

SOFTWARE

Geosoft Oasis Montaj and GM-SYS 9.0

Geosoft Oasis Montaj (version 9.0) is a powerful mapping and analysis tool. Geosoft Oasis Montaj 9.0 was used to create grids which present data in the form of an iso-anomaly contour map. All grid maps were created by using the Kriging method.

GM-SYS module is an extension of Oasis Montaj 9.0 which is used to generate the 2D hypothetical geology model based on the calculated gravity responses. GM-SYS uses the forward (alternately referred to as indirect) approach in calculating gravity data. The forward approach involves the process of individually assigning rock densities to rock layers being modelled based on calculated gravity anomaly (Seigel, 1995).

IHS Petra 3.7.2

IHS Petra version 3.7.2 provides solutions for data management, manipulation, visualization and integration of geological, geophysical and petro-physical data. This software was used to display the subsurface geology using petro-physical properties from well logs.

ArcGIS 10.3

ArcGIS version 10.3 was developed by ESRI and it is a geographical information system that is used in creating maps and analyzing data. ArcGIS 10.3 is equipped with several extensions, and it can perform basic geo-spatial analysis. ArcGIS 10.3 was used to create maps which represent spatial distribution and extent of gravity points. This

software was used to process the LiDAR dataset by creating a Digital Elevation Model (DEM) from which the elevation values were extracted.

ERDAS IMAGINE

ERDAS IMAGINE is a remote sensing application with a raster graphic editor designed for geospatial applications. ERDAS IMAGINE was used to process satellite image used to create a classified land cover map.

DATA COLLECTION AND DATA PROCESSING

GRAVITY FIELD SURVEY

A gravity dataset was collected by using the CG-5 Scintrex Autograv, and a gravity field survey was taken on different intervals between the months of May through August 2016. A local gravity base station was established within the study area, and this local base station was revisited at the beginning and at the end of each day during the field survey. Multiple local base station visitations were done to ascertain the degree of accuracy of the drift correction which is automatically applied to all gravity readings by the CG-5 Autograv. The gravity meter was programmed to collect three gravity readings per gravity station, and the third readings of each cycle of the gravity measurement were collated and used. ESRI ArcGIS 10.3 was used to display gravity data points on a map and to examine the spatial coverage of gravity data points collected. This was done to

suggest where additional gravity data points were needed in order to get a widely-distributed set of gravity data points (Figure 18). Prior to the beginning of the field survey, an initial study area boundary was drawn around Hastings Oil Field which is located at the border northeast of Brazoria County and northwest of Galveston County (Figure 18). Due to some observations during the data processing phase of this research, the study area was extended northwards and towards south of Harris county in order to accommodate for additional findings. Gravity data was collected in two batches, because the full extent of the gravity low anomaly, which is being investigated, was not captured. Subsequently, additional field visits were conducted and survey continued northwards into Harris County, thereby increasing the data coverage and accommodating for additional checks. A total of 537 gravity readings were collected during this study (Figure 18).

The field survey was conducted in a non-traditional approach, i.e. without grids or lines (Figure 18). Gravity data were collected at a spacing interval of one-third to one-quarter of a mile and along accessible roads and public places. Gravity measurements were not taken in restricted areas such as private and government properties.

All relative gravity readings measured using the CG-5 Scintrex Autograv were tied to a pre-established absolute gravity base station. The absolute gravity base station is located at latitude N 29°44.2 and longitude W 95°25.10 which is by Branard and Argonne Streets, southwest of downtown Houston (Figure 18). The absolute gravity information of the base station was retrieved from the International Gravimetric Bureau website, <http://bgi.omp.obs-mip.fr/data-products/Gravity-Databases/Reference-Gravity->

Stations (Figure 19). This absolute base station is the closest one to the study area and it is an open and easily accessible. The absolute Gravity was measured in July of 1967 and found to be 979283.720 mGal with an estimated accuracy of $\pm 0.1\text{mGal}$ (Figure 20), at an elevation of 18.4 meters. The procedure for measuring absolute gravity at based stations is in accordance with the International Gravity Standardization Network of 1971. A gravity meter was used to measure the absolute gravity reading for this location. The variation in gravitational field between the local base station in the study area and the pre-established absolute gravity base station was measured using the CG-5 Scintrex Autograv. Subsequently, all gravity readings were tied to the established gravity base station by a process called looping. Looping was carried out by taking relative gravity readings at the local base station and the pre-established absolute gravity base station using the CG-5 Scintrex gravity meter. Since the absolute gravity value at the gravity base station is known, the change in magnitude of gravity measured in other place nearby can be tied to it to determine the absolute gravity value at local base stations.

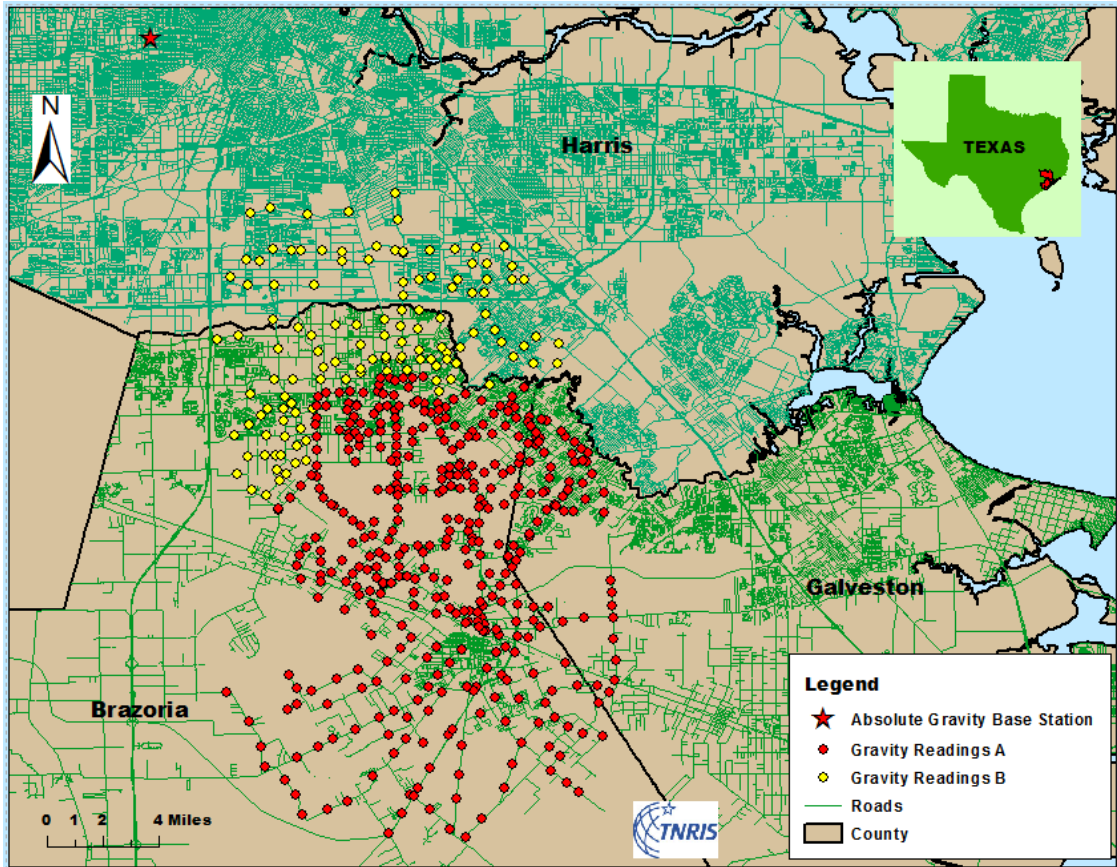


Figure 18 – Spatial distribution of the 537 gravity readings (red and yellow circles) that were collected in the field and the location of the absolute gravity base station (red star) in southwest Harris County. The red circles represent the first phase of the gravity dataset collected between 5/7/2016 to 6/4/2016 which was restricted to Brazoria and Galveston Counties, while the yellow circles represent the second phase of the gravity dataset collected between 07/17/2016 to 8/24/2016.

**Bureau Gravimétrique International
International Gravimetric Bureau**

Search

The BGI | Data / Products | Activities | Publications | Links

BGI > Data / Products > Gravity Databases > Reference Gravity Stations

Reference Gravity Stations

ID	Name	Easting	Northing	UTM Zone	Access		
003581	GALVESTON	29.30333	-94.9167	2.30	979280300	500	open access
038374	GILMER	32.70917	-94.94500	116.70	979501090	200	unknown
040021	GUTHRIE	33.61967	-100.32167	530.10	979444120	100	open access
038434	HARRIS	33.76500	-94.72917	103.60	979607120	200	unknown
039911	HEAVENER	34.88917	-94.60167	161.54	97955230	100	open access
002700	HOUSTON	29.65000	-95.27833	15.20	979278770	0	unknown
002703	HOUSTON	29.65000	-95.27833	15.20	979278660	0	unknown
002702	HOUSTON	29.71833	-95.40167	18.00	979283720	0	unknown
002706	HOUSTON	29.73333	-95.42667	18.00	979282910	0	unknown
00270A	HOUSTON	29.65000	-95.27833	15.20	979278700	0	unknown
002705	HOUSTON	29.65000	-95.28333	15.20	979278660	0	unknown
002701	HOUSTON	29.73667	-95.41833	18.40	979283720	0	open access
002704	HOUSTON	29.65000	-95.27833	15.00	979278700	0	unknown
002709	HOUSTON	29.65000	-95.27833	15.20	979278700	0	unknown
002708	HOUSTON	29.61667	-95.16667	11.89	979275060	100	unknown
002707	HOUSTON AIRPORT	29.65000	-95.27833	15.20	979278670	0	unknown
038281	JUNCTION	30.33967	-99.77583	524.60	979213630	200	open access
004651	KENT	31.06833	-104.20167	1290.80	979039500	500	unknown
038361	KILGORE	32.38750	-94.87583	111.90	979485410	200	open access
003864	KINGSTON	32.18333	-93.71000	69.80	979491430	200	open access
038324	LAMONT	30.65667	-94.95167	39.00	979351570	200	unknown
005151	LAREDO	27.53667	-99.45667	156.10	979064610	0	unknown
005153	LAREDO	27.50000	-99.75000	0	979062550	0	unknown
005152	LAREDO	27.54450	-99.46117	151.72	979065090	100	open access
005154	LAREDO	27.53333	-99.45833	156.00	979067130	100	unknown
046561	LAS VEGAS	35.59367	-105.21833	1961.70	979193320	100	open access
046562	LAS VEGAS	35.59367	-105.21933	1961.70	979193130	100	unknown
052792	LEONARD	35.91050	-95.79250	256.00	979721080	100	unknown
052791	LEONARD	35.91133	-95.79250	256.00	979720960	100	unknown
052783	LEONARD	35.91167	-95.79250	255.00	979721200	100	unknown
009361	LUBBOCK	33.65500	-101.81500	992.40	979308360	0	open access
038391	MASTERSON	35.57300	-101.94967	1080.50	979430570	200	unknown
051892	MC ALESTER	34.93200	-95.76850	200.00	979619430	100	unknown
051891	MC ALESTER	34.93200	-95.76850	200.00	979619330	100	unknown
040041	MCAMEY	31.13700	-102.22750	759.87	979178600	100	open access
053141	MEXIA	31.68017	-96.48233	162.50	979439660	100	unknown
004454	MIDLAND	33.00333	-103.06167	843.70	979208200	500	unknown

affiche

Figure 19 - Absolute Gravity Base Station database containing pre-established absolute gravity readings at different locations. The station highlighted in red is the closest to the study area and it is an open access absolute gravity base station. This location was used to tie all 537 gravity readings that were collected in the field. Data source: International Gravimetric Bureau (retrieved August, 2016).

Gravity Base Station: 002701, g (microgals) = 979283720

GRAVITY BASE STATION			
LATITUDE	29° 44.20' N (1)	STATION DESIGNATION	HOUSTON
LONGITUDE	95° 25.10' W (1)	COUNTRY/STATE	USA/Texas
ELEVATION	18.40 METERS (1)	ADOPTED GRAVITY VALUE	
REFERENCE CODE NUMBERS			
ACIG 0270-1			
IGC 08295B			
GW 18			
		ESTIMATED ACCURACY	DATE
		+ 0.1 mgals	MONTH/YEAR July/1967
DESCRIPTION AND/OR SKETCH			
<p>The station is southwest of downtown Houston at the northeast corner of Branard St. and Argonne St., at the former Hall-Sears Co. (2424 Branard St., also formerly occupied by Houston Technical Lab and Electro Tech International Co.), near the center of the building, east of the reception room, in the former lunchroom, at the west wall, about two meters south of the northernmost of two doorways in the west wall, on the tile floor.</p> <p>Station is monumented with a USAF Gravity Disk. A USC&GS Gravity Disk is set vertically 0.3 meters south of the northwest corner of the building, 0.3 meters above the ground. (1)</p>			
REFERENCE SOURCE			
(1) 02733			

ACIG HQ FORM FEB 68 O-415

<http://bgi.omp.obs-mip.fr/data-products/Gravity-Databases/Reference-Gravity-Stations>

Figure 20 – Map showing the location of the absolute gravity base station closest to the study area. It is located in SW Houston and is represented by the red star in Figure 18. Data source: International Gravimetric Bureau (retrieved August, 2016).

ELEVATION DATA

Elevation values used for gravity elevation corrections were extracted from a Digital Elevation Model (DEM) and were created from LiDAR data. The LiDAR dataset values were in laz (Galveston and Brazoria) and e00 (Harris) file extension format. These LiDAR file formats were analyzed and processed using ESRI ArcGIS version 10.3 to produce a raster DEM. The field gravity data in .txt format was converted to a shapefile (point feature class) and was overlain on the DEM (Figure 21). The elevation value at the point of intersection between the gravity data and the DEM was extracted and recorded (Figure 21). Elevation values for the Harris County LiDAR data was converted from feet to meters, while that for Brazoria and Galveston had their elevation values reported in meters.

An additional elevation dataset was used for this study, the ETOPO1, which is a 1 arc-minute global relief model of the earth's surface. This elevation dataset was extracted from National Oceanic and Atmospheric Administration (NOAA): National Centers for Environmental Information (NCEI). The horizontal datum for ETOPO1 is a world geodetic system WGS 84 and the vertical datum is mean sea level (Amante and Eakins, 2009). Elevation values were reported in meters with a cell size of one arc minute. The ETOPO1 dataset is available in two versions: Ice Surface, (top of Antarctic and Greenland Ice sheets) and Bedrock (the base of the ice sheet) (Amante and Eakins, 2009). The ETOPO1 bedrock dataset was gridded and used to generate an elevation map. The ETOPO 1 elevation value was used as an elevation for the creation of the 2D hypothetical gravity model.

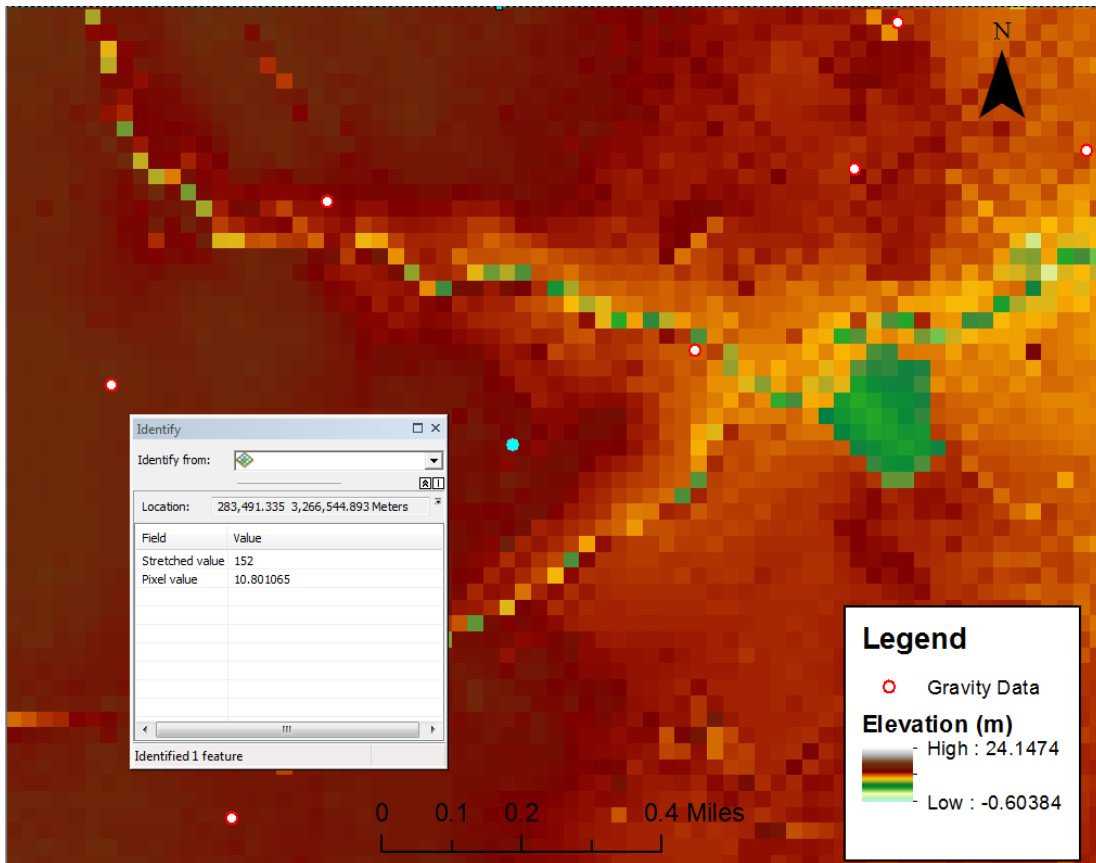


Figure 21 – Map showing gravity data points overlain on a DEM and elevation values assigned to pixels. These elevation values were recorded and used for elevation correction. The gravity data point highlighted in a light blue circle displays the elevation values assigned to the pixel where the gravity station intersects with the DEM. The elevation value for the highlight gravity station represented with a blue circle is 10.8 meters. The DEM was generated from a LiDAR dataset over the study area.

MAGNETIC DATA

A total Magnetic Intensity dataset of Texas was obtained from the Pan American Center for Earth and Environmental Studies, PACES, at the University of Texas at El Paso, UTEP. PACES is an open source database that contains gravity and magnetic datasets for the United States of America. The magnetic dataset was acquired by GeoMetric Incorporated between March – May, 1977. The aeromagnetic survey was acquired in an E-W direction and with a line spacing interval of 1.6 km (3 miles) by an aircraft flown at a height of 305 meter above terrain.

The magnetic intensity dataset represents variations in the earth's magnetic field. The earth's magnetic field is measured with the aid of a magnetometer. Variations in the earth's magnetic field are as a result of an uneven distribution of magnetite in rocks from one point to another. Magnetic Intensity anomalies reveal subsurface structural features based on the degree of magnetic characteristic of the rock. The total magnetic intensity values contained in the dataset is reported in nanoTesla (nT).

The magnetic intensity dataset was used in this study to visualize and understand the distribution of magnetic properties of rocks and to supplement the gravity data in creating 2D hypothetical gravity models. This serves as an additional control measure to restrain the model based on density and magnetic properties of rocks, so that so it is geologically realistic. This goal was achieved by matching the observed magnetic and gravity data so that the calculated magnetic and gravity curves are as realistic as possible.

SATELLITE IMAGERY

Satellite Imagery was downloaded from the U.S. Geological Survey (U.S.G.S) webpage and was originally acquired from a Landsat 8 spacecraft with an OLI_TIRS sensor. The study area lies within path 25 and row 40 of the spacecraft's orbit and the imagery file was in a geotiff format. The horizontal datum was hung hanged on WGS 84 and the map projection in UTM zone 15. The image's landsat scene id is LC80250402016126LGN00 and it was acquired by the space-craft on the 5th May, 2016 with a reflective grid cell size of 30m.

The satellite image was classified using ERDAS Imagine to create a land cover map of the study area. This process was done to highlight streams to apply the concept of creekology. Creekology is a useful investigation technique that can be applied to classified land cover maps. Creekology is a non-systematic method that was used for finding oil in the 19th to early 20th century (Frehner, 2004). This old technique is based on the relationship between the flow of creeks relative to topographic and structural highs, the latter of which might create prospects for presence of oil. Creekology was restricted to a narrow geographic range and oil targets downslope of anticlinal structures, which often formed valleys through which creeks flowed (Frehner, 2004). This technique also relied on surveying the landscape to find oil seeps which displayed a rainbow swirl on the surface of water bodies (Frehner, 2004).

Creekology was adopted in this study not for the purpose of finding oil but to observe flow patterns of creeks around structural highs or anticlinal structures, especially around salt domes. This is often a clue to identifying subsurface geological features.

WELL LOGS

Well logs were used to correlate beds based on similarities in their petro-physical characteristic and properties of the rocks in the subsurface. Eleven well logs were obtained from Texas Railroad commission, <http://www.rrc.state.tx.us/about-us/resource-center/research/gis-viewers/public-gis-viewer/> (Table 1). The well logs were processed and analyzed using IHS Petra to create a structural map of the subsurface. This structural map was used to delineate the presence of possible faults or the effects of uplift resulting from or associated with salt domes.

The main producing reservoir in the Hastings Oil Field is the Frio Sandstone at the depth range of 1,640 meters to 2,080 meters (Thomas, 1953). A Structural map of the top of the Frio Sandstone Formation was created by Thomas (1953) (Figure 22) and this map was adopted for this study. The structural map was georeferenced using the Texas land survey boundary shapefile from TNRIS. Thomas (1953) interpreted a northwest trending normal fault with a maximum throw of 213 meters (700 feet) which divides Hastings Oil Field into West Hastings and East Hastings Oil Fields (Thomas, 1953)

(Figure 22). A line of section of the wells used to create the stratigraphic column, structural and isopach maps is shown in Figure 23.

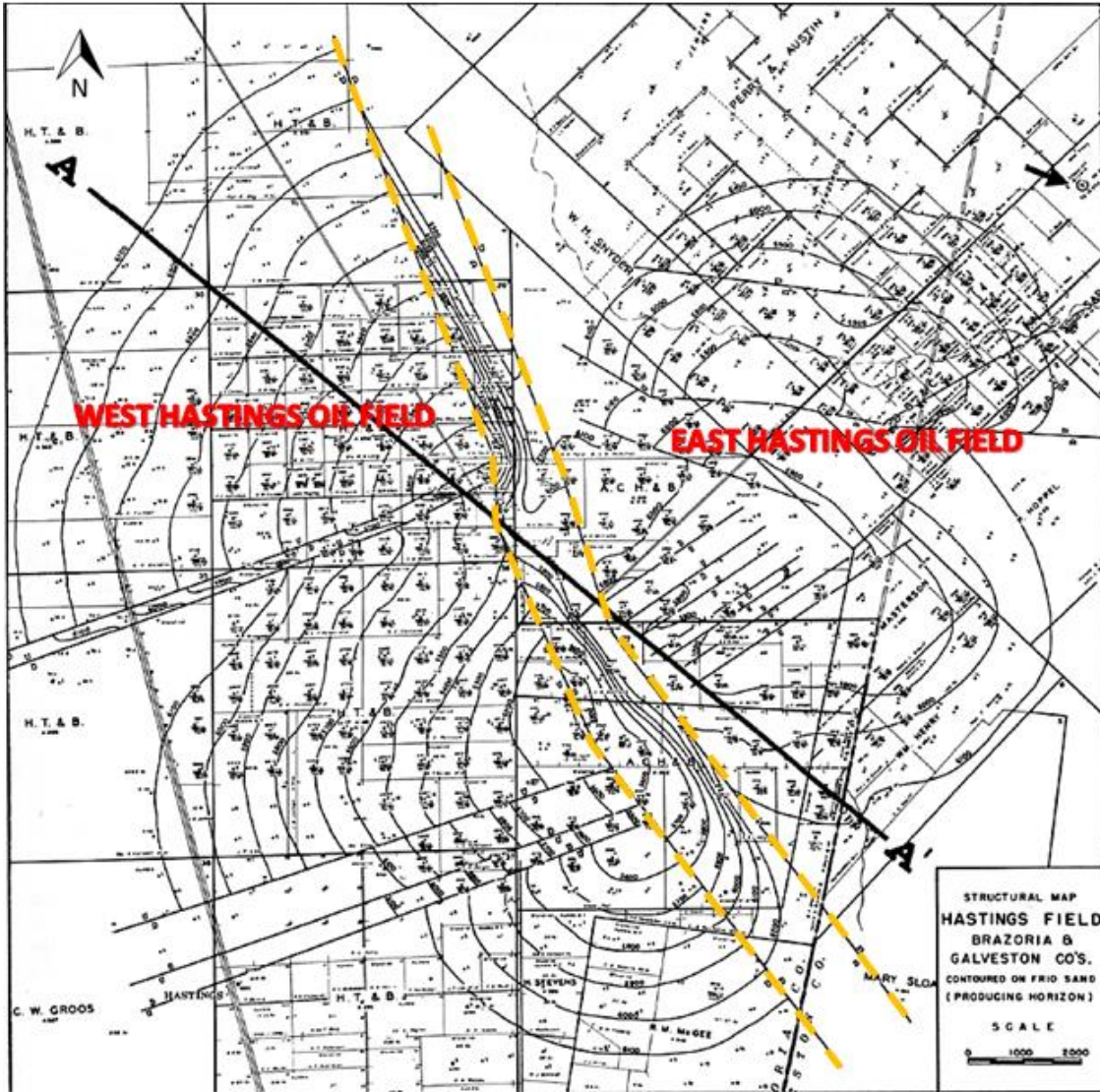


Figure 22 - Structural map of Frio Formation at Hasting Oil Field Yellow dash lines represent the north-west trending normal fault that divides the oil field into two arms; Hastings West (left) and Hastings East (right) Oil Fields. There are also several minor southwest to northeast trending normal faults (modified from Thomas, 1953).

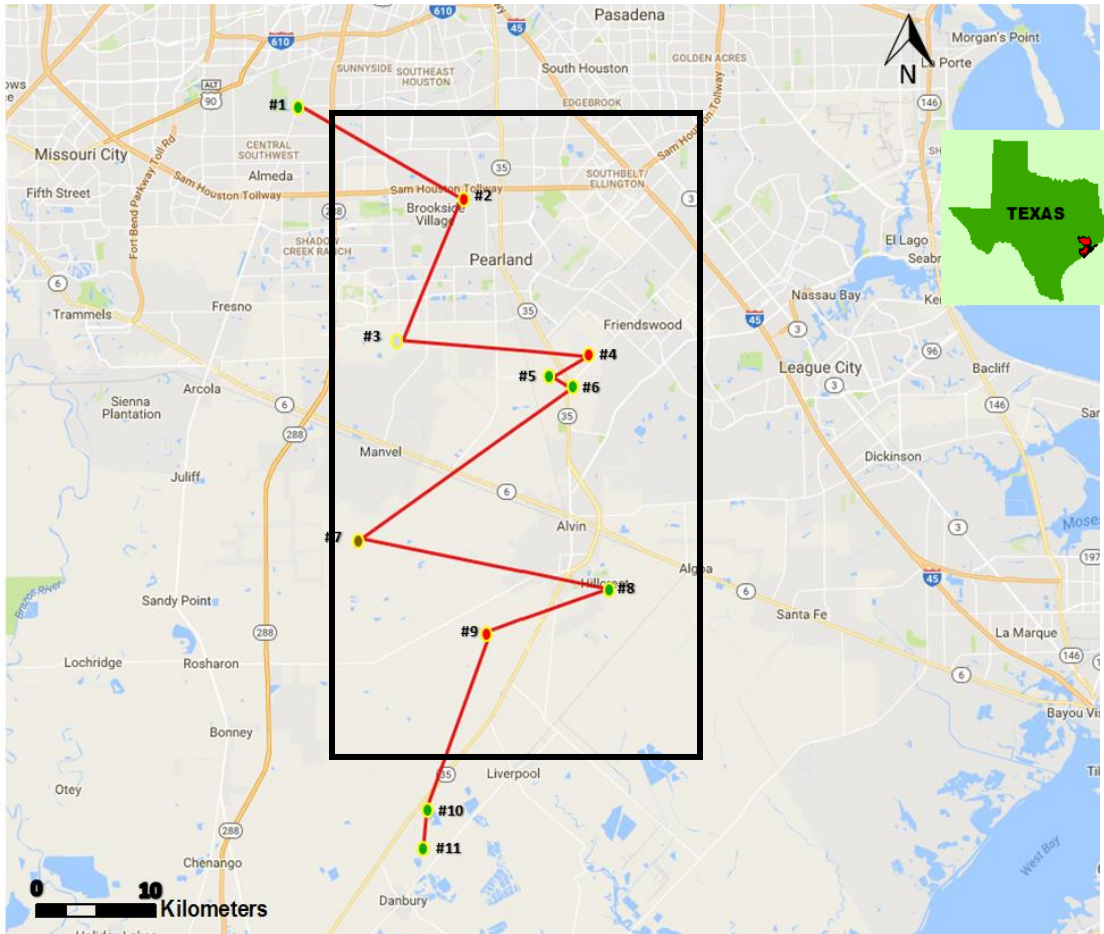


Figure 23 – Line of section for cross-section from well 1 to well 11 (Figure 39). Study area in black rectangle. www.gpsvisualizer.com. Well #1 (Pierce Junction), #2 (Hastings), #3 (Manvel), #10 (Danbury), and #11 (Danbury) are associated with the presence of salt domes, while well #4, #5, and #6 are in the Hastings Oil Field.

	Longitude	Latitude	API	Well Type	Oil Field Name / County
1	-95.408449	29.644766	4220132697	Oil Well	Pierce Junction / Harris
2	-95.3099270	29.594690	4220132868	Gas Well	Mykawa / Harris
3	-95.2703710	29.5208660	4203933086	Injection Well	Gubert #1 / Brazoria
4	-95.2342830	29.5127690	4203932768	Gas Well	Hastings East / Brazoria
5	-95.2549090	29.5016090	4203933183	Oil Well	Hastings West / Brazoria
6	-95.244173	29.495622	4203932971	Oil Well	Hastings West / Brazoria
7	-95.3694690	29.4175070	4203933055	Dry Hole	Bailey's Prairie / Brazoria
8	-95.22208	29.3913280	4203932742	Oil Well	Wildcat / Brazoria
9	-95.2922630	29.3698	4203932739	Gas Well	Wildcat / Brazoria
10	-95.3301490	29.2770590	4203933185	Oil Well	Danbury Dome / Brazoria
11	-95.3325320	29.2573870	4203933058	Oil Well	Danbury Dome / Brazoria

Table 1 - Well Log Data obtained from Texas Railroad Commission showing location, API number, well type and oil field counties. Data source: Texas Railroad Commission [retrieved August, 2016].

RESULTS AND INTERPRETATION

The objective of a gravimetric survey is to reveal the lateral distribution of rock density in the subsurface. This information can estimate the extent and distribution of subsurface geology based on gravity anomaly values (Seigel, 1995).

Elevation, observed gravity, theoretical gravity, free-air anomaly, residual gravity anomaly, and Bouguer gravity anomaly maps were created from gravity data collected from the field. Gravity data retrieved from the PACES database was also gridded and compared to gravity data collected from the field. The total magnetic intensity dataset for Texas was also gridded to observe the distribution of magnetic anomalies.

ELEVATION

Elevation maps for the two elevation sources used (elevation values from DEM and elevation values from ETOPO1) were gridded. The ETOPO 1 elevation map that was generated shows a regional view of elevation beyond the study area (Figure 24).

Elevation data for the study area was extracted from the ETOPO1 database and was re-gridded (Figure 25); elevation values were extracted from the DEM (Figure 26) were also subsequently gridded. The two different elevation sources for the study area displayed a similar elevation distribution trend when compared. The DEM elevation map represents elevation values assigned to gravity stations, which is dependent on the spatial

distribution of the location of the gravity stations. The ETOPO 1 elevation map has more evenly distributed elevation points. Due to this observation, the ETOPO 1 elevation map was used instead for the construction of the 2D hypothetical gravity model.

The regional ETOPO1 map shows elevation high values of 91.7 meters in the northwest which decrease in a southeast direction towards the Gulf of Mexico to low elevation values of -16.2 meters (Figure 24). The ETOPO 1 elevation map for the study area shows high elevation values of 21.9 meters in the northwest portion and a decrease to the southeast direction to a low elevation value of 5 meters (Figure 25). The DEM elevation map shows a similar trend with high elevation value of 18.3 meters to the west and decreasing in a southeast direction to a low elevation value of 5.5 meters (Figure 26).

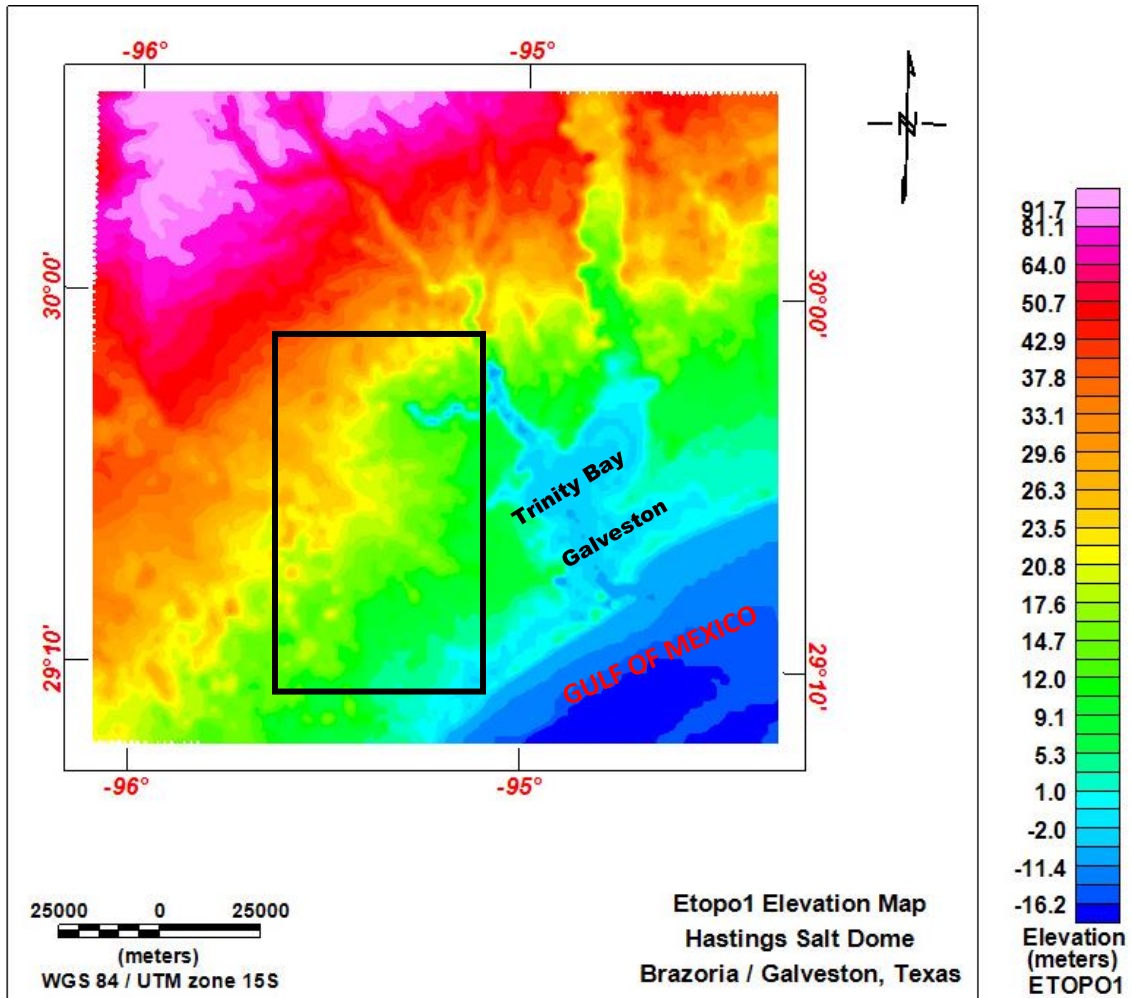


Figure 24 – A regional ETOPO1 elevation map extracted from NOAA database (Amante and Eakins, 2009). Elevation high values are observed in the northwest portion with gradual decrease in elevation values towards the Gulf of Mexico in a southeast trend. Study area highlighted in black rectangle.

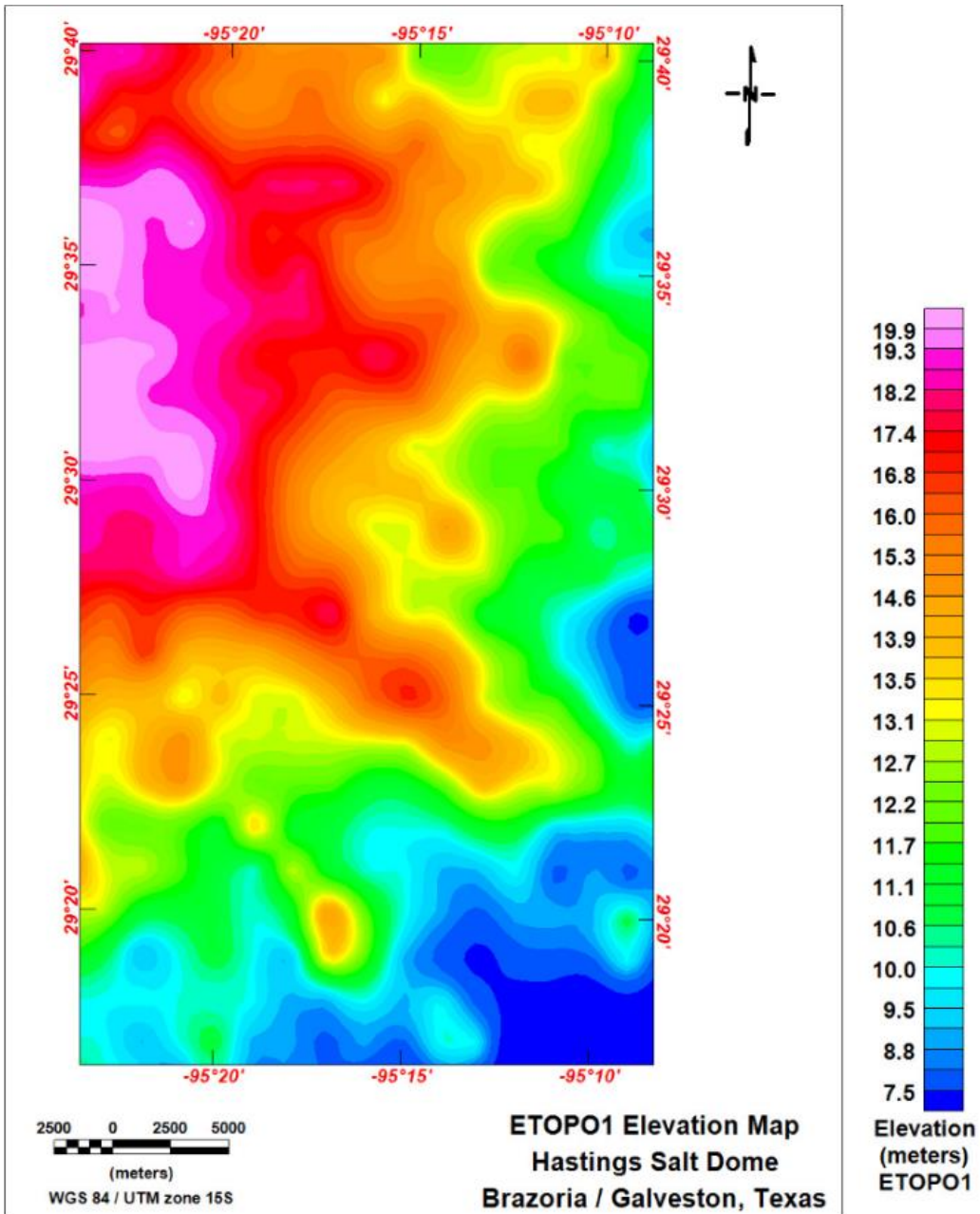


Figure 25 – ETOPO1 elevation map of the study area extracted from NOAA database (Amante and Eakins, 2009). Elevation high values of 21.9 meters are located to the west and decrease to the southeast to a minimum value of 5 meters.

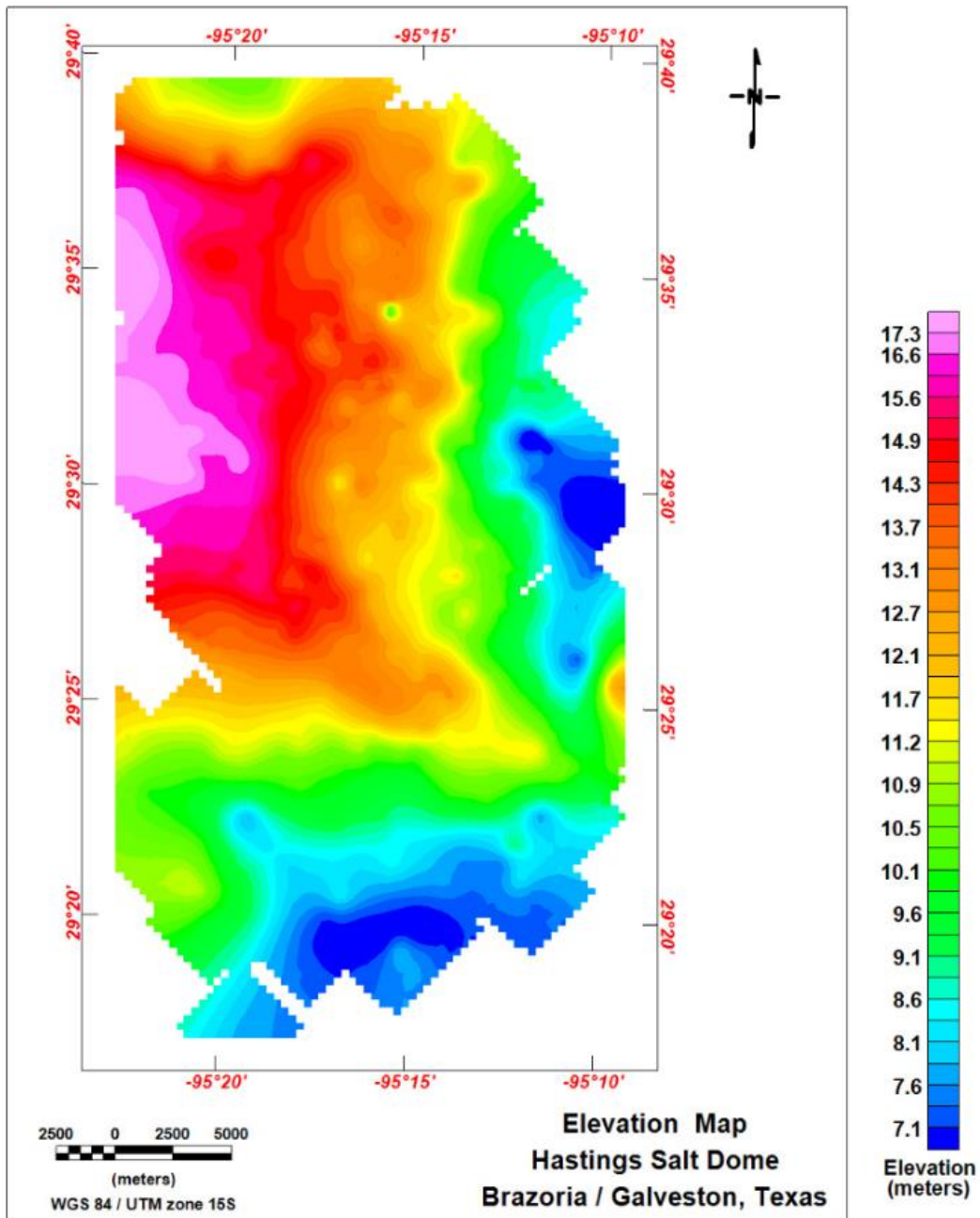


Figure 26 - Elevation map from gravity data collected from the field. Elevation high values of 18.4 meters were observed in the west and decrease to a lowest elevation of 5.5 meters at the southeast edge of study area.

GRAVITY MAPS

Gravity correction techniques discussed in Gravity Correction section earlier were applied to field data and used to create various gravity anomaly maps. Gravity data extracted from the PACES database were also gridded and used to create similar maps for comparison purposes. The comparison was done to ascertain the degree of data consistency between gravity data collected from the field and gravity data extracted for the PACES database. Gravity data observations and interpretations are discussed below.

OBSERVED GRAVITY

Observed gravity values were gridded to create an Observed Gravity Map (Figure 27). Observed gravity values represent gravity data collected from the field and are tied to an absolute gravity base station of IGSN 1971. Besides the tide and drift corrections, which are automatically calculated and applied by the CG-5 gravity meter, no other correction was applied to generate the observed gravity values. The Observed gravity map shows a gravity high value of 979280.1 mGal at the northwest and gradually decreases in an undulating pattern to a gravity low value of 979259.3 mGal at the southwest of the study area (Figure 27). These gravity data have been normalized and tied to a pre-established absolute gravity base station (IGSN 1971).

Subsequently, the gravity dataset obtained from PACES for the Houston region was gridded and an observed gravity map was created for comparison with an observed

gravity map from gravity field data. (Figure 28). A total of 42 gravity data points retrieved from the PACES database lie within the study area. The observed gravity map from PACES shows a gravity high value of 3303 mGal to the northeast and a gravity low value of 3256.1 mGal to the southwest portion of the study area (Figure 28). The highlighted black rectangle also shows an increase in gravity values to the northeast and a decrease in the southwest direction. This shows a similar pattern compared to collected gravity data, despite a relatively wide range of data spacing intervals between both gravity data sources. Although both observed gravity maps show some similarities in the gravity anomalies, the observed gravity map generated from the gravity data collected in the field shows detailed distribution in gravity anomalies, when compared to the observed gravity map generated from the PACES database. The difference between the maximum and minimum observed gravity values from field gravity data is 20.8 mGal (Figure 27), while gravity data from PACES database and within the study area is 20 mGal (Figure 28).

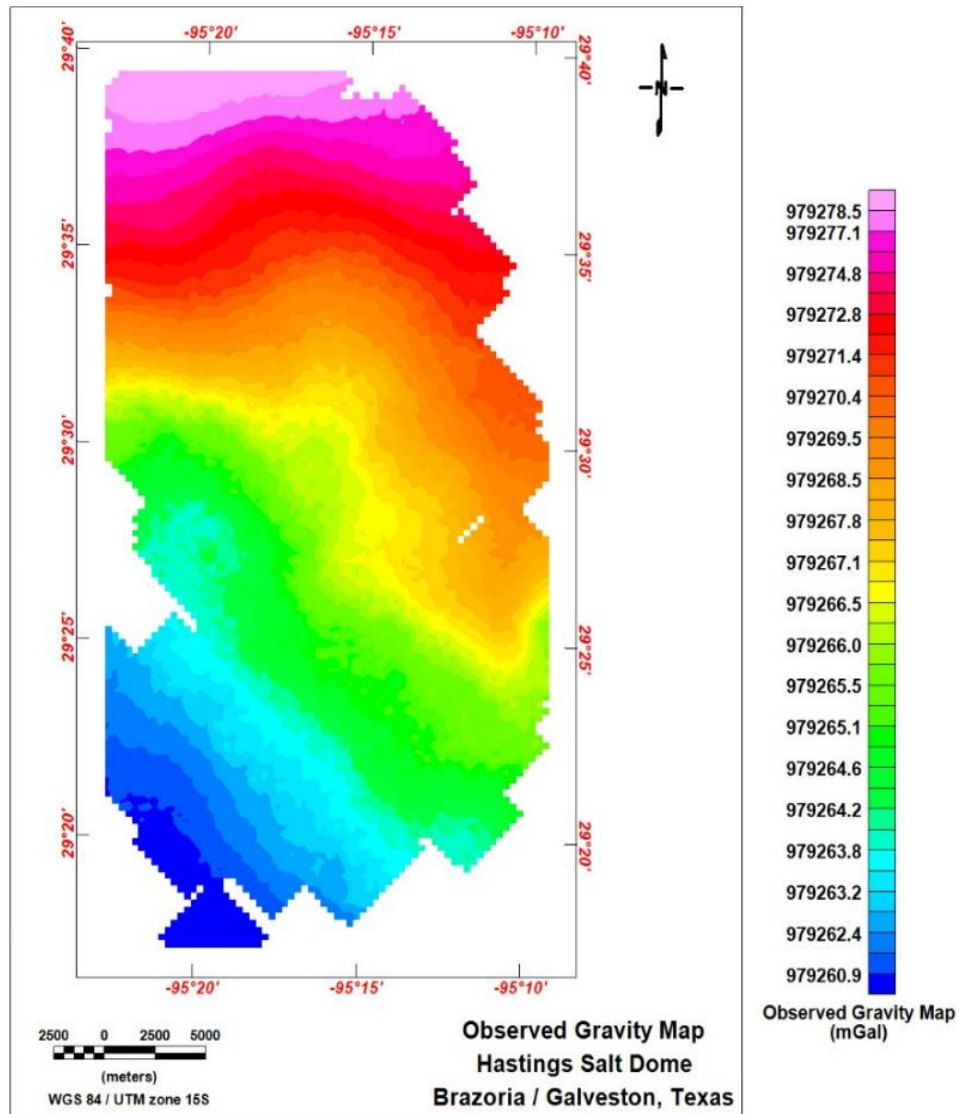


Figure 27 - Observed gravity map created from corrected gravity data collected in the field. High gravity values at 979280.1mGal are observed in the northern portion and gradually decrease towards the southwest with gravity low values at 979259.3mGal.

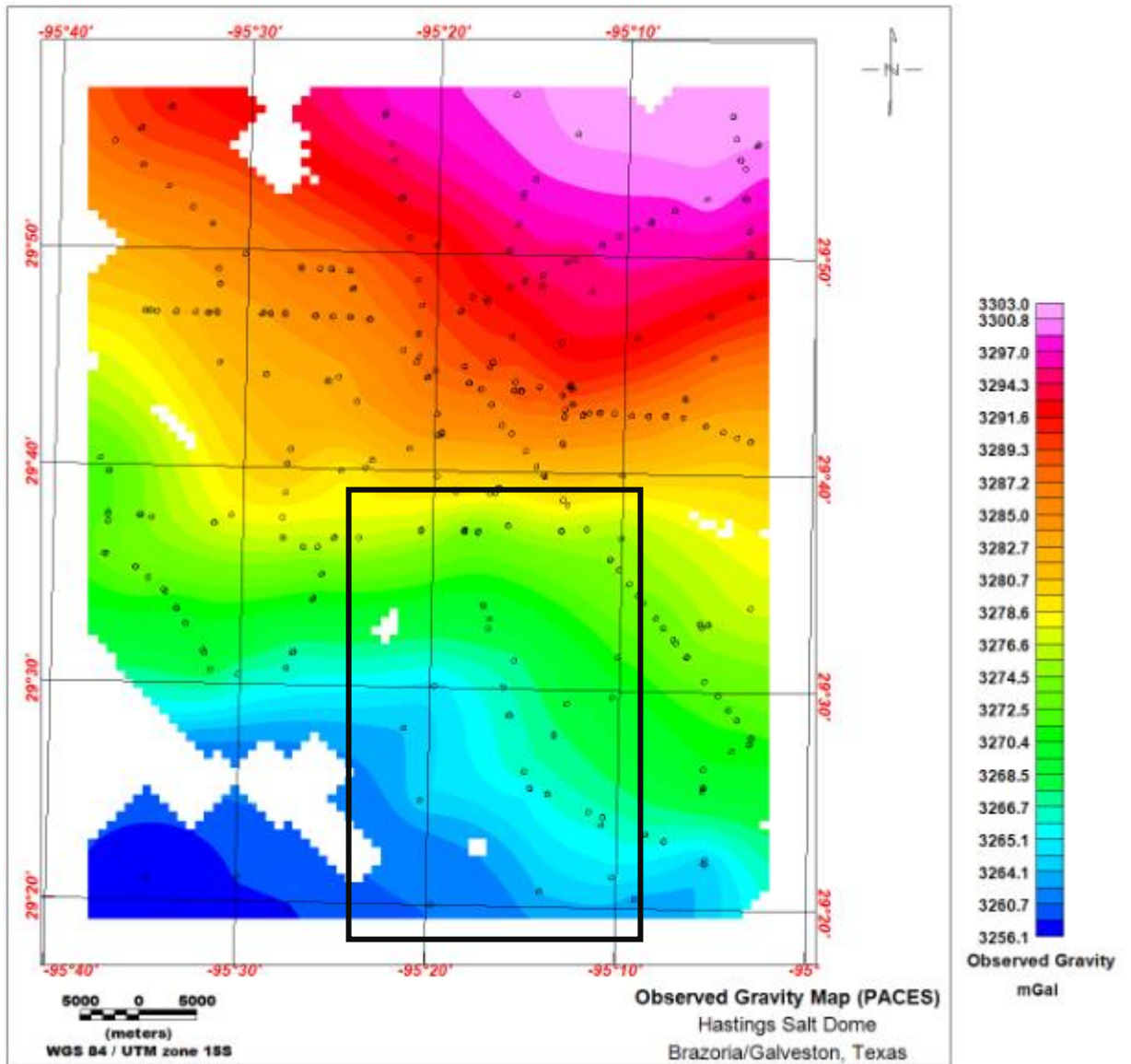


Figure 28 - Observed gravity map of Houston area created from gravity data collected from PACES database. Gravity high values of 3303 mGal are observed in the northeast which gradually decreased in a southwest direction to a gravity low value of 3256.1 mGal. The black rectangle shows the extent of the study area; 42 gravity data points lie within it.

THEORETICAL GRAVITY MAP

Theoretical gravity values were gridded to create a theoretical gravity map (Figure 29). The International Gravity Formula 1987 (Equation 2) was used to calculate theoretical gravity values. The resulting theoretical gravity map shows a gravity high value of 979298.2 mGal to the north and decreasing gradually southwards to a gravity low value of 979269.8 mGal (Figure 29). This observation is consistent with that fact that away from the earth's pole, gravity values decrease. This is due to the uneven radius from the center of the earth resulting in an increase in gravitational acceleration towards the earth's poles.

Subsequently, the gravity dataset from the PACES database for the Houston region was extracted and theoretical gravity values were calculated. The dataset was gridded to create a theoretical gravity map for the Houston region (Figure 30). The theoretical gravity map for the Houston region shows a gravity high value of 981064.8 mGal to the north and gradually decreasing southwards to a gravity low value of 980969.7 mGal (Figure 30). The two theoretical gravity maps generated show a similar gravity anomaly trend with increasing gravity values northward. This agrees with the theory that, away from the equator, gravity increases towards the poles.

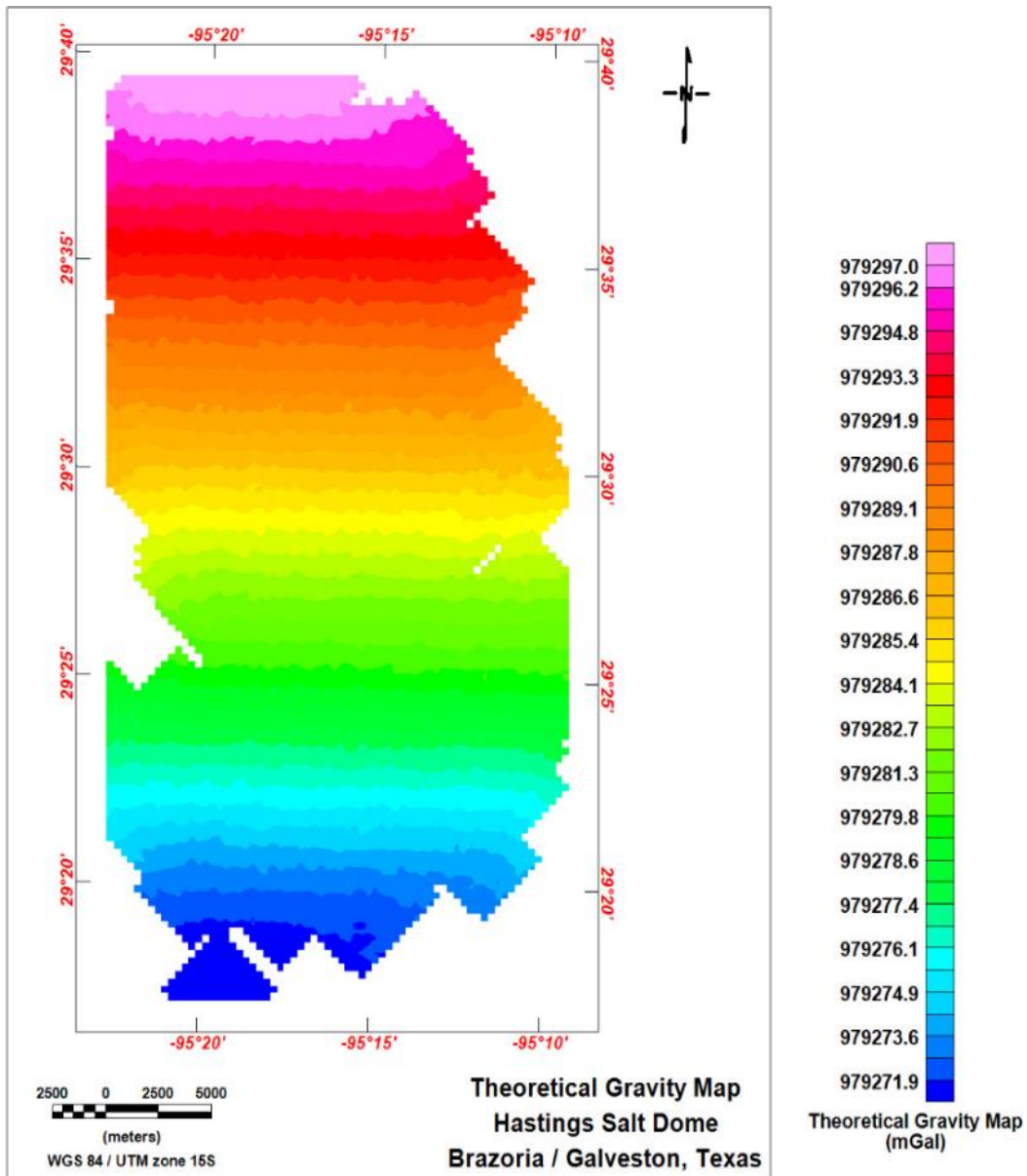


Figure 29 - Theoretical gravity map from gravity data collected from the field. High gravity values of 97998.2mGal are observed in the north and gradually decrease towards the southwest with a gravity low of 979269.8 mGal.

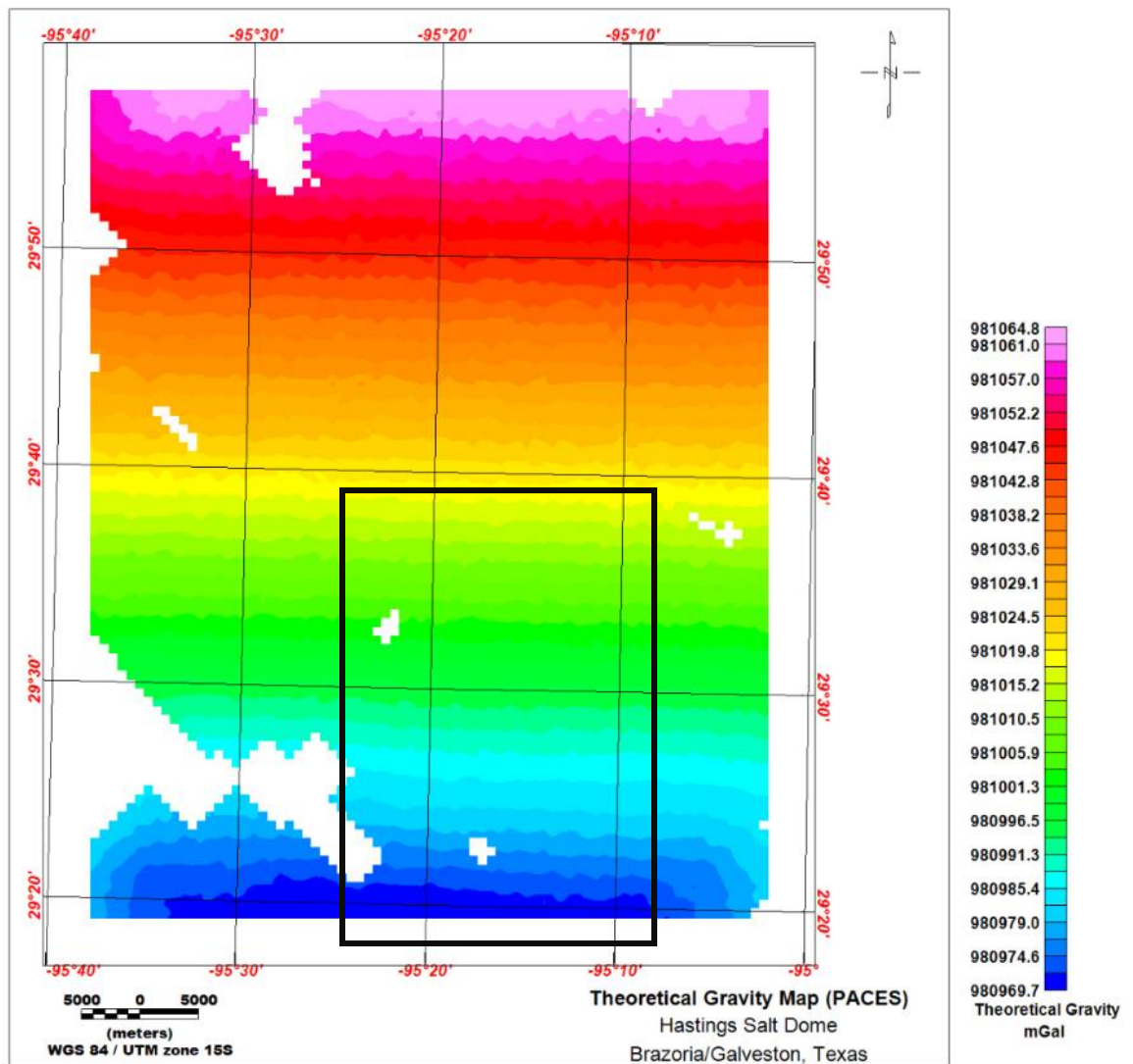


Figure 30 - Theoretical gravity map of the Houston area created from gravity data collected from the PACES database. Gravity high values of 981064.8 mGal are observed in the north portion and decrease gradually southwards with a gravity low at 980969.7 mGal. The black rectangle shows the extent of the study area.

RESIDUAL GRAVITY ANOMALY MAP

The residual gravity anomaly was calculated and gridded to create a Residual gravity anomaly map (Figure 31). The residual gravity anomaly was derived by subtracting theoretical gravity values from the observed gravity values. This shows gravity effects from shallow sources within a localized area, when effects due to regional gravity fields have been removed. Therefore, residual gravity anomalies are caused only by target structures when regional gravity effects have been removed (Figure 31).

The residual gravity anomaly map shows a gravity high value of -9 mGal to the west and north-center and a gravity low of -21.7 mGal in the southeast portion of the study area (Figure 31).

FREE-AIR GRAVITY ANOMALY

Free-air gravity anomaly values were calculated by using Equation 4. These values were gridded and used to create a free-air anomaly map (Figure 32). The free-air gravity anomaly map shows a gravity low value of -18.4 mGal to the northeast and increases toward the southeast portion of the study area with a gravity anomaly high value of -6.6 mGal (Figure 32).

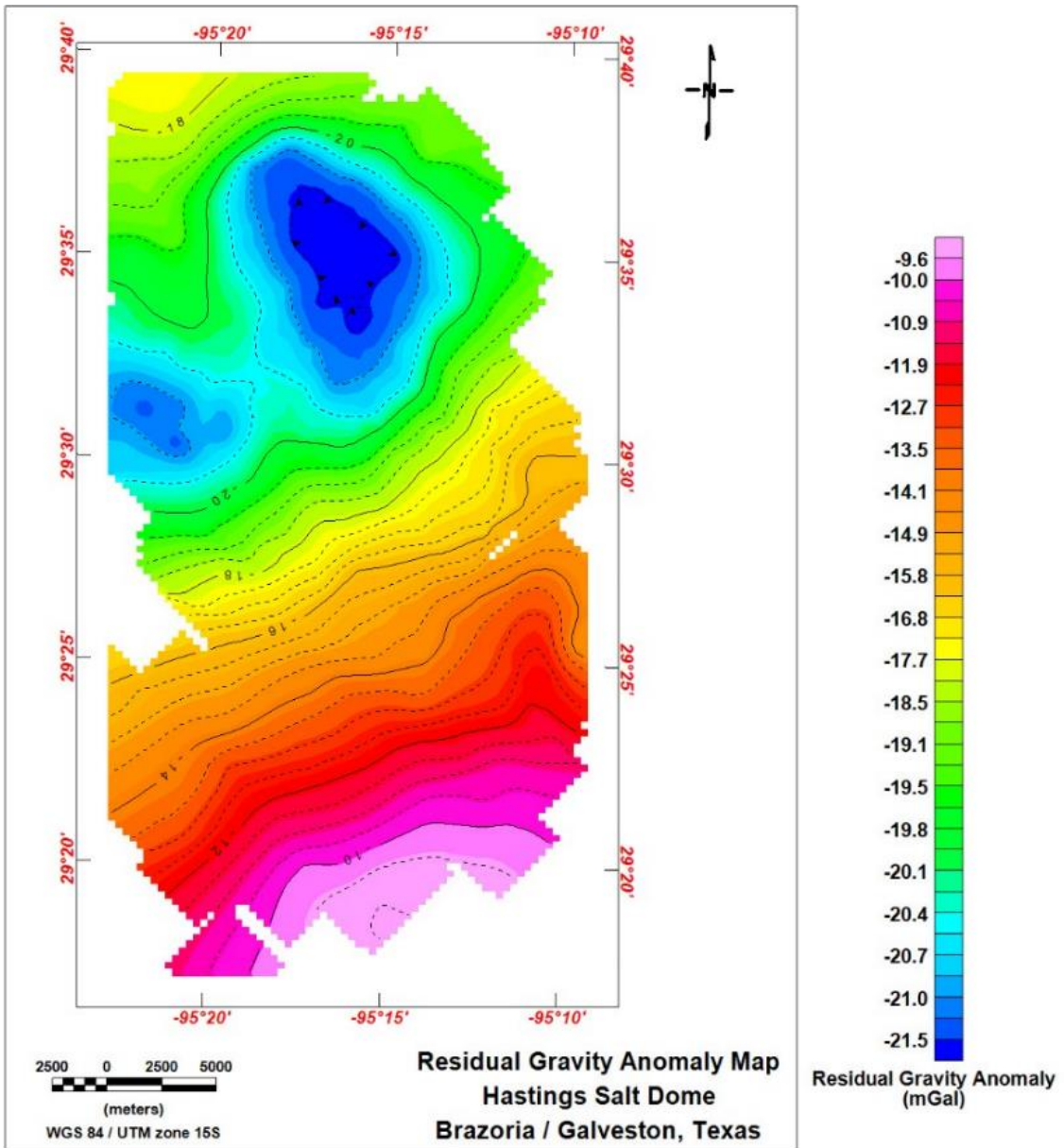


Figure 31 - Residual Gravity Anomaly map created from field gravity data. Gravity low anomaly value of -21.7 mGal occur in the north central and west portions and decrease southwards to a gravity high anomaly value of -9.9 mGal at the southeast end of the study area.

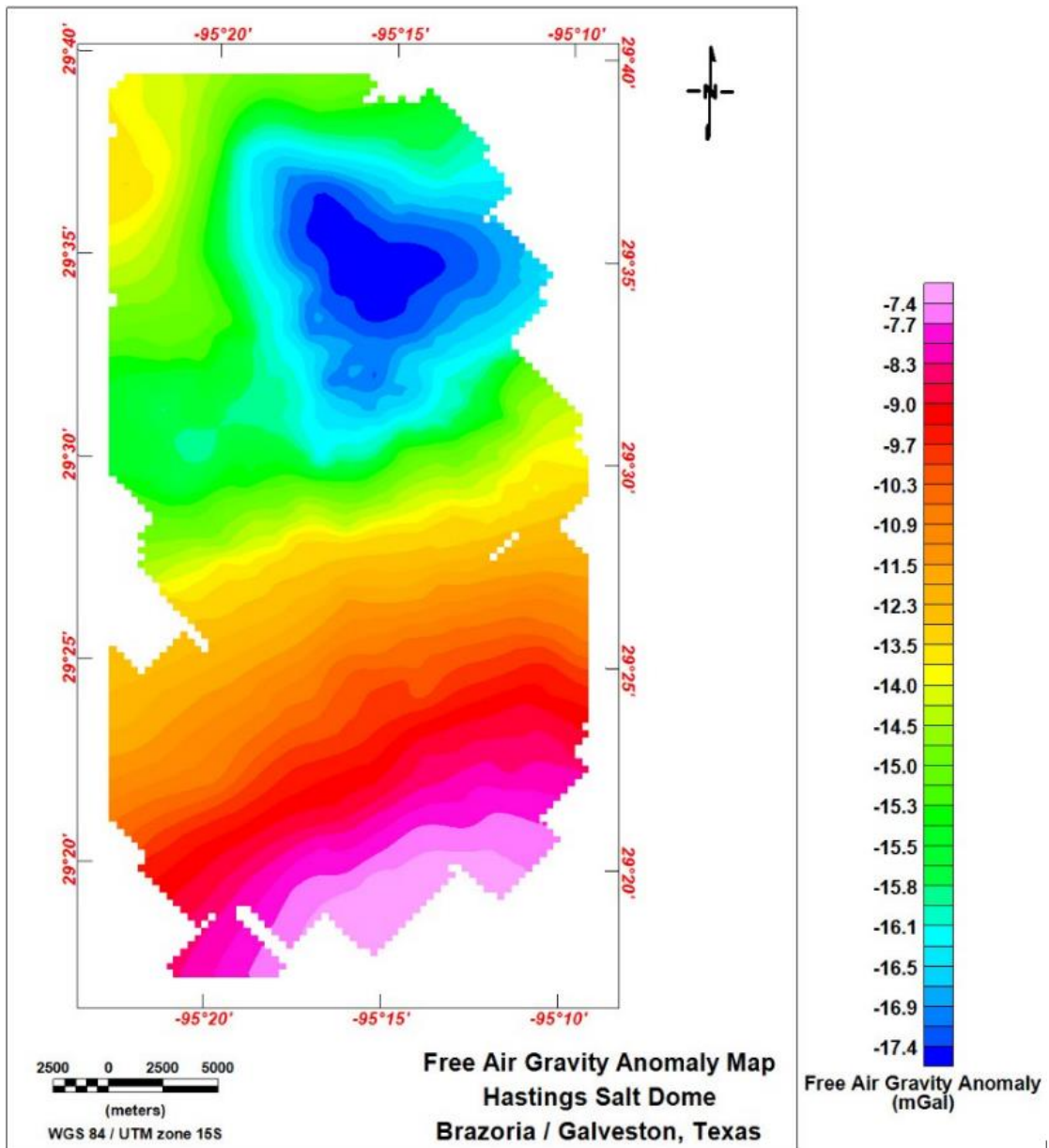


Figure 32 – Free-air gravity anomaly map shows gravity low anomaly values of -18.4 mGal at the northeast and increases in a southeast direction to gravity high anomaly values of -6.6 mGal in the southeast part of the study area.

BOUGUER ANOMALY MAP

One of the main objectives of this study was to create a Bouguer anomaly map of the study area, after all known gravity corrections were applied to the field gravity data. The corrected Bouguer anomaly data reflects lateral variations in rock's density at the subsurface (Figure 33). Bouguer anomaly (BA) can be calculated using the equation:

$$BA = G_{obs} - (G_n \pm FAC \pm BC) \dots \dots \dots \text{Equation 7}$$

Corrected gravity ($G_{corrected}$) refers to all corrections applied to the gravity dataset collected in the field and it is represented by this equation

$$G_{corrected} = G_n \pm FAC \pm BC$$

Hence, Bouguer anomaly is defined as the difference between the Observed Gravity (G_{obs}) and Corrected Gravity values ($G_{corrected}$) (Arafin, 2004). Therefore:

$$BA = G_{obs} - G_{corrected} \dots \dots \dots \text{Equation 8}$$

Bouguer gravity anomaly values were calculated and gridded to create a simple Bouguer anomaly map as shown in Figure 33. The term “simple” is used to classify the type of Bouguer anomaly derived, and this is because terrain correction was not applied to the gravity dataset. Terrain correction is generally applied to gravity readings collected in mountainous regions due to its effect on gravity. The study area has flat to low-lying topography; hence, terrain correction was not applied. The Bouguer anomaly map reveals two distinct concentrations of gravity lows in the study area. An oval-shaped, gravity low value range of about -24.5 mGal to -24.9 mGal is observed in the west portion of the

study area (Figure 33). The second gravity anomaly observed is near-oval in shape and it is located in the north-central portion of the study area. It has a gravity low value range of -24.9 mGal to -23.8 mGal. A similar pattern of the gravity low anomaly was observed in the residual gravity anomaly map. These gravity lows have been interpreted as Manvel (west) and Hastings Salt Dome (north-central), respectively.

Subsequently, gravity data from the PACES database for the Houston area was gridded and used to create a regional Bouguer anomaly map (Figure 34). This Bouguer gravity anomaly data represents the complete Bouguer anomaly data type because the gravity dataset was corrected for effect of terrain variations. A gravity low anomaly value of -17.9 mGal from the PACES dataset is observed in a similar location as on the data and was interpreted as the Hastings Salt Dome from the field data collected during this study (Figure 34 and Figure 33). A gravity low anomaly value of -17 mGal from the PACES dataset is observed over a similar location as the Manvel Salt Dome as interpreted in the Bouguer anomaly map that was created. Both distinct oval-shaped gravity lows anomalies have been interpreted as the location and extent of the Manvel and Hastings Salt Dome respectively (Figure 34). The Bouguer gravity anomaly increased gradually southwards, and a gravity high value of -10.4 mGal was observed in the southeast portion of the study area. An enlarged view of the gravity low anomaly interpreted as the Hastings Salt Dome is shown in Figure 35. These gravity low anomaly values range from -24.4 mGal to -24 mGal and are represented in blue (Figure 35). This shows us details of the density distribution of the Hastings Salt Dome.

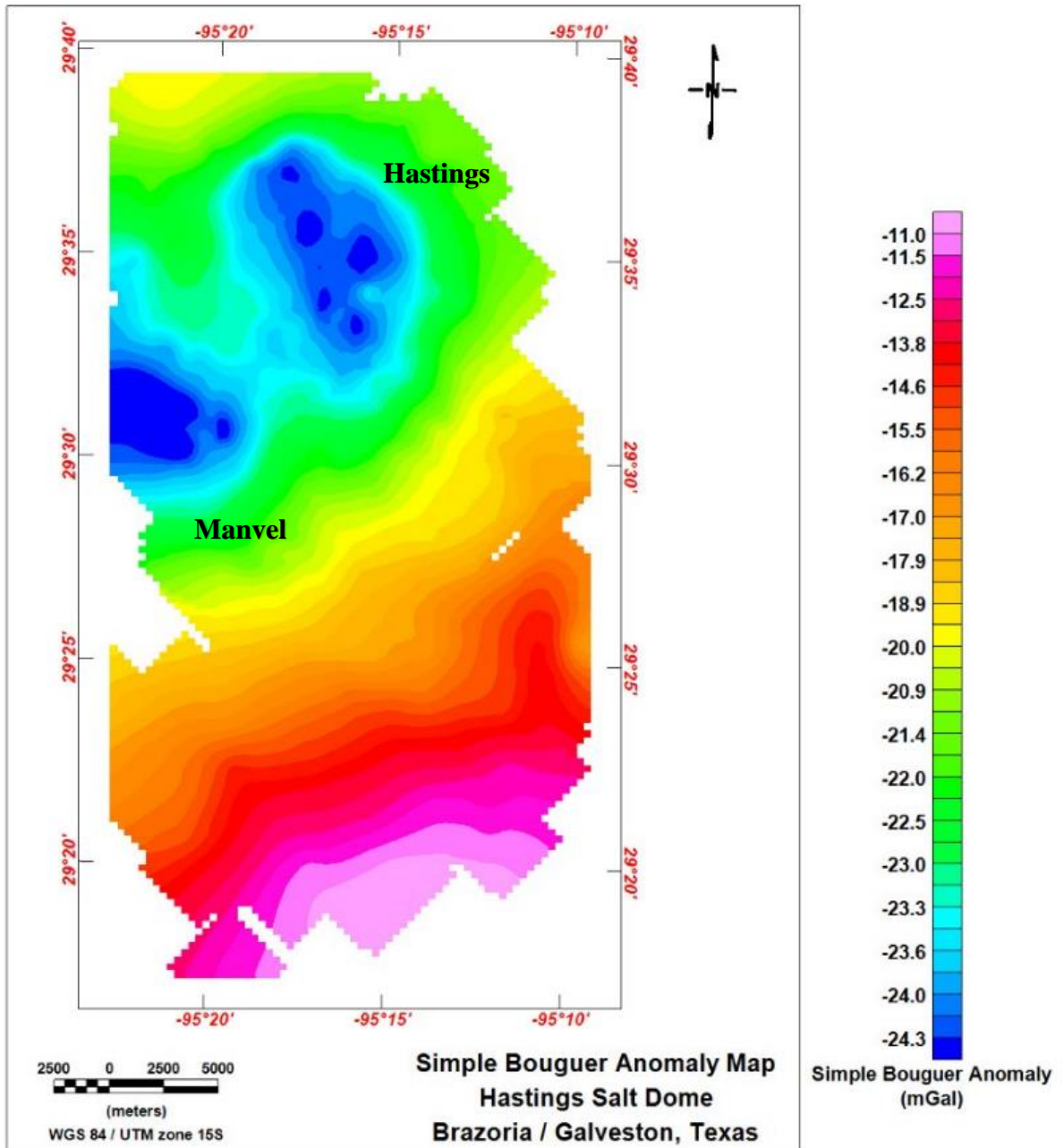


Figure 33 - Simple Bouguer anomaly map created from the gravity dataset collected from the field. Gravity low anomaly values ranging between -24.9 mGal to -23.5 mGal are observed at north-central and west portions of the study area. This has been interpreted as the Hastings and Manvel Salt Dome respectively.

A higher resolution version of the Bouguer gravity anomaly map was produced from our gravity dataset collected from the field compared to the Bouguer anomaly map created from the gravity dataset extracted from the PACES database. This is due to the relatively close data spacing interval and the total number of gravity data readings collected in this study. Having confirmed the position and extent of the Hastings Salt Dome, a structural map of the Frio Sandstone from the Hastings Oil Field was georeferenced and mapped (Figure 36). This was possible by using the Texas Land Survey Boundary shapefile downloaded from TNRIS database. This map reveals that the Hastings Oil Field is located on the south-eastern flanks of the Hastings Salt Dome (Figure 36).

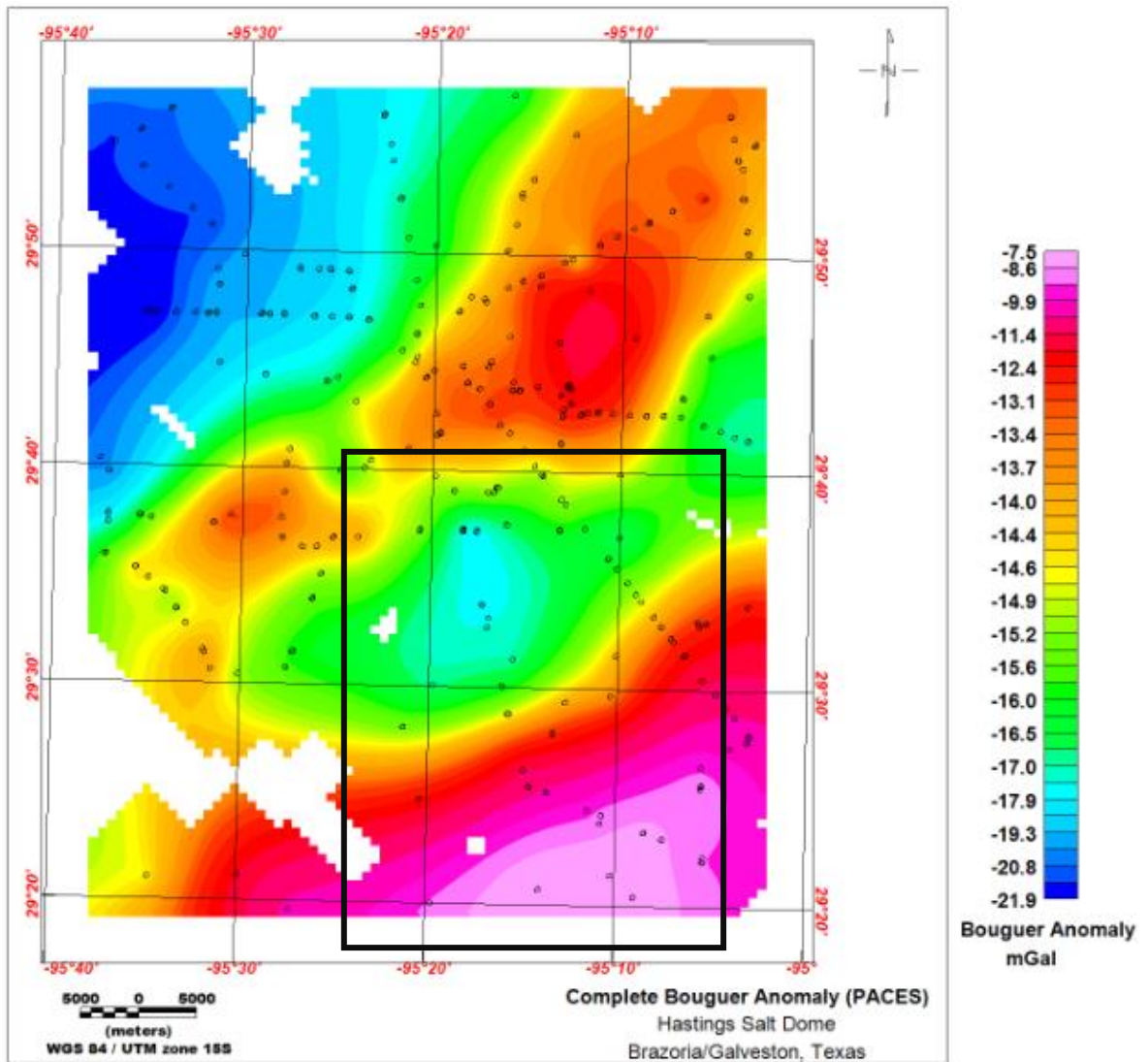


Figure 34 - Complete Bouguer anomaly map of Houston area created from the PACES gravity dataset. A black rectangle shows the extent of the study area and black circles represent gravity stations used to create the map. Note the wide-spacing gravity reading between gravity stations.

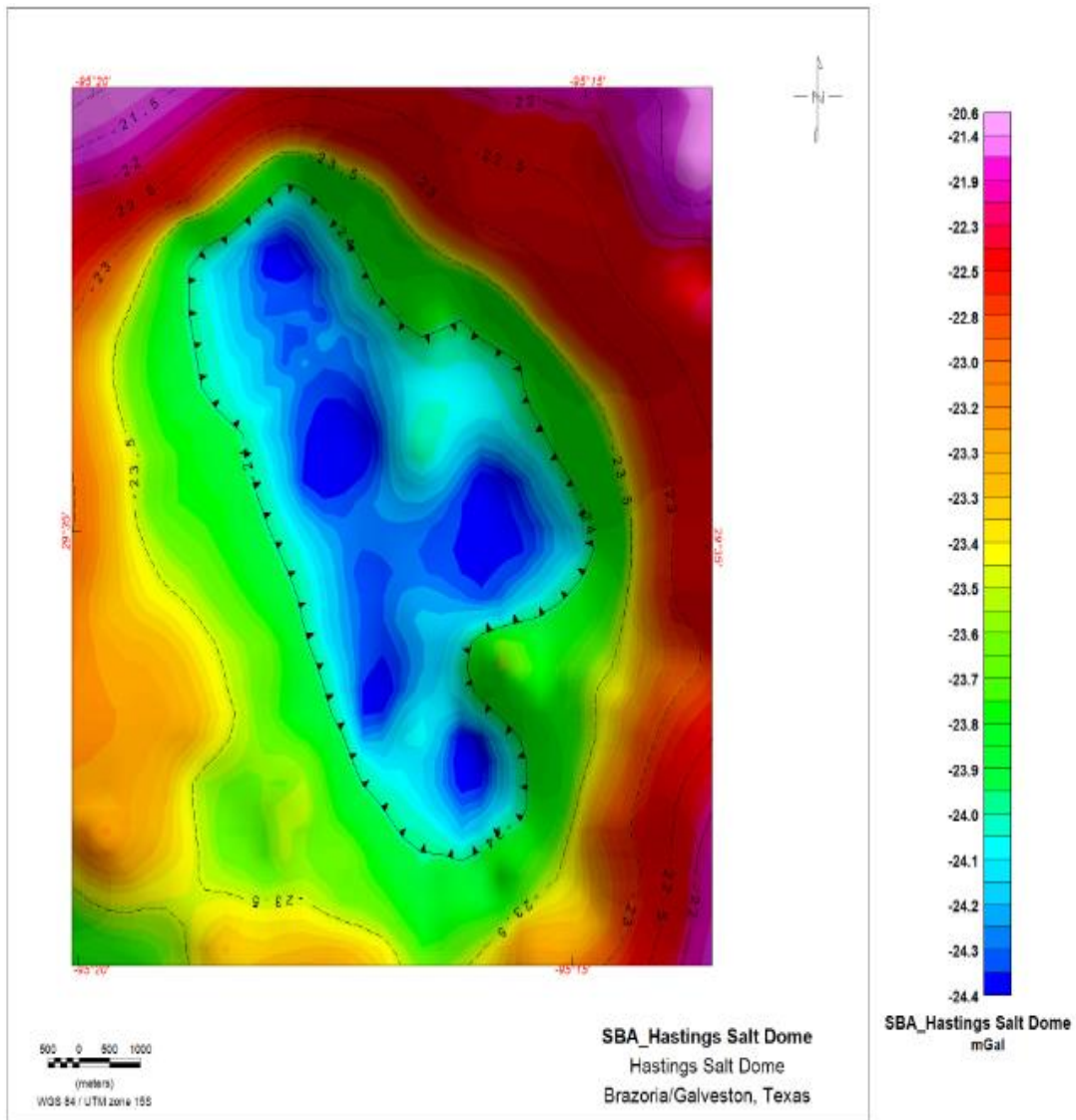


Figure 35 - An enlarged view of the oval-shaped, gravity low anomaly interpreted as the Hastings Salt Dome. The image shows the uneven distribution of density within the Hastings Salt Dome with five distinct loops of low gravity anomaly.

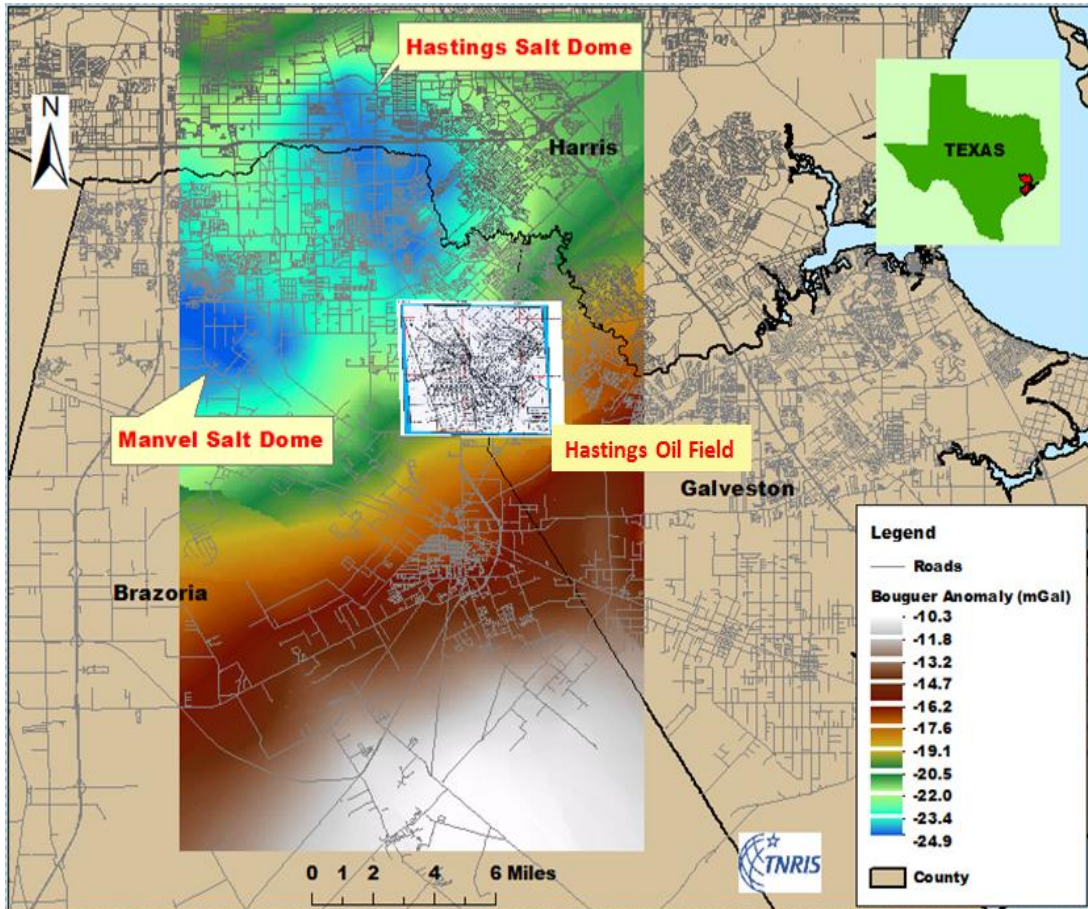


Figure 36 - Simple Bouguer anomaly map overlain on county and road network shapefiles using ArcGIS 10.3. It shows that the Hastings Salt Dome is located at the border between Harris and Brazoria Counties, while the Manvel Salt Dome is in Brazoria County. The Hastings Oil Field, as represented by the georeferenced structural map, is located on the south-eastern flank of the Hastings Salt Dome.

MAGNETIC ANOMALY MAP

The magnetic dataset that was extracted from the PACES database was gridded, and it was used to create a total magnetic intensity map of Texas (Figure 37). A total of 151 magnetic readings from the PACES dataset lie within the study area and this data were used to create a total magnetic intensity map of the study area (Figure 38). The magnetic data points are arranged in columns and rows (Figure 38) because the magnetic data was acquired in a traditional manner (i.e., in lines or grids) during an aeromagnetic survey with approximately 800 meters-line spacing (U.S.G.S. report, 2006).

The total magnetic map of Texas shows the distribution of measured magnetic intensities. Towards the southeast part of the magnetic anomaly map, a high intensity of magnetic anomaly values (ranging from -306.6 nT to -207.7 nT in the south coastal plain region of Texas) is observed (Figure 37). This anomaly extends from southwest to east of Texas and presumably into Louisiana. This high magnetic anomaly has been interpreted as the limit of the geosyncline or depositional basin, which consists of the Rio Grande Embayment, San Marcos Arch and Houston Embayment (Figure 37).

The total magnetic intensity map of the study area shows a high magnetic anomaly value of -240.8 nT to the north, with values decreasing gradually southwards to a low magnetic anomaly value of -417.1 nT in the southeast portion of the study area (Figure 38). Both magnetic and gravity geophysical survey methods involve passive measurements of the earth's naturally occurring magnetic and gravitational fields.

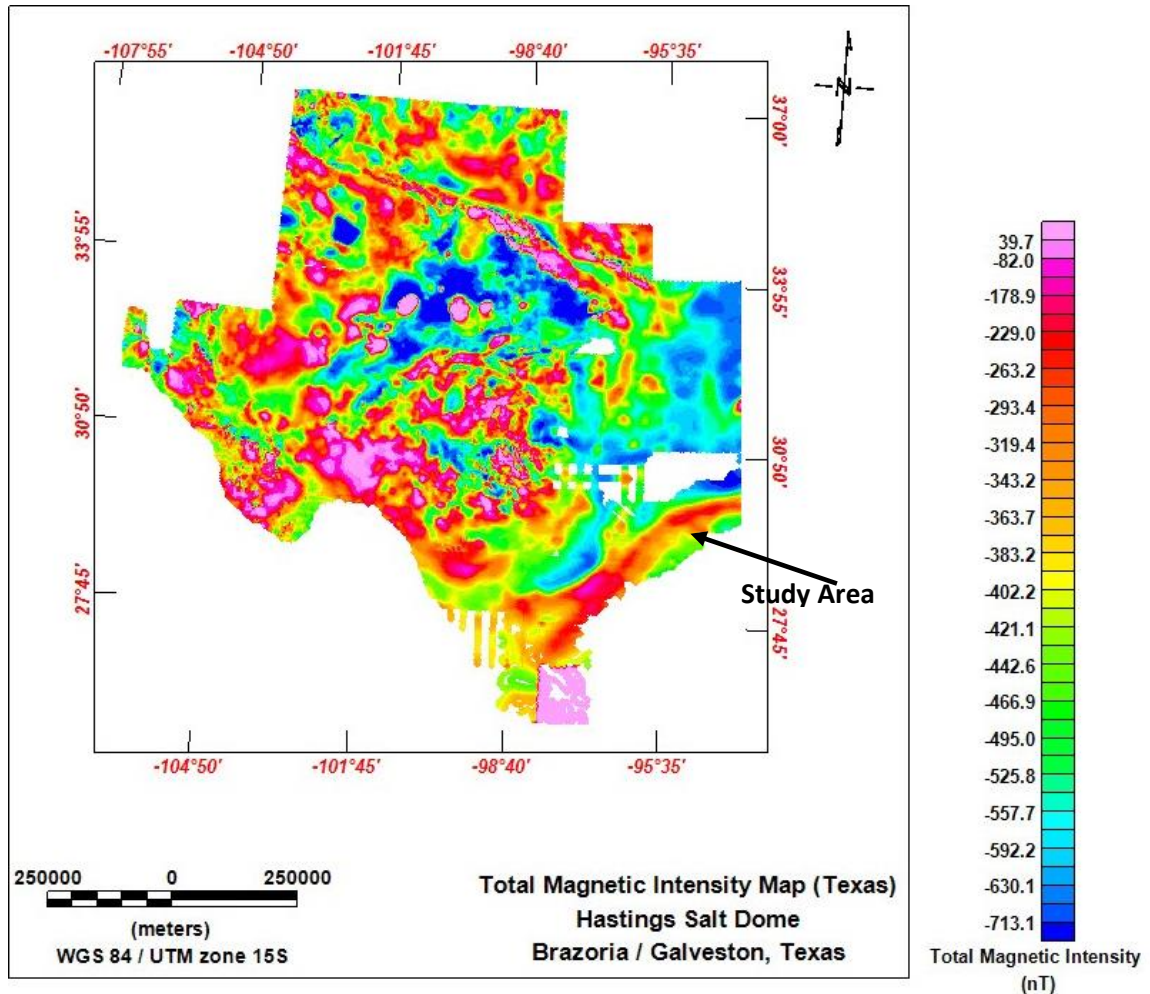


Figure 37 – The total magnetic intensity map of Texas showing the distribution of magnetic anomalies. A black arrow shows the approximate location of the study area. Magnetic data was extracted from the PACES database. The northern edge of the Gulf of Mexico geosyncline is located to the southeast of the map and represented by an eastward trending magnetic anomaly.

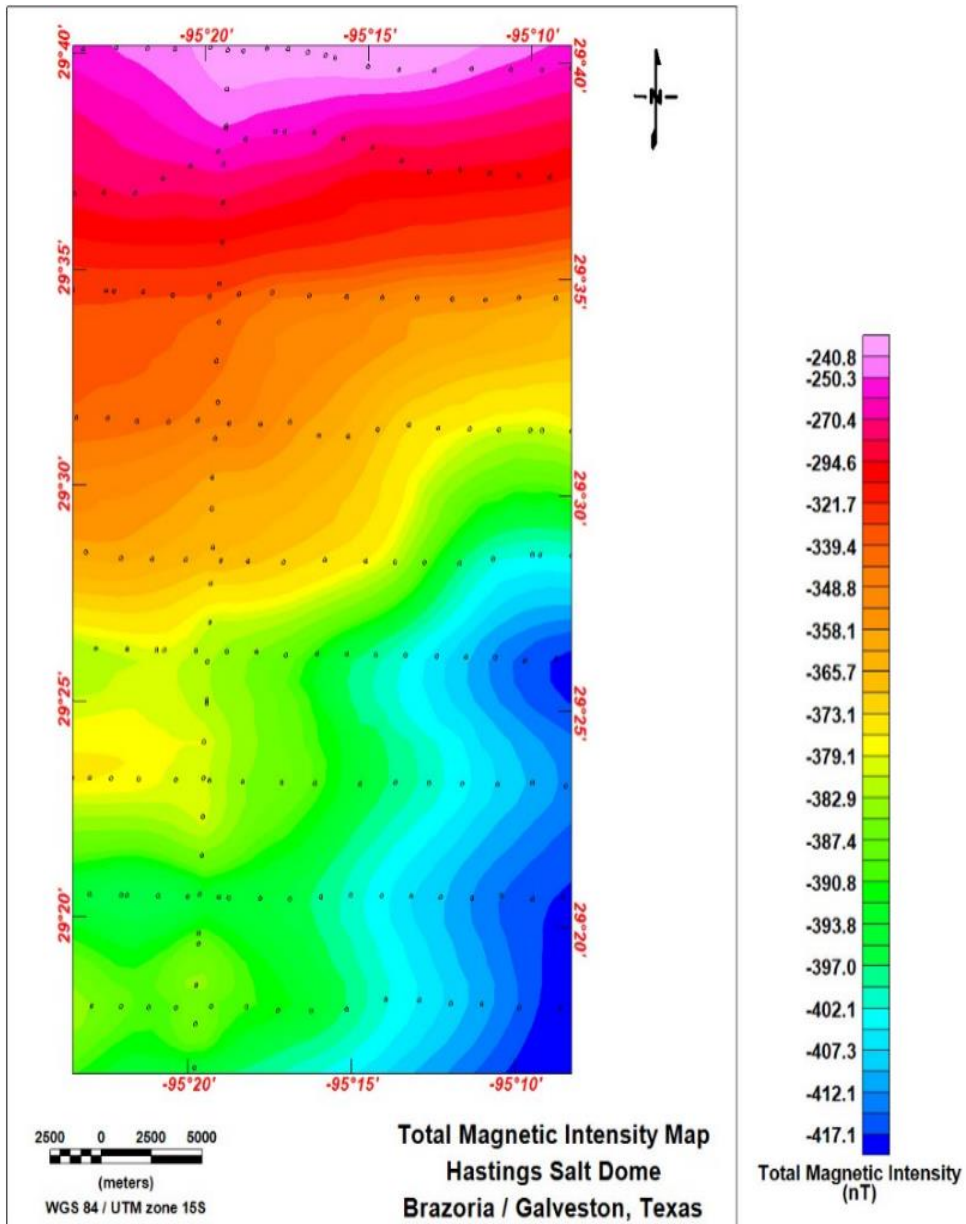


Figure 38 - Total Magnetic Intensity map of the study area. High magnetic values at -240.8 nT are observed at the north and gradually decrease southwards to an abrupt magnetic low at the southeast at a value of -417.1 nT is observed. The black circles represent the location where the magnetic field was measured.

WELL LOG INTERPRETATION

Two units, the Miocene Shale unit and the Frio Shale of the Frio Formation were present on several well logs and were correlated based on similarities in their petrophysical characteristics to create a cross-section (Figure 39). Eleven well logs were correlated and utilized to create a stratigraphic column based on the self-potential, gamma, and resistivity curves (Table 1). Wells #1 and #2 are in Harris County, and the remaining nine wells are in Brazoria County (Figure 23). Well #2 through well #7 lies within the study area (Figure 23). A cross section was drawn between these wells to examine the effect of salt diapirism in subsurface rocks. This cross section extends from well #1 in the Pierce Junction oil field to well #2, located over the Hastings Salt Dome in Mykawa Oil Field, through to wells #3-5 which are located over the Hasting Oil Field, to well #10 and 11, which are over the Danbury Salt Dome in Danbury Oil Field (Figure 23) and Figure 39).

The general gulfward, southeast dip of sedimentary beds is influenced by the shape of the Gulf of Mexico (GOM) geosyncline, where a thick accumulation of sediments were deposited (**Figure 5**). Well #1 is an oil well in Harris County and it is associated with the Pierce Junction Salt Dome. The Pierce Junction Salt Dome has been interpreted and classified as a shallow salt dome because the salt dome is encountered at the depth of 289.5 meters (950 feet) from the center of the dome (Glass, 1953). From the cross section created, the diapiric effect of the Pierce Junction Salt Dome as observed in well #1, shows both uplifted Frio and Miocene Shale beds (Figure 39). Well #2 is located in the northern portion of the Hastings Salt Dome (as observed from the Bouguer

anomaly map created in Figure 36) in Mykawa Oil Field. The Frio Shale unit shows the effect of uplift, while the Miocene Shale unit does not show an uplift effect. In well #2, the Miocene Shale unit is approximately 1,300 feet thick; it is thickest when compared with surrounding correlated wells (Figure 39). Also, showing in well #2, the sedimentary units in between the Frio and Miocene Shales is the thinnest among correlated wells. This could be as a result of sediment compaction due to the overburdened thickness of the overlying sedimentary beds. This observation could support and explain the occurrence of subsidence in this region (Figure 39). Well #10 and well #11 are located in Danbury Oil Field, and are associated with Danbury Salt Dome (Figure 23 and Figure 39). The Frio Shale unit shows uplift which occurred as a result of the uprising Danbury Salt Dome (Figure 39).

A structural map (Figure 40) created shows the depth to the top of the Frio Shale along the cross section. This structural map shows that the shallowest depth to the top of the Frio Shale occurred at well #1, which is to the northwest in the cross section, and depth increased to the southeast towards well #9 and reached a depth of 6,300 feet (Figure 40). An isopach map was also created to show the thickness of the Frio Shale (Figure 41). Well logs from well #1 and well #2 were not logged to the base of the Frio Shale, hence, the isopach thicknesses of the Frio Shale in well #1 and well #2 could not be calculated (Figure 41). The isopach map is based on the data available, and shows that the Frio Shale is thinnest in wells located in the Hastings Oil Field. Well #4 is located in the Hastings Oil Field and has an approximate thickness of 540 feet and is located east of the cross section, where it is thinnest (Figure 41). In well #8, the Frio Shale unit is

thickest with a thickness of 1,950 feet; it is in the southeast of the cross section (Figure 41).

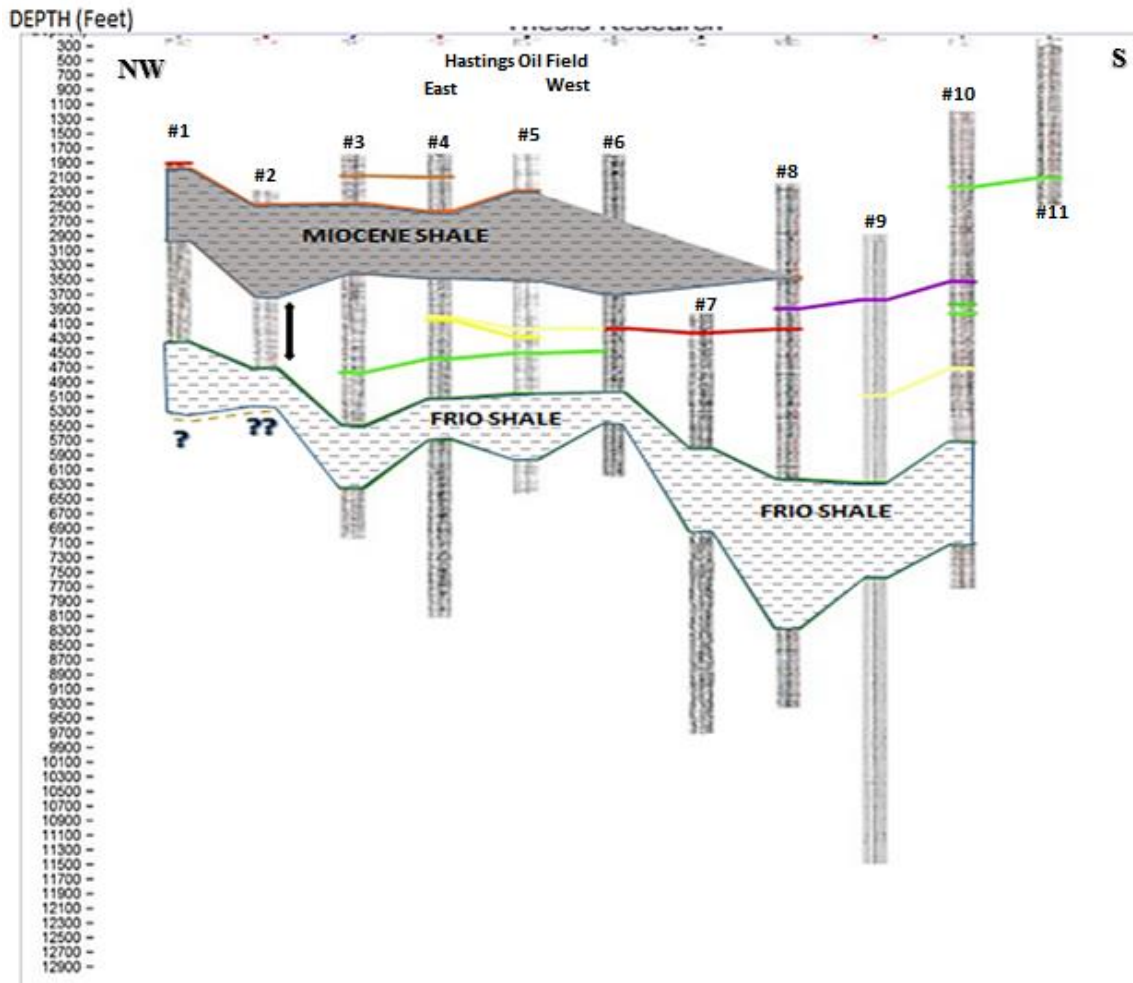


Figure 39 – This cross section shows the correlation between the Frio and Miocene Shales. In well #2, the sedimentary beds between the Miocene and Frio Shales show evidence of sediment compaction. This observation can explain the subsidence within this region. Cross section can be found in Figure 23.

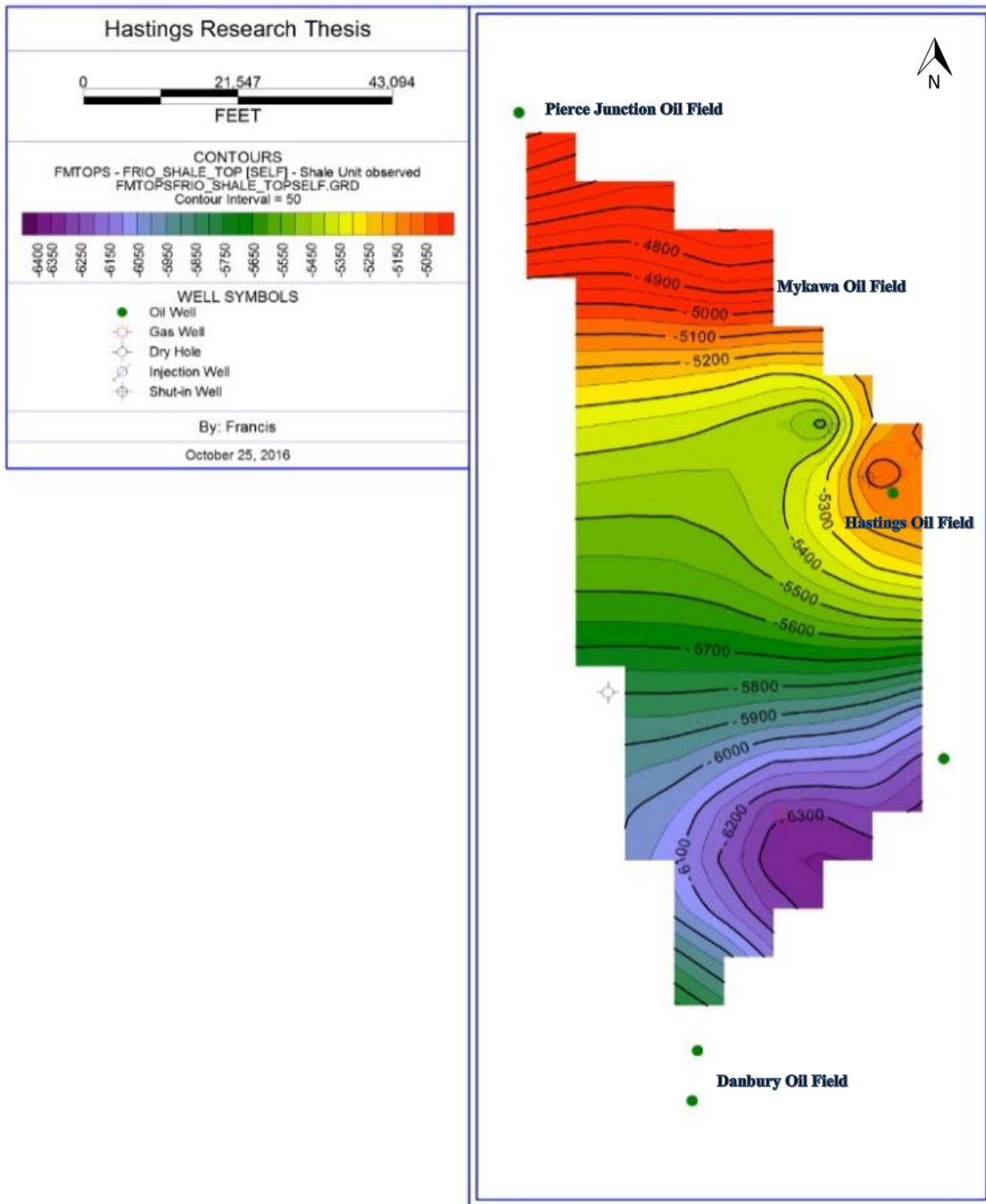


Figure 40 - Structural map of the top of the Frio Shale. This shows a southeasternward increase in depth to a maximum of -6,300 feet in well #9. Generally, the depth of the Frio Shale gets deeper towards the Gulf of Mexico.

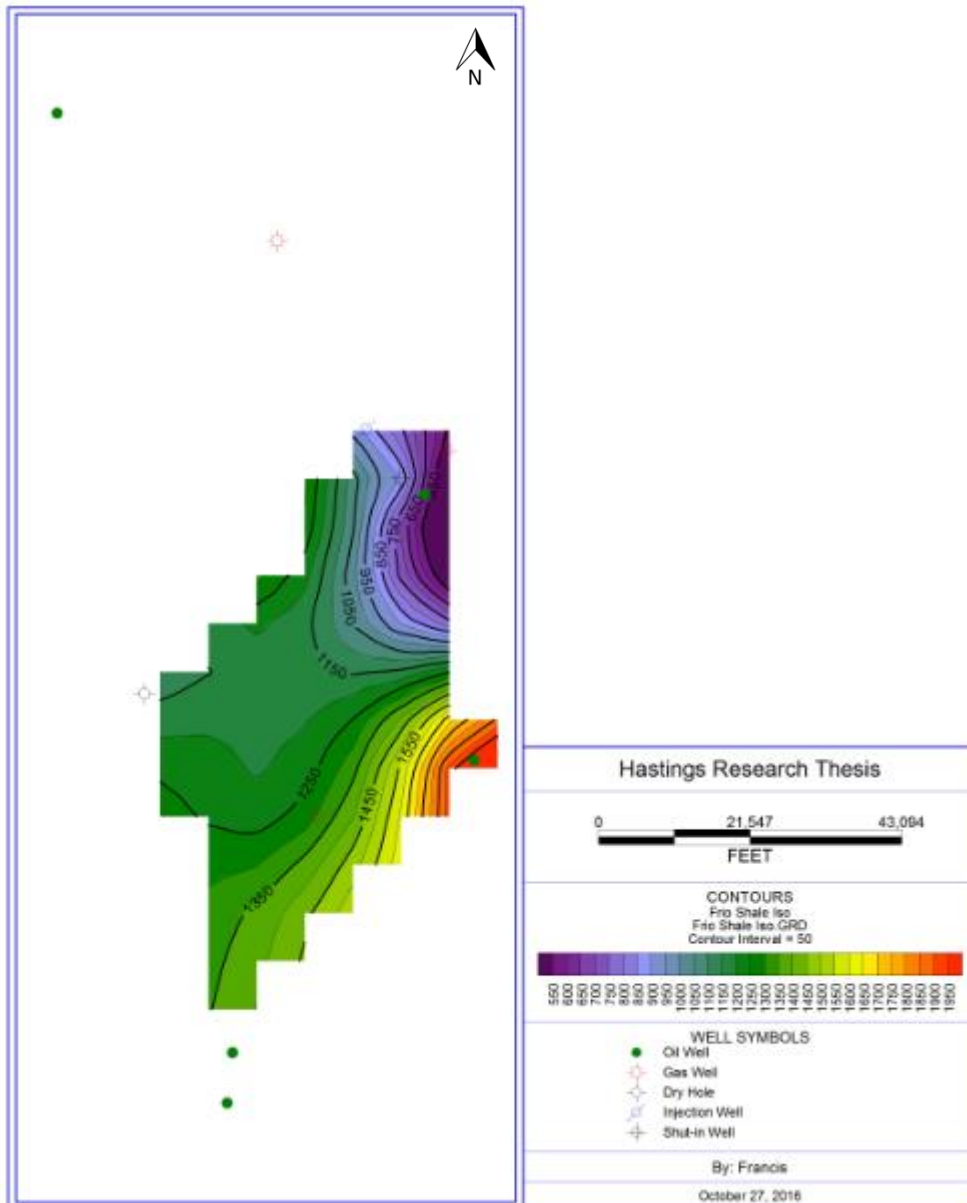


Figure 41 - Isopach map showing the distribution of thickness of the Frio Shale. Well # 4 shows the least thickness of approximately 540 feet, while the maximum thickness occurred at well #8 with a thickness of 1,950 feet south-east of study area.

ESTIMATING THE DEPTH TO HASTINGS SALT DOME

The depth to the Hastings Salt Dome can be estimated by applying the half-width equation to the gravity low anomaly from the Bouguer anomaly gravity map shown in Figure 33. This technique is applied to estimate the depth of a subsurface feature using spherical geometry; e. g., depth to salt domes. The depth estimation is however important, since the depth of the Hastings Salt Dome is unknown. The geometry of salt domes differs widely and is dependent on factors such as buoyancy and differential offloading of overlying sediments.

The concept of the half-width equation technique shows that the vertical component of gravity measured (g_z) has a maximum value at the center of a sphere where x (distance) is zero. The half-width equation technique is used to estimate the depth of the Hastings Salt Dome as shown by this equation.

$$z = 1.305x_{1/2} \dots\dots\dots\text{Equation 9}$$

In this equation, z is the depth to the center of the sphere and $X_{1/2}$ is half of the horizontal distance of the anomaly.

This equation can be applied to estimate the depth to the Hasting Salt Dome. The minimum and maximum Bouguer gravity anomaly values of the Hastings Salt Dome are -24.4 mGal and -23.8 mGal respectively. The center of the vertical boundary limit is 5.3 km, which lies along N29°35' latitude line. The center of the horizontal boundary limit and along the pre-established vertical boundary line is 3 km. In other words, 3 km is

the estimated half-width value to the outer boundary of the Bouguer gravity anomaly of the Hastings Salt Dome. At this point, which is the center of the gravity low, $x = 0$ and the vertical component of gravity (g_z) is maximum.

Therefore:

$$z = 1.305 \times 3 = 3.915 \text{ km}$$

The estimated depth to the Hastings Salt Dome is 3,915 meters (12,840 feet). According to Halbouty's (1967) classification of salt domes based on salt piercement and depth of burial, the Hastings Salt Dome is classified as a deep-seated salt dome occurring at a depth below 1,800 meters (Figure 10). Unfortunately, there is no well log available over or around the Hastings Salt Dome to compare it with the estimated value calculated from using the half-width equation method. Well log API 4203933055 has the greatest depth of penetration ranging from 4,380 meters (14,000 feet) to a total depth of 5,270 meters (17,290 feet). This well was a wildcat and was a dry hole. This well is located to the south and outside of the study area along longitude W -95.32997 and latitude of N 29.417635.

CREEKOLOGY

Creekology is an old technique that is based on the relationship between flow pattern of creeks and relative to structural highs. A supervised, classified land-cover map was created using Landsat 8 satellite imagery (Figure 42). The land-cover map was

classified into 6 classes; water body, urban settlement, bare-ground surface, roads, thick vegetation and agricultural fields (Figure 42). The concept of creekology was applied to the land-cover map (Figure 42), DEM (Figure 43), and Bouguer gravity anomaly map (Figure 44). A shapefile containing information on creeks and rivers within the study area was used. This shapefile was downloaded from TNRIS and it was overlain on each of the three maps created. Observations on the relationship, extent and direction of the flow of a creek and relative to the topography are crucial when applying the concept of creekology. This is observation reveals the presence of possible subsurface geology feature.

The land cover map shows that the northern portion of the study area is mostly dominated by urban settlements, while the southern portion consists mostly of agricultural fields. Clear Creek forms the borders south of Harris County and north of Brazoria and Galveston counties (Figure 42). Clear Creek and Dickinson Bayou flows in a west to east direction towards Trinity and Galveston Bay, while Chocolate Bayou, Mustang Bayou, and Austin Bayou all flow in a northwest to southeast direction towards the Gulf of Mexico.

Information on climatic and weather reports was reviewed from the National Oceanic and Atmospheric Administration (NOAA) / National Weather Service webpage for the Houston Hobby region. This data shows that the precipitation rate (rainfall) for the months prior to when the satellite image was taken was below normal (NOAA, 2016). This explains why the full extent of the surface water bodies (creeks) was partially detected in the classified land-cover map; however, the shapefile containing information and spatial distribution of rivers and creeks was utilized.

The Digital Elevation Model that was created shows the general terrain surface of the study area (Figure 43) and the concept of creekology was applied. High elevations are observed to the west and northwest of the study area and are generally decreasing in an eastern and southeastern direction towards Galveston Bay and the Gulf of Mexico (Figure 43). The regional flow direction of the creeks is controlled by the decrease in elevation towards the Gulf of Mexico; changes in local flow pattern may be controlled by subtle changes in topography (Figure 43).

The concept of creekology was also applied to the Bouguer anomaly map determine for the local response of creeks over gravity lows anomalies interpreted as the location of the salt domes (Figure 44). Towards the western portion of the study area and over the location of the Manvel Salt Dome, the Dickinson Bayou responded to the presence of the Manvel Salt Dome by meandering and wrapping around the region of the gravity low anomaly (Figure 44). This observation supports the presence of a surface imprint as a result of the uprising of the Manvel Salt Dome. On the other hand, the Clear Creek flowed across the gravity low anomaly interpreted as the Hastings Salt Dome. This flow pattern of Clear Creek around the gravity low anomaly mimics the disseminated distribution of the gravity low anomaly within the Hastings Salt Dome (Figure 44). Towards the east portion of the gravity low anomaly, Clear Creek can be seen meandering and then wrapping around the southeast portion of the Hastings Salt Dome (Figure 44). This seems to support the idea that the Hastings Salt Dome created a positive uplift at the surface, even though the salt dome is classified as a deep-seated feature.

A fault dataset containing different fault types was retrieved from TNRIS database and the data specific to the study area was extracted. When mapped, a series of normal faults was displayed above and around the Hastings Salt Dome (Figure 45). These normal faults may have formed during the uprising and formation of Hastings Salt Dome due to the extensional stresses generated in the overlying sedimentary rocks (Figure 45).

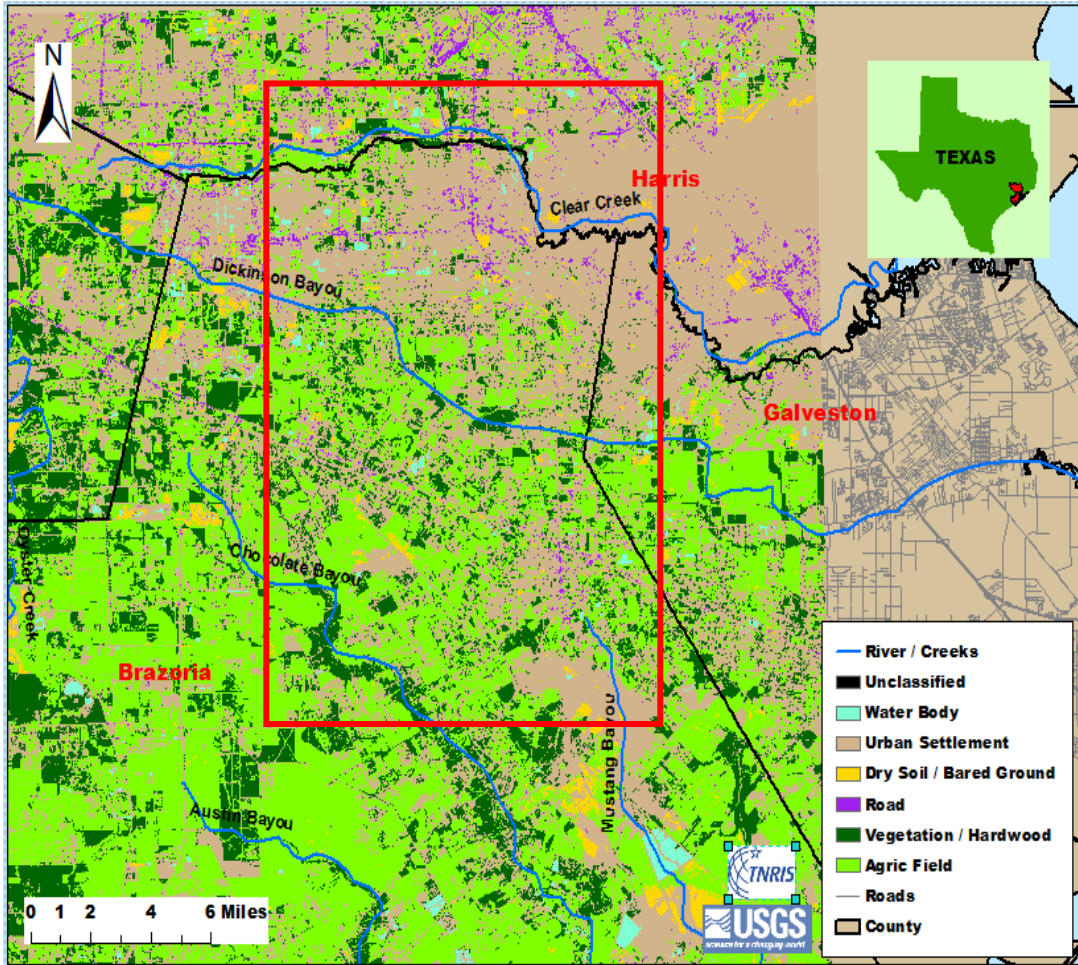


Figure 42 - Land Cover map showing a high concentration of urban settlement to the north and northeast and more agricultural activity in the south and southwest. The study area is highlighted in red.

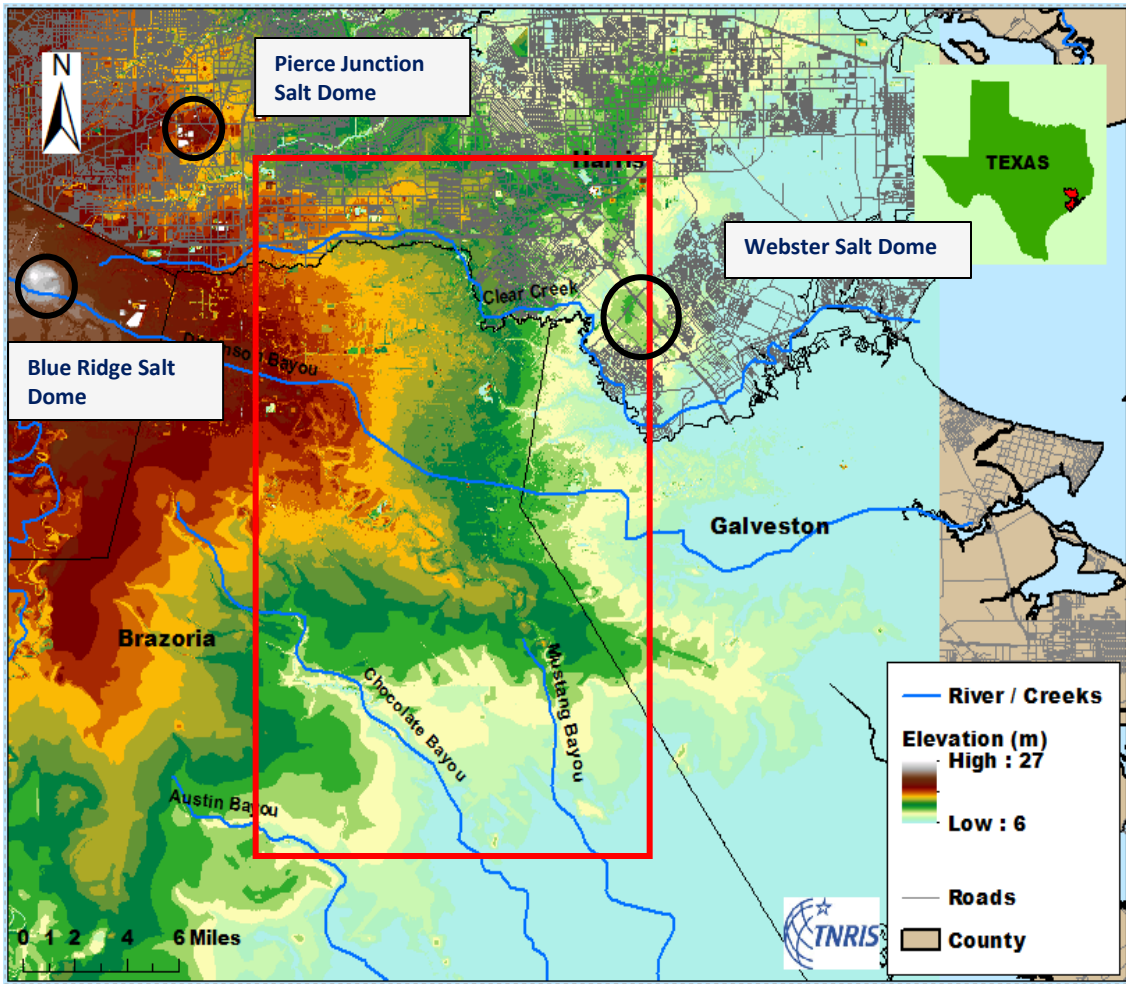


Figure 43 - Digital Elevation Model showing the distribution of elevation. The creeks are controlled by the general topography of the region. The study area is highlighted in the red rectangle. Isolated elevation highs (represented in the black circles) show probable surface imprints of salt dome diapirism for the Blue Ridge, Pierce Junction and Webster Salt Domes.

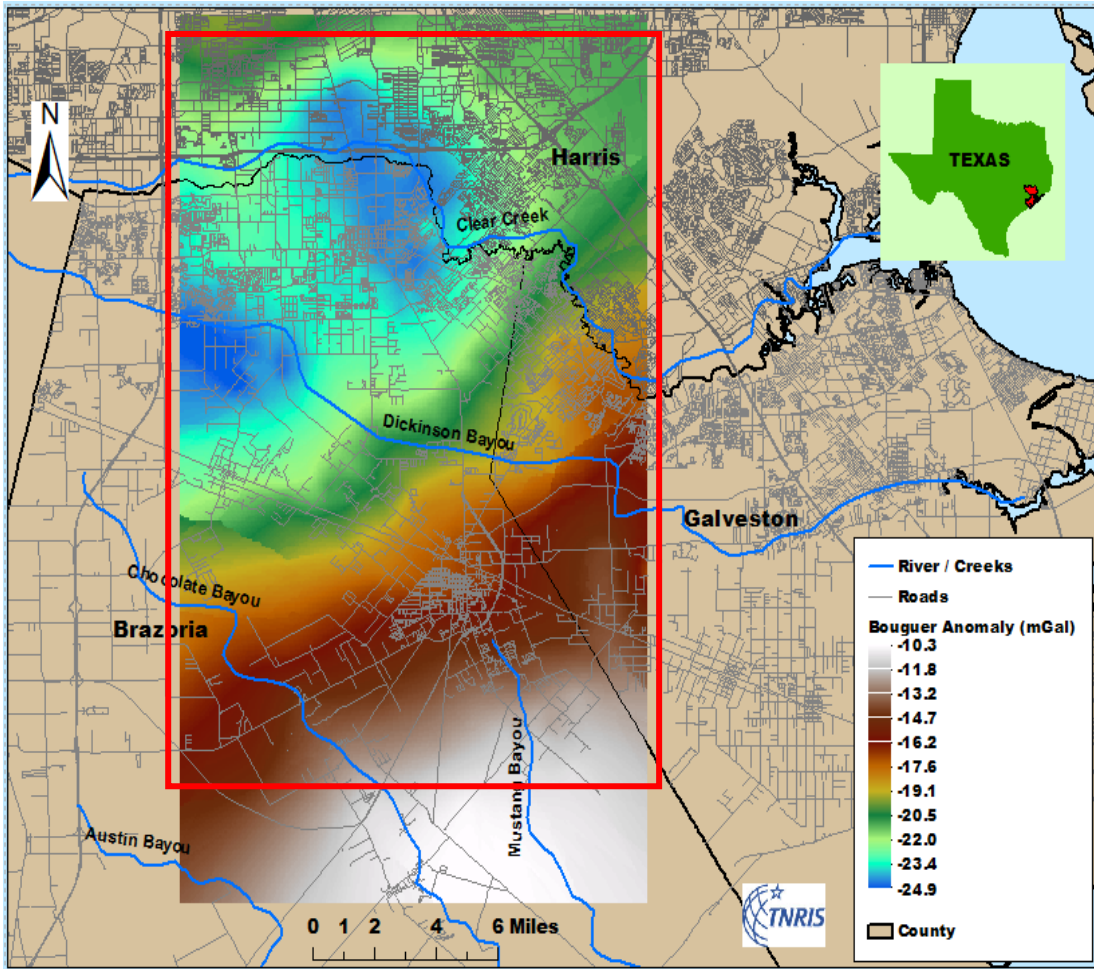


Figure 44 – Map showing the local effect salt domes and the flow pattern of the creeks around the domes. In the west of the study area, the Dickinson Bayou responds to the presence of the Manvel Salt Dome by wrapping around it. Clear Creek flows across the Hastings Salt Dome but wraps around it towards the east portion of the salt dome. The study area in red rectangle and salt domes are represented in blue (gravity low anomaly).

GRAVITY MODEL

Three 2D gravity models were created from cross sections over the Bouguer gravity anomaly map (Figure 46). These gravity models were generated using a GM-SYS module, an extension of the Geosoft Oasis Montaj (version 9.0) software. GM-SYS allows its user to create 2D hypothetical geology models which depict the subsurface geology along the selected cross-section. Rock densities are assigned to each rock layer represented and these rock layers are modified so that the observed gravity curves match up with the calculated gravity. This was achieved by adjusting nodes assigned to a rock layer. These nodes responded simultaneously based on the rock layer's gravity and magnetic properties. The magnetic dataset was used as an additional control to constrain the hypothetical gravity model based on the assigned rock's density and magnetic susceptibility properties. To successfully construct a more realistic and logical model, adequate information and knowledge of the general geology of a region is paramount. Advancements in technology "know-how" allow for the integration of seismic and borehole data to hypothetical gravity models. These advancements have enhanced visualization and improved interpretation of gravity hypothetical models.

The average bulk density of rocks and sediments is controlled by the density of minerals present, volume of pore spaces and the fluid content (Burger, 1992). A stratigraphic column of Harris County was created by Murray (1961) and Meyer (1939) for construction of gravity modelling (Table 2). This stratigraphic column was created by using well logs and borehole data from Harris County. The data shows that the Paleozoic

Ouachita basement rock was encountered at a depth of 10,000 meters (Table 2). Stratigraphic units were divided and classified into six layers consisting of five depositional rock ages and a Paleozoic Ouachita basement rock age. The Paleozoic basement rocks of the Ouachita Facies consist mainly of granitic igneous rocks with a thickness of 1,600 meters. An average density value of 2.95 g/cm^3 was assigned to these rocks. The Triassic age rock unit, which is comprised of mainly sandstone of the Eagle Mill Formation, has a thickness of 800 meters and an average density of 2.73 g/cm^3 . The Jurassic Salt unit (Louann Salt) is comprised of halite and has a thickness of 1,800 meters. An average density of 2.1 g/cm^3 was assigned to the salt unit. The Cretaceous age rock unit is comprised of limestone, shale and clay and has a thickness of 900 meters with an average density value of 2.7 g/cm^3 . The Tertiary age rock unit is comprised of sand, sandstone and shale and has a thickness of 4,500 meters, with an average density value of 2.67 g/cm^3 . The Quaternary age rock unit is comprised of clay and shale and has a thickness of 600 meters with an average density of 2.51 g/cm^3 (Murray, 1961).

Three cross-sections were created and used to generate a 2D hypothetical gravity model. The Bouguer anomaly map, magnetic and elevation grid files were used to construct the gravity model. The flight height (the height at which the magnetic data was collected) was considered and added to the elevation grid in the magnetic data column. Average rock densities defined by Murray (1961) in Table 2 and magnetic susceptibilities of the different rock layers were assigned. The average density value assigned to the Jurassic salt layer is 2.1 g/cm^3 with a magnetic susceptibility value of -0.0003 .

Systems - Main Formation	Description (Rock Type)	Depth (meters)	Estimated Thickness (meters)	Assigned Average Density (g/cm³)
Quaternary – Beaumont and Lissie	Mostly Clay, Shale and Sand Shale	0 - 600	600	2.51
Tertiary – Frio, Catahoula, Yegua, Jackson, Wilcox, Crockett-Carrizo	Mostly sand, sandstone (Frio & Yegua), sandy and silty shale, shale (Jackson)	600 - 5,100	4,500	2.67
Cretaceous – Eagle Ford, Woodbine	Limestone and Shale	5,100 - 6,000	900	2.7
Jurassic – Louann Salt	Rock Salt	6,000 - 7,800	1,800	2.1
Triassic – Eagle Mills	Sandstones, siltstone, shale	7,800 - 8,600	800	2.73
Paleozoic – Ouachita Facies (Basement rocks)	Granitic - Dioritic	8,600 - 10,000	1600	2.95

Table 2 – Main sedimentary units in Harris County with the depth, thickness and assigned average density (from Murray, 1961; Meyer, 1939). The densities of the six layers were used to build a 2D hypothetical gravity model.

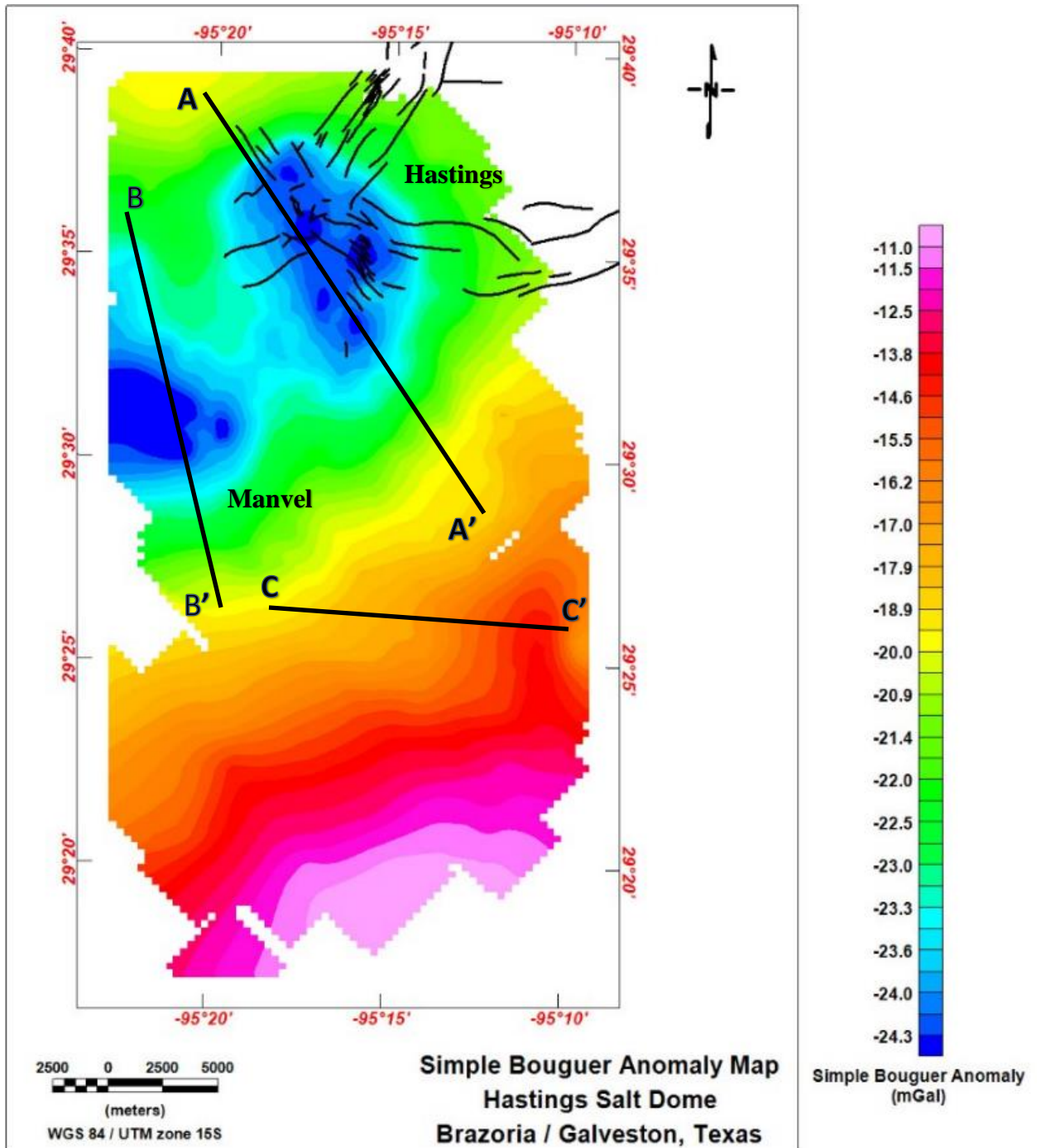


Figure 45 - Three cross sections A-A' (Hastings Salt Dome), B-B' (Manvel Salt Dome) and C-C' were drawn and used to create hypothetical gravity models. The fault shapefile that was extracted lies within Hastings Salt Dome. The faults are normal faults.

CROSS SECTION A-A'

The cross-section A-A' (Figure 45) runs in a northwest to southeast direction over the gravity low anomaly interpreted as Hastings Salt Dome (Figure 33). This cross-section is approximately 23 kilometers long and is projected to a depth of 10 kilometers. The gravity profile anomaly along cross section A-A' ranges from -18.99 mGal to -24.3 mGal, while the magnetic intensity anomaly ranges from -246.77 nT to -385.69 nT.

HYPOTHESIS

The 2D hypothetical gravity model along cross section A-A' shows that the Hastings Salt Dome is asymmetric in geometry (Figure 46). This can be supported by the distribution of the gravity low anomaly within it (Figure 35). This model also shows series of normal faults cutting across the Cretaceous and Tertiary layers. These normal faults were probably formed during the uprising of the Hastings Salt Dome due to the development of primarily extensional stresses in the overlying sedimentary rocks. The model shows that the Hastings Salt Dome occurs at a depth of approximately 3,790 meters, and it is categorized as a deep-seated salt dome (Figure 46). The depth of the Hastings Salt Dome as shown in the model is in agreement with the estimated depth derived from using the half-width equation. This model also shows that the Louann Salt layer of the Hastings Salt Dome has an average thickness of 3,680 meters (Figure 46). The tertiary and quaternary rock layers show a gulfward dipping to the southeast portion of the model. The vertical exaggeration of A-A' model is 0.89.

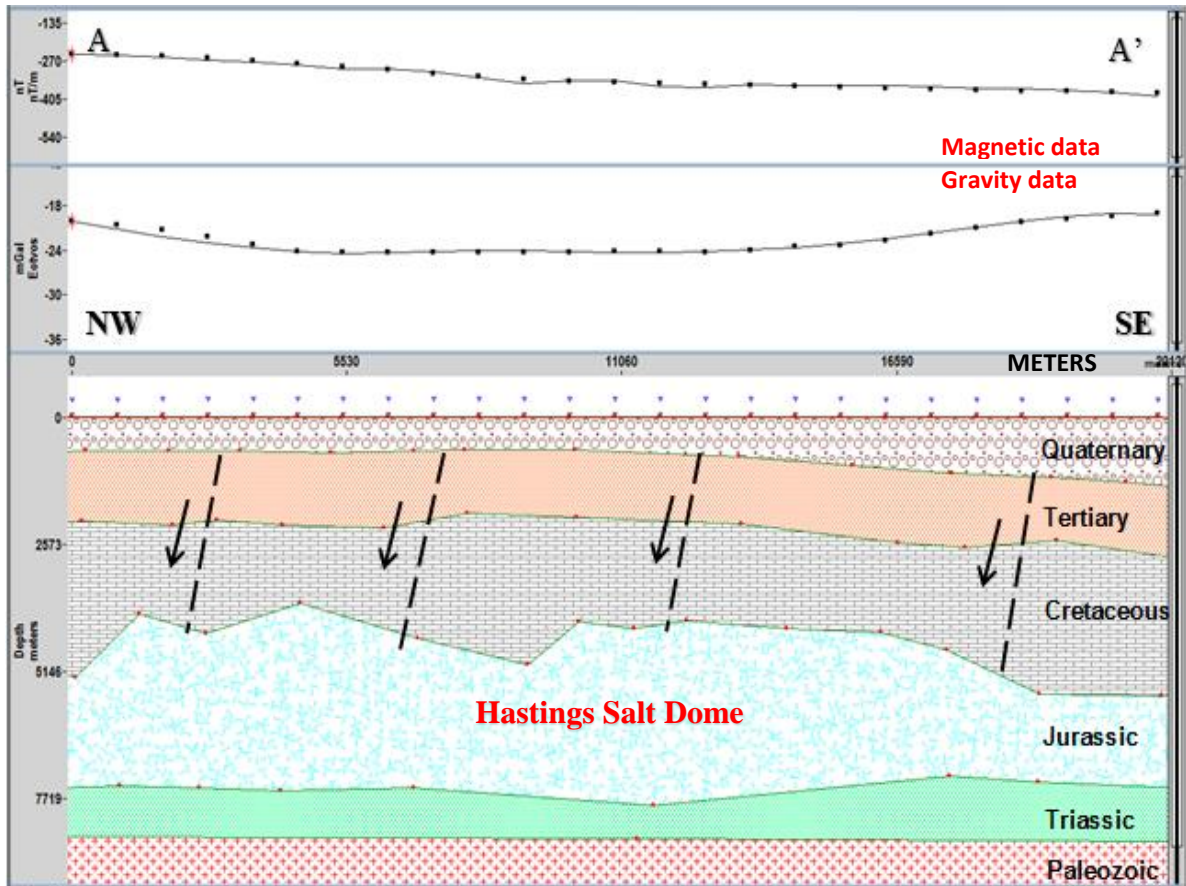


Figure 46 - A 2D hypothetical gravity model along cross section A-A' shows that the Hastings Salt Dome has an asymmetric geometry. The Hastings Salt Dome is bounded by a series of normal faults (in black broken lines) which cuts Cretaceous and Tertiary layers. Gulfward dipping of Quaternary and Tertiary layers in a southeast direction is observed. The Vertical Exaggeration = 0.89.

CROSS SECTION B-B'

Cross section B-B' (Figure 45) runs in a north to south direction over the gravity low anomaly interpreted as the Manvel Salt Dome (Figure 33). This cross section is approximately 17 kilometers long and is projected to a depth of 10 kilometers. The gravity profile anomaly along cross section B-B' ranges from -20.9 mGal to -24.6 mGal while the magnetic intensity anomaly ranges from -310.97 nT to -375.92 nT.

HYPOTHESIS

The 2D hypothetical gravity model along cross section B-B' shows that the Manvel Salt Dome is nearly symmetrical in geometry (Figure 47). The model also shows that the Manvel Salt is a diapiric salt dome where it is observed to have pierced into the overlying Cretaceous layer. The model shows that Manvel Salt Dome is a deep-seated salt dome based on depth of burial at a depth of approximately 4,290 meters. The model shows evidence of uplift of the overlying Tertiary and Quaternary layers over the Manvel Salt Dome (Figure 47).

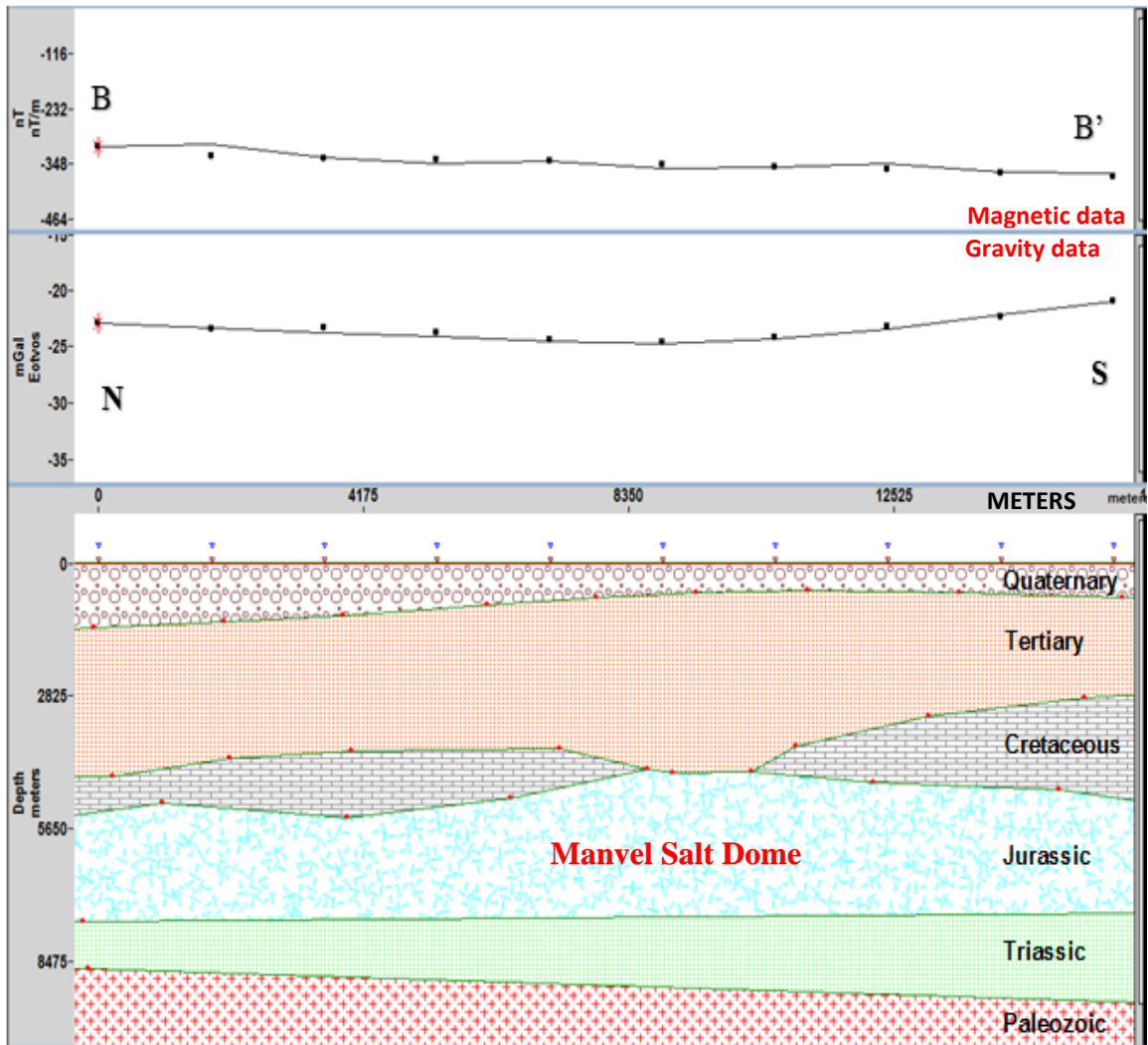


Figure 47 - A 2D hypothetical gravity model along cross-section B-B' shows that the Manvel Salt Dome has a near symmetric geometry. The Manvel Salt Dome is a diapiric type of salt structure and it is a deep-seated salt dome at a depth of 4,285 meters. The Vertical Exaggeration = 0.59.

CROSS- SECTION C-C'

Cross section C-C' (Figure 45) runs in a northwest to southeast direction over the gravity anomaly located to the south of the study area (Figure 33). The cross section is approximately 14 kilometers long and it projected to a depth of 10 kilometers. The gravity profile anomaly along cross section C-C' ranges from -14.16 mGal to -20.59 mGal while the magnetic intensity anomaly ranges from -380.54 nT to -414.37 nT.

HYPOTHESIS

The 2D hypothetical gravity model of cross section C-C' shows a salt withdrawal process in a westerly direction (Figure 48). As observed in the model, the salt withdrawal process results in a significant thinning of the Jurassic Louann Salt layer to the east. The gravity model shows gulfward thickening of the Cretaceous, Tertiary and Quaternary rock layers (Figure 48). It can be inferred from this model that the basin-ward progradation of sediment loading resulted in the salt withdrawing process due to differential loading. When this occurred, the salt layer in its solid-state flowed in a ductile manner. This observation could explain the process that led to the formation of Hastings and Manvel Salt Domes.

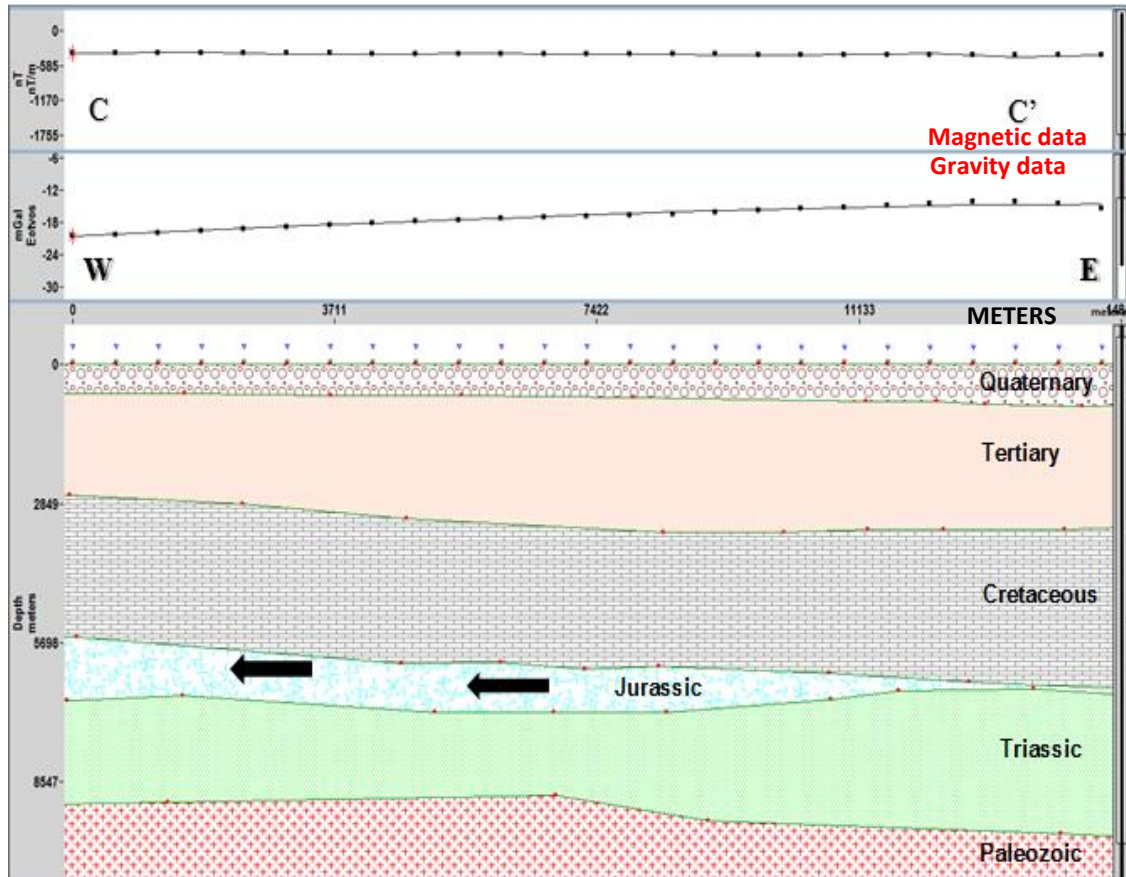


Figure 48 - A 2D hypothetical gravity model of cross section C-C' shows that the salt withdrawal process moved westward (represented by black arrows direction) and resulted in a significant thinning of the Jurassic salt layer. The overlying Cretaceous, Tertiary and Quaternary rock layers show thickening towards the east of the model. This observation supports the theory of sediment differential loading. The Vertical Exaggeration = 0.56.

DISCUSSION AND CONCLUSION

A total of 537 gravity readings were collected and used to create high resolution gravity anomaly maps. These relatively high resolution gravity anomaly maps revealed the geometry, shape, location and extent of the Hastings and Manvel Salt Domes. A Bouguer gravity anomaly map revealed lateral variations in subsurface rock density. The Bouguer gravity anomaly map showed that the Hastings and Manvel Salt Domes were represented by oval-shaped, gravity low anomalies with values ranging from -24.4 mGal to -23.8 mGal.

The georeferenced subsurface structural map of the Frio Sandstone in Hastings Oil Field shows that the Hastings Oil Field is located on the eastern flank of the Hastings Salt Dome in Brazoria County. The Mykawa Oil Field, on the other hand, is located to the northern portion and over the Hastings Salt Dome in Harris County (information from well logs). The relationship between the Hastings Oil Fields and the Hastings Salt Dome is now better defined and understood as a result of this study. The Manvel Salt Dome is located in the west portion of the study area and southwest of the Hastings Salt Dome. The depth of the Hastings Salt Dome was estimated at 3,915 meters by using the half-width equation method. The estimated depth applies to the center of the Hastings Salt Dome where the vertical gradient of gravity measured is greatest.

Well logs were correlated to create a cross section. The cross section was created to observe the effects of salt diapirism. Wells #1, #10 and #11 show uplift of the overlying sedimentary layers due to the uprising of the salt dome. Well #2 shows an uplifted Frio Shale unit but the Miocene Shale beds did not show an effect of uplift. In well #2, evidence of sediment compaction is observed, and this can explain a reason for subsidence within this region. A map of subsidence of Harris and Galveston Counties and its environ created by Zilkoski et al., (2003) shows a northward increase in the rate of subsidence. The subsidence observation sites (PAM 21 and PAM 33) also show that the rate of subsidence is greater in PAM 21 with an average subsidence rate of 0.3 cm per year.

The concept of creekology over the Bouguer anomaly gravity maps shows that the Dickinson Bayou wraps around the Manvel Salt Dome. This suggests that the region around the salt dome was uplifted due to the uprising of the Manvel Salt Dome. The Manvel Salt Dome has been interpreted as a deep-seated salt structure based on gravity model B-B. On the other hand, Clear Creek flowed across the Hastings Salt Dome and then towards the eastern portion of the Hastings Salt Dome it wrapped around it. The effect of the even distribution of gravity anomaly low could be due to the presence of faults. The Hastings Salt Dome is a deep-seated salt dome, and this is confirmed from the estimation using the half-width equation and the 2D hypothetical gravity model.

The 2D hypothetical gravity model and the Bouguer gravity maps show that Hastings Salt Dome is asymmetric in geometry, while Manvel Salt Dome is nearly symmetrical in geometry. In cross-section C-C', the 2D hypothetical gravity model

shows salt withdrawal which is likely due to the gulfward thickening of the overlying sediments towards the east. The isopach map of the Frio Shale shows maximum thickness towards the east of the cross section. The magnetic anomaly map shows a decrease in magnetic intensity to the east and southeast of the study area.

LIMITATIONS

The data collection phase of the field survey involved some unforeseen challenges that resulted in delays and required additional funding. The previous gravity dataset collected during the months of October through December 2015 was discarded. This was due to inconsistencies observed in the gravity dataset because of the faulty gravity meter. The data inaccuracies were identified during this study, and then the gravity meter was shipped to the company in Canada for repairs. These repairs lasted for three months before it was fixed and returned. Hence, a reliable gravity dataset was collected between May and August of 2016.

The classified land cover map shows that there is dense population of urban settlement to the north and a high concentration of agricultural fields, ranches and other privately owned properties towards the south and southwest. There were areas within the study area that were not accessible and were restricted to public access. This affected the distribution of gravity stations. An aero-gravity survey can be carried out within these restricted regions.

There were insufficient well logs especially over the Hastings Salt Dome to investigate for the uneven distribution of gravity low anomaly and to compare with the estimated depth calculated from using the half width equation method.

FUTURE WORK

The outcome of this study can serve as a reconnaissance survey for future work. Having identified the location of the Hastings Salt Dome as shown in the Bouguer anomaly map, a resistivity survey over the Hasting Salt Dome is recommended. Seismic data can be integrated with gravity and magnetic datasets to create a higher resolution gravity model. Recent advancements in technology allow for construction of 3D gravity models with the aid of 3D seismic data and well logs.

CITATIONS

- Arafin, S., 2014, Relative Bouguer anomaly: Sultan Qaboos University, Al-Khodh, Sultanate of Oman, The leading Edge.
- Amante, C. and B.W. Eakins, 2009. ETOPO1 1 Arc-Minute Global Relief Model: Procedures, Data Sources and Analysis. NOAA Technical Memorandum NESDIS NGDC-24. National Geophysical Data Center, NOAA. doi:10.7289/V5C8276M [September, 2016].
- Baker (Jr.), E.T., 1995, Stratigraphic nomenclature and geologic sections of the Gulf Coastal Plain of Texas: U.S. Geological Survey open file report 94-461.
- Bornhauser, M., 1958, Gulf Coast tectonics: American Association of Petroleum Geologists Bulletin, v. 42, p. 339-370.
- Braunstein, J., Huddleston, P., and Biel, R., 1988, COSUNA- Gulf Coast Regional Correlation Chart: American Association Petroleum Geologists, regional coordinator, I chart.
- Bruce, C.H., 1973, Pressured shale and related sedimentary deformation- Mechanism for development of regional contemporaneous faults: American Association of Petroleum Geologists Bulletin, v. 57, p. 878-886.
- Bushaw, D.J., 1968, Environmental synthesis of the East Texas Lower Cretaceous: Gulf Coast Association of Geological Societies Transactions, v. 18, p. 416-438.
- Burger, H. S., (1992), Exploration Geophysics of the shallow subsurface. Prentice Hall.
- Byerly, G.R., 1991, Igneous activity, *in* Salvador, A., editor, The Gulf of Mexico Basin: Boulder, Colorado, Geological Society of America, The Geology of North America, v. J., p. 91-108.
- Closs, E., 1968, Experimental analysis of Gulf Coast fractures patterns: AAPG Bulletin, v. 52, p.420-444.
- Coplin, L.S., and Galloway, Devin, 1999, Houston-Galveston, Texas – Managing coastal subsidence, in Galloway, Devin, Jones, D.R., and Ingebritsen, S.E., eds., Land subsidence in the United States: U.S. Geological Survey Circular 1182, p. 35-48.
- Denbury Resources Incorporation, 2011,
http://www.midwesterngovernors.org/EOR/Denbury_West_Hastings_Field_Unit_Handout.pdf

- Ewing, T. E., and R. F. Lopez, compilers, 1991, Principal structural features, Gulf of Mexico Basin, in A. Salvador, ed., The geology of North America, v. J: The Gulf of Mexico Basin: Geological Society of America, Boulder, Colorado, plate 2, scale 1:2,500,000.
- Frehner, B., 2004, From creekology to geology: Finding and conserving oil on the southern plains, 1859-1930 [Ph.D.]: University of Oklahoma.
- Foote, R.Q., Massingill, L.M., and Wells, R.H., 1988, Petroleum geology and the distribution of conventional crude oil natural gas, and natural gas liquids, East Texas basin: Department of the Interior, U.S. Geological Survey, Open-File Report 88-450k.
- Gabrysch, R.K., and Bonnet, C.W., 1975, Land-surface subsidence in the Houston-Galveston regions, Texas: Texas Water Development Board Report 188, 19p.
- Galloway, Devin, Jones, D.R., and Ingebritsen, S.E., eds., 1999, Land subsidence in the United States: U.S. Geological Survey Circular 1182, 177p.
- Galloway, W.H., 1982, Frio Formation of the Texas Gulf Coast Basin. Austin: Bureau of Economic Geology, University of Texas.
- Galloway, W. E., 2005, Gulf of Mexico basin depositional record of Cenozoic North American drainage basin evolution: Special Publication of the International Association of Sedimentologists No. 35, p. 409-423.
- Grubb, H.F., 1998, Summary of hydrology of the regional aquifer systems, Gulf Coastal plain, South-Central United States- Regional aquifer systems analysis-Gulf Coastal Plain: U.S. Geological Survey Professional paper 1416-A, p.61 p.
- Halbouty, M., 1976, Salt Domes, Gulf Region, United States and Mexico. Texas: Gulf Publishing Company.
- Harris – Galveston Subsidence District: <http://hgsubsidence.org/subsidence-data/> (accessed September, 2016).
- Holzer, T.L., Bluntzer, R.L., 1984, Land subsidence near oil and gas fields, Houston, Texas. Ground Water 22:450-459.
- Hosman, R.L. and Weiss, J.S., 1991, Geohydrologic units of the Mississippi Embayment and Texas Coastal Uplands Aquifer Systems, South-Central United States – Regional aquifer system analysis-Gulf Coastal Plain: U.S. Geological Survey Professional Paper 1416-B, 19 p.
- Hudec, M.R., Norton, I.O., Jackson, M.P.A., Peel, F.J., 2013, Jurassic evolution of the Gulf of Mexico Salt Basin: AAPG Bulletin, volume 97, 10, p 1683-1710.

- Humphris, C. C., Jr., 1979, Salt movement on continental slope, northern Gulf of Mexico: AAPG Bulletin, v. 63, p. 782–798.
- Internationale Gravimetric Bureau, B.G.I., Reference Gravity Stations,
<http://bgi.gov/>[August, 2016].
- Jackson, M.P.A., and Galloway, W.E., 1984, Structural and depositional styles of Gulf Coast Tertiary continental margins-Applications to hydrocarbon exploration: Continuing Education Course Notes Number 25, American Association of Petroleum Geologists, p. 255.
- Jackson, M.P.A., and Talbot, C.J., 1986. External shapes, strain rates, and dynamics of salt structures: Geological Society of American Bulletin, volume 97, p 305-323.
- Khan, S.D., Huang, Z. and Karacay, A. Nat Hazards (2014) 73: Study of ground subsidence in northwest Harris county using GPS, LiDAR and InSAR techniques, 1143. doi:10.1007/s11069-014-1067-x.
- Lawless, P.N., R.H. Fillon, and R.G. Lytton, III, 1997, Gulf of Mexico Cenozoic biostratigraphic, lithostratigraphic, and sequence stratigraphic event chronology: Gulf Coast Association of Geological Societies Transactions, v. 47, p. 271-282.
- Lopez, J. A., 1995, Salt tectonism of the U.S. Gulf Coast Basin: Map published by the New Orleans Geological Society, Louisiana.
- Martin, R. G., 1980, Distribution of salt structures in Gulf of Mexico region: Map and descriptive text: U.S. Geological Survey Miscellaneous Field Study Map MF-1213, 8 p., 2 sheets.
- Martinez, J.D., 1991, Salt Domes. American Scientist, vol 79, no. 5, p 420-431 [retrieved from <http://www.jstor.org/stable/29774476>].
- Meyer, W. G., 1939, Stratigraphy and Historical Geology of Gulf Coastal Plain in Vicinity of Harris County, Texas. Bulletin of the American Association of Petroleum Geologists, pp. 145-211.
- Murray, G., 1961, Geology of the Atlantic and Gulf Coastal Province of North America. New York: Harper and Brothers.
- National Weather Service: National Oceanic and Atmospheric Administration
<http://www.weather.gov/images/hgx/climate/KHOU2016plot.png> [accessed October, 2016].

- Newkirk, T.F., 1971, Possible future petroleum potential of Jurassic, western Gulf Basin, in Cram, I.H. (ed.), Future petroleum provinces of the United State-their geology and potential: American Association of Petroleum Geologists Memoir 15, p. 927-953.
- Nichols, P.H., 1964, The remaining frontiers for exploration in northeast Texas: Gulf Coast Association of Geological Societies Transactions, v. 14, p. 7-22.
- O'Brien, G.D., 1968, Survey of diapirs and diapirism in Braunstein, Jules, and O'Brien, G.D., eds., Diapirism and diapirs: American Association of Petroleum Geologists Memoir 8, p.1-9.
- PACES, 2016, Gravity and Magnetic Database, Pan American Center for Earth and Environmental Studies, research.utep.edu/paces. [Retrieved September, 2016].
- Parker, T.J., and A. N. McDowell, 1955, Scale models as guide to interpretation of salt dome faulting: American Association of Petroleum Geologists Bulletin, v. 35, p. 2076-2086.
- Pigott, J.D., and Bradley, B.W., 2014, Application of production decline curve analysis to clastic reservoir facies characterization within a sequence stratigraphic framework: Example – Frio Formation, south Texas: GCAGS Journal, vol. 3, p. 111-134.
- Presley, M.W., and Reed, C.H., 1984, Jurassic Exploration Trends of East Texas in Presley, M.W. (ed.). The Jurassic of East Texas: East Texas Geological Society and East Texas Jurassic Exploration Conference, Tyler, Texas, March 27-28, 1984, P. 11-21.
- Rainwater, E.H., 1967, Resume of Jurassic to recent sedimentation history of the Gulf of Mexico basin: Gulf Coast Association of Geological Societies Transaction, v.16, p. 179-210.
- Salvador, A., 1991, Origin and development of the Gulf of Mexico basin, in A. Salvador, ed., The Gulf of Mexico Basin: Geological Society of America, The Geology of North America, v.J, P. 389-444.
- Schultz-Ela, D.D., Jackson, M.P.A, Vendeville, B.C, 1993, Mechanics of active salt diapirism; Bureau of Economic Geology, Tectonophysics, vol. 228, p. 275-312.
- Scintrex, 2012, www.scintrexltd.com [Retrieved August, 2016].
- Seigel, H.O., 1995, A guide to high precision land gravimeter surveys, Scintrex Limited, Concord, Ontario.

- Solis, R.F., 1981, Upper Tertiary and Quaternary depositional systems, central Coastal Plain, Texas-Regional geology of the coastal aquifer and potential liquid-waste repositories: The University of Texas at Austin, Bureau of Economic Geology Report of Investigations 108, 89 p.
- Telford, W.M., Geldart, L.P., and Sheriff, R.E., Applied Geophysics, Second Edition: Cambridge, Cambridge University Press, 1990.
- Texas Railroad Commission, 2012; RRC Public GIS Map Viewer, www.rrc.state.tx.us/ [Retrieved August, 2016].
- Thomas, W.A., 1953, Hastings Field, Brazoria and Galveston Counties, Texas *in* Houston Geological Society, 2007 – Guidebook, Field Trip Routes, Oil Fields, p. 121-124.
- Trimble Inc., 2011, NOMAD 9000 Series Users Guide: www.Trimble.com [Accessed October 2016].
- U.S. Department of the Interior, U.S. Geological Survey:
 url:http://pubs.usgs.gov/ds/2006/232/data/GRAVITY%20DATA/GRAV_INFO.TXT
- Walper, J.L., and Miller, R.E., 1985, Tectonic evolution of Gulf Coast basins in Perkins, B.F., and Martin, G.B., Habitat of oil and gas in the Gulf Coast: Proceedings of the Fourth Annual Research Conference, Gulf Coast Section, Society of Economic Paleontologists and Mineralogists Foundation, p. 25-42.
- Warren, J.K., 2006, Evaporites: Sediments, resources, and hydrocarbons: Berlin, Springer, p. 1035.
- Withjack, M.O., and Scheiner, C., 1982, Fault patterns associated with domes, An experimental and analytical study: AAPG Bulletin vol. 66, no. 3, p. 302-316.
- Worrall, D. M., and S. Snelson, 1989, Evolution of the northern Gulf of Mexico, with emphasis on Cenozoic growth faulting and the role of salt, in A. W. Bally and A. R. Palmer, eds., The Geology of North America—an overview: Boulder, Colorado, Geological Society of America, v. A, p. 97–138.
- Williamson, A.K. and Grubb, H.F., 2001, Groundwater flow in the Gulf Coast aquifer systems, Regional aquifer system analysis – Gulf coastal plain, U.S. Geological Survey Professional Paper 1416-F, p. 173.
- Zheng, Y. Huang., Shuhab, K., Robert, S., and Ramesh, S., 2011, Investigating Salt domes in Harris county, Texas, using GIS and Remote Sensing Techniques: The Gulf coast association of Geological societies.

Zilkoski, D.B., Hall, C.W., Mitchell, J.G., Kammula, V., Singh, A., Chrismer, W.M., and Neighbors, R.J., 2003, The Harris – Galveston Coastal Subsidence District / National Geodetic Survey automated global positioning system monitoring project, Frieswood, Texas.

APPENDIX A – GRAVITY DATASET FOR STUDY AREA

Latitude	Longitude	Observed Gravity_G _{obs} (mGal)	Elevation_(m)	Free Air Anomaly (mGal)	Theoretical Gravity_Gn (mGal)	Simple Bouguer Anomaly (mGal)	Residual Gravity Anomaly (mGal)
29.4278889	-95.2440567	979265.865	12.928	-10.535	979280.390	-17.078	-14.525
29.4353046	-95.2444458	979266.19	12.093	-11.041	979280.963	-17.161	-14.773
29.4411392	-95.244194	979266.544	11.503	-11.320	979281.414	-17.142	-14.870
29.4461937	-95.2393341	979266.686	11.008	-11.722	979281.805	-17.293	-15.119
29.4520283	-95.235054	979266.982	10.647	-11.988	979282.256	-17.377	-15.274
29.4610558	-95.2290802	979267.104	10.813	-12.513	979282.954	-17.986	-15.850
29.4646664	-95.22686	979266.881	10.91	-12.986	979283.233	-18.507	-16.352
29.4722214	-95.22789	979267.124	10.811	-13.358	979283.818	-18.829	-16.694
29.4769726	-95.2199173	979267.417	10.604	-13.496	979284.185	-18.862	-16.768
29.4850273	-95.2156143	979267.75	9.745	-14.051	979284.809	-18.983	-17.059
29.4937782	-95.2065582	979268.334	9.653	-14.173	979285.486	-19.058	-17.152
29.5053062	-95.1923904	979269.875	7.282	-14.256	979286.378	-17.941	-16.503
29.5096664	-95.1873322	979270.141	7.276	-14.329	979286.716	-18.012	-16.575
29.5206108	-95.1891937	979270.582	7.53	-14.657	979287.563	-18.468	-16.981
29.5231953	-95.1930313	979270.441	8.309	-14.758	979287.763	-18.963	-17.322
29.5261669	-95.1963882	979270.33	8.285	-15.107	979287.993	-19.300	-17.663
29.5294724	-95.2013855	979270.234	8.655	-15.345	979288.249	-19.725	-18.015
29.5318604	-95.2036133	979270.246	8.547	-15.551	979288.434	-19.876	-18.188
29.5371666	-95.2111359	979270.088	9.151	-15.933	979288.845	-20.565	-18.757
29.5291672	-95.2163086	979269.541	9.044	-15.894	979288.226	-20.471	-18.685
29.5282497	-95.2145309	979269.485	8.919	-15.917	979288.155	-20.431	-18.670
29.5253334	-95.2165298	979269.325	8.685	-15.924	979287.929	-20.319	-18.604
29.5156384	-95.2256927	979268.267	9.612	-15.945	979287.178	-20.809	-18.911
29.5118065	-95.2293854	979268.517	9.456	-15.446	979286.881	-20.232	-18.364
29.5097771	-95.2336655	979267.93	10.601	-15.523	979286.724	-20.888	-18.794
29.5147495	-95.2381668	979267.94	10.366	-15.970	979287.109	-21.216	-19.169
29.5019436	-95.2401352	979267.612	11.375	-14.996	979286.118	-20.752	-18.506
29.4968891	-95.245224	979267.224	11.21	-15.043	979285.727	-20.716	-18.503
29.5186939	-95.2247238	979268.434	10.326	-15.794	979287.415	-21.020	-18.981
29.5254993	-95.2204437	979269.055	9.381	-15.992	979287.942	-20.739	-18.887
29.5293617	-95.2256088	979268.89	10.582	-16.085	979288.241	-21.441	-19.351
29.5350552	-95.2325821	979268.751	11.528	-16.373	979288.682	-22.208	-19.931
29.5308895	-95.2391968	979268.005	11.687	-16.748	979288.359	-22.662	-20.354

Latitude	Longitude	Observed Gravity_G _{obs} (mGal)	Elevation_(m)	Free Air Anomaly (mGal)	Theoretical Gravity_Gn (mGal)	Simple Bouguer Anomaly (mGal)	Residual Gravity Anomaly (mGal)
29.5289993	-95.2473602	979267.617	12.057	-16.875	979288.213	-22.977	-20.596
29.5356941	-95.244278	979268.058	13.082	-16.636	979288.731	-23.257	-20.673
29.5413055	-95.2383041	979268.705	12.674	-16.550	979289.166	-22.964	-20.461
29.5448608	-95.2351379	979269.048	11.988	-16.694	979289.442	-22.761	-20.394
29.5458336	-95.2293854	979269.554	10.293	-16.787	979289.517	-21.996	-19.963
29.5443058	-95.2274475	979269.534	10.586	-16.598	979289.399	-21.955	-19.865
29.542305	-95.2306137	979269.383	10.956	-16.480	979289.244	-22.024	-19.861
29.5391941	-95.2265854	979269.422	11.231	-16.115	979289.003	-21.799	-19.581
29.5397778	-95.2197495	979269.829	9.937	-16.152	979289.048	-21.181	-19.219
29.536972	-95.2204437	979269.746	9.302	-16.214	979288.830	-20.921	-19.084
29.5383606	-95.2134476	979270.068	9.148	-16.047	979288.938	-20.677	-18.870
29.5347214	-95.2193604	979269.701	9.978	-15.876	979288.656	-20.926	-18.955
29.5311661	-95.2161942	979269.609	9.516	-15.835	979288.381	-20.651	-18.772
29.5266953	-95.2153625	979269.483	9.318	-15.676	979288.034	-20.392	-18.551
29.520834	-95.2125549	979269.438	8.384	-15.555	979287.580	-19.798	-18.142
29.5161114	-95.220192	979268.795	8.94	-15.661	979287.215	-20.185	-18.420
29.513361	-95.209137	979269.147	8.315	-15.289	979287.002	-19.497	-17.855
29.5079994	-95.2098312	979269.053	8.807	-14.816	979286.587	-19.273	-17.534
29.5010834	-95.2118912	979268.725	8.269	-14.774	979286.051	-18.959	-17.326
29.4999447	-95.213028	979268.631	8.805	-14.615	979285.963	-19.071	-17.332
29.499527	-95.2191391	979268.251	9.114	-14.867	979285.931	-19.480	-17.680
29.5056953	-95.1991119	979269.739	7.25	-14.432	979286.408	-18.101	-16.669
29.501833	-95.1994705	979269.216	7.528	-14.570	979286.109	-18.380	-16.893
29.4913063	-95.2107468	979268.072	9.55	-14.275	979285.295	-19.109	-17.223
29.4790287	-95.2199173	979267.413	11.062	-13.518	979284.344	-19.116	-16.931
29.4686661	-95.2246399	979266.987	10.881	-13.198	979283.543	-18.705	-16.556
29.4576664	-95.2323074	979266.91	10.854	-12.432	979282.692	-17.925	-15.782
29.4314175	-95.2434692	979266.041	12.459	-10.777	979280.662	-17.082	-14.621
29.4281673	-95.2426147	979265.862	12.683	-10.635	979280.411	-17.054	-14.549
29.4260006	-95.1592789	979265.752	12.854	-10.525	979280.244	-17.030	-14.492
29.5453606	-95.310112	979268.849	15.247	-15.926	979289.480	-23.642	-20.631
29.5463333	-95.3141937	979269.055	15.032	-15.862	979289.556	-23.469	-20.501
29.5432224	-95.314415	979268.84	15.073	-15.823	979289.315	-23.451	-20.475
29.5398617	-95.311554	979268.537	15.223	-15.819	979289.054	-23.524	-20.517
29.536417	-95.3075867	979268.298	14.767	-15.932	979288.787	-23.406	-20.489
29.5359993	-95.31353	979268.269	15.128	-15.818	979288.755	-23.474	-20.486

Latitude	Longitude	Observed Gravity_G _{obs} (mGal)	Elevation_(m)	Free Air Anomaly (mGal)	Theoretical Gravity_Gn (mGal)	Simple Bouguer Anomaly (mGal)	Residual Gravity Anomaly (mGal)
29.5329723	-95.3186646	979268.045	15.693	-15.633	979288.521	-23.575	-20.476
29.5303898	-95.3141403	979267.806	14.777	-15.954	979288.321	-23.433	-20.515
29.5309715	-95.3104172	979267.983	14.743	-15.833	979288.366	-23.294	-20.383
29.5310841	-95.3037186	979267.967	14.997	-15.779	979288.374	-23.369	-20.407
29.5320835	-95.2971649	979267.947	14.46	-16.042	979288.452	-23.360	-20.505
29.5362778	-95.2971115	979268.243	14.481	-16.065	979288.777	-23.393	-20.534
29.5408611	-95.3009186	979268.409	14.843	-16.142	979289.132	-23.654	-20.723
29.5441113	-95.2978363	979268.717	14.476	-16.199	979289.384	-23.525	-20.667
29.545084	-95.294136	979268.67	14.509	-16.311	979289.459	-23.654	-20.789
29.5428333	-95.2896118	979268.502	13.909	-16.490	979289.285	-23.529	-20.783
29.5392227	-95.289444	979268.165	14.221	-16.451	979289.005	-23.648	-20.840
29.5340557	-95.2893906	979267.942	13.925	-16.365	979288.605	-23.412	-20.663
29.528944	-95.2892532	979267.721	13.661	-16.272	979288.209	-23.185	-20.488
29.5240269	-95.2888336	979267.366	13.85	-16.188	979287.828	-23.197	-20.462
29.5193062	-95.2888031	979267.086	13.396	-16.242	979287.462	-23.022	-20.376
29.5158882	-95.2887802	979266.873	13.262	-16.232	979287.197	-22.944	-20.324
29.5092506	-95.2886963	979266.465	13.209	-16.142	979286.684	-22.827	-20.219
29.5044441	-95.2888031	979266.523	12.562	-15.912	979286.311	-22.269	-19.788
29.5013046	-95.288475	979266.471	12.408	-15.768	979286.068	-22.048	-19.597
29.5018063	-95.2926102	979266.35	13.233	-15.674	979286.107	-22.371	-19.757
29.5017509	-95.2985535	979266.372	13.533	-15.555	979286.103	-22.404	-19.731
29.4986115	-95.2884979	979266.226	12.562	-15.757	979285.860	-22.115	-19.634
29.4920826	-95.288559	979266.095	12.906	-15.277	979285.355	-21.808	-19.260
29.4858055	-95.2887192	979266.146	12.73	-14.794	979284.869	-21.237	-18.723
29.4803333	-95.2911911	979265.856	13.783	-14.336	979284.445	-21.311	-18.589
29.4755287	-95.293335	979265.597	13.489	-14.314	979284.074	-21.141	-18.477
29.4779453	-95.301445	979265.308	13.851	-14.678	979284.261	-21.688	-18.953
29.4829731	-95.3078918	979265.248	14.512	-14.923	979284.650	-22.268	-19.402
29.4858055	-95.3116379	979265.207	15.023	-15.026	979284.869	-22.629	-19.662
29.4895287	-95.3166351	979265.163	14.955	-15.379	979285.157	-22.947	-19.994
29.4930553	-95.3213348	979265.156	15.683	-15.434	979285.430	-23.371	-20.274
29.4768333	-95.3056412	979265.143	14.311	-14.615	979284.175	-21.858	-19.032
29.4738884	-95.3118057	979264.887	15.113	-14.396	979283.947	-22.044	-19.060
29.4668064	-95.3031082	979264.923	13.969	-14.165	979283.399	-21.235	-18.476
29.4611664	-95.3085022	979264.785	14.058	-13.839	979282.963	-20.954	-18.178
29.4576111	-95.3119736	979264.303	15.14	-13.712	979282.688	-21.375	-18.385

Latitude	Longitude	Observed Gravity_G _{obs} (mGal)	Elevation_(m)	Free Air Anomaly (mGal)	Theoretical Gravity_Gn (mGal)	Simple Bouguer Anomaly (mGal)	Residual Gravity Anomaly (mGal)
29.4537506	-95.3156128	979264.106	14.733	-13.737	979282.389	-21.193	-18.283
29.451334	-95.3100815	979264.272	14.637	-13.413	979282.202	-20.821	-17.930
29.449028	-95.3032227	979264.528	14.905	-12.896	979282.024	-20.439	-17.496
29.4476395	-95.2971954	979264.792	14.411	-12.677	979281.917	-19.971	-17.125
29.4526672	-95.2958069	979264.854	14.498	-12.977	979282.305	-20.314	-17.451
29.4561672	-95.2993088	979264.62	15.039	-13.315	979282.576	-20.926	-17.956
29.4611111	-95.299614	979265.008	13.97	-13.639	979282.958	-20.709	-17.950
29.4596939	-95.3044739	979264.684	14.583	-13.664	979282.849	-21.045	-18.165
29.4531384	-95.2958603	979264.817	14.505	-13.049	979282.342	-20.389	-17.525
29.4529171	-95.2916412	979265.029	14.173	-12.922	979282.325	-20.095	-17.296
29.4568882	-95.2877808	979265.088	14.491	-13.072	979282.632	-20.406	-17.544
29.4568329	-95.2833862	979265.193	14.367	-13.001	979282.627	-20.272	-17.434
29.4614162	-95.2878647	979265.271	14.328	-13.289	979282.982	-20.541	-17.711
29.4663048	-95.2944412	979265.17	14.945	-13.578	979283.360	-21.142	-18.190
29.4690285	-95.2981415	979265.057	14.896	-13.917	979283.571	-21.456	-18.514
29.4677505	-95.287941	979265.485	14.198	-13.605	979283.472	-20.791	-17.987
29.471138	-95.2846909	979265.804	13.294	-13.827	979283.734	-20.555	-17.930
29.4727783	-95.2783051	979266.016	12.317	-14.044	979283.861	-20.277	-17.845
29.4689159	-95.2753067	979266.052	12.132	-13.766	979283.562	-19.906	-17.510
29.4609165	-95.2743301	979265.737	13.376	-13.078	979282.943	-19.848	-17.206
29.4558887	-95.2693634	979266.2	12.385	-12.532	979282.554	-18.800	-16.354
29.4546947	-95.263031	979266.52	12.021	-12.232	979282.462	-18.316	-15.942
29.4463615	-95.2641678	979266.196	12.317	-11.821	979281.818	-18.054	-15.622
29.4453335	-95.2686386	979266.107	13.251	-11.542	979281.738	-18.248	-15.631
29.4401112	-95.2616425	979266.003	12.782	-11.387	979281.335	-17.856	-15.332
29.4372768	-95.25811	979266.077	12.251	-11.258	979281.115	-17.458	-15.038
29.4383602	-95.2510834	979266.256	11.986	-11.244	979281.199	-17.310	-14.943
29.4382782	-95.2538605	979266.124	12.406	-11.240	979281.193	-17.519	-15.069
29.4326954	-95.2516403	979265.846	12.524	-11.050	979280.761	-17.389	-14.915
29.432972	-95.2467194	979266.025	11.951	-11.070	979280.783	-17.118	-14.758
29.438139	-95.2468033	979266.26	11.844	-11.267	979281.182	-17.261	-14.922
29.4300556	-95.2458649	979265.97	12.193	-10.824	979280.557	-16.995	-14.587
29.4287777	-95.237442	979265.938	12.703	-10.600	979280.458	-17.029	-14.520
29.4324722	-95.2530823	979265.855	12.597	-11.002	979280.744	-17.377	-14.889
29.4374714	-95.2684708	979265.851	13.022	-11.261	979281.130	-17.851	-15.279
29.4415836	-95.2801361	979265.438	13.146	-11.954	979281.448	-18.607	-16.010

Latitude	Longitude	Observed Gravity_G _{obs} (mGal)	Elevation_(m)	Free Air Anomaly (mGal)	Theoretical Gravity_Gn (mGal)	Simple Bouguer Anomaly (mGal)	Residual Gravity Anomaly (mGal)
29.4482231	-95.2801971	979265.292	13.948	-12.365	979281.962	-19.424	-16.670
29.454916	-95.2792511	979265.534	14.014	-12.621	979282.479	-19.713	-16.945
29.472723	-95.2718048	979265.982	11.479	-14.332	979283.857	-20.142	-17.875
29.4722214	-95.2637787	979266.157	11.847	-14.005	979283.818	-20.000	-17.661
29.4759159	-95.2630539	979266.277	11.909	-14.151	979284.104	-20.178	-17.827
29.4799442	-95.2613602	979266.305	11.83	-14.460	979284.415	-20.447	-18.110
29.4800549	-95.2518921	979266.49	11.869	-14.271	979284.424	-20.278	-17.934
29.4763603	-95.2494965	979266.618	11.324	-14.025	979284.138	-19.756	-17.520
29.4744453	-95.2496109	979266.595	11.486	-13.850	979283.990	-19.663	-17.395
29.4839439	-95.2509995	979266.527	11.688	-14.591	979284.725	-20.506	-18.198
29.4859715	-95.2568893	979266.354	12.321	-14.725	979284.882	-20.961	-18.528
29.4859715	-95.2627487	979266.292	11.785	-14.953	979284.882	-20.917	-18.590
29.5001392	-95.2667465	979266.286	12.557	-15.817	979285.978	-22.172	-19.692
29.5450287	-95.2873917	979268.63	14.273	-16.420	979289.455	-23.643	-20.825
29.5463886	-95.28022	979268.48	13.803	-16.820	979289.560	-23.806	-21.080
29.5465565	-95.2745285	979268.37	14.26	-16.802	979289.573	-24.019	-21.203
29.5467777	-95.2677231	979268.215	14.442	-16.918	979289.590	-24.227	-21.375
29.5443611	-95.2634964	979268.239	13.159	-17.103	979289.403	-23.763	-21.164
29.5431118	-95.2672195	979268.009	13.776	-17.046	979289.306	-24.018	-21.297
29.5487499	-95.2590866	979268.446	13.924	-17.000	979289.743	-24.047	-21.297
29.5513058	-95.2528305	979268.791	12.904	-17.168	979289.941	-23.698	-21.150
29.5480556	-95.2446671	979269	12.285	-16.898	979289.689	-23.115	-20.689
29.5499725	-95.2288055	979269.878	10.729	-16.649	979289.838	-22.078	-19.960
29.5550842	-95.2224197	979270.294	10.14	-16.811	979290.234	-21.942	-19.940
29.5317783	-95.2494736	979267.726	12.895	-16.723	979288.428	-23.249	-20.702
29.53475	-95.2585526	979267.764	11.887	-17.226	979288.658	-23.242	-20.894
29.5390835	-95.2631378	979267.795	13.943	-16.896	979288.994	-23.953	-21.199
29.5418053	-95.2710266	979268.056	13.33	-17.035	979289.205	-23.781	-21.149
29.5376663	-95.2678604	979267.796	13.738	-16.849	979288.884	-23.801	-21.088
29.5316658	-95.2806091	979267.511	12.535	-17.040	979288.419	-23.384	-20.908
29.5265274	-95.2806091	979267.216	13.563	-16.620	979288.021	-23.484	-20.805
29.5191669	-95.2831421	979267.01	13.073	-16.407	979287.451	-23.023	-20.441
29.5165272	-95.291748	979266.949	13.369	-16.172	979287.247	-22.938	-20.298
29.5233326	-95.2971649	979267.516	14.13	-15.897	979287.774	-23.048	-20.258
29.5244713	-95.3083344	979267.467	14.781	-15.834	979287.862	-23.314	-20.395
29.5283051	-95.3082504	979267.683	14.765	-15.920	979288.159	-23.392	-20.476

Latitude	Longitude	Observed Gravity_G _{obs} (mGal)	Elevation_(m)	Free Air Anomaly (mGal)	Theoretical Gravity_Gn (mGal)	Simple Bouguer Anomaly (mGal)	Residual Gravity Anomaly (mGal)
29.5161381	-95.3104172	979266.825	14.855	-15.808	979287.217	-23.325	-20.392
29.5221672	-95.3136978	979267.285	14.912	-15.797	979287.684	-23.344	-20.399
29.5286388	-95.3139725	979267.608	15.246	-15.872	979288.185	-23.588	-20.577
29.5447769	-95.3257751	979269.199	15.221	-15.539	979289.435	-23.242	-20.236
29.5451393	-95.3304138	979269.315	15.204	-15.456	979289.463	-23.151	-20.148
29.5496941	-95.3298874	979269.594	15.495	-15.440	979289.816	-23.282	-20.222
29.5387783	-95.330719	979268.601	15.522	-15.579	979288.970	-23.435	-20.369
29.5351944	-95.3309708	979268.298	16.121	-15.420	979288.693	-23.578	-20.395
29.5290279	-95.330719	979267.663	16.014	-15.610	979288.215	-23.715	-20.552
29.5220833	-95.3304443	979266.857	16.458	-15.741	979287.677	-24.070	-20.820
29.5141659	-95.3303299	979266.012	17.07	-15.784	979287.064	-24.423	-21.052
29.5086937	-95.3302536	979265.605	17.399	-15.666	979286.640	-24.471	-21.035
29.5024166	-95.329277	979265.489	16.266	-15.646	979286.154	-23.878	-20.665
29.4973888	-95.3271103	979265.259	16.28	-15.482	979285.765	-23.721	-20.506
29.4941387	-95.3227463	979265.209	16.196	-15.307	979285.514	-23.503	-20.305
29.5094166	-95.3331146	979265.794	16.493	-15.813	979286.696	-24.160	-20.902
29.5038891	-95.3387222	979265.386	16.095	-15.916	979286.268	-24.061	-20.882
29.497694	-95.3442535	979264.918	16.623	-15.741	979285.789	-24.154	-20.871
29.4912491	-95.3503342	979264.656	15.73	-15.780	979285.290	-23.741	-20.634
29.4915562	-95.3504181	979264.724	15.73	-15.736	979285.314	-23.696	-20.590
29.4623051	-95.3410568	979264.047	14.947	-14.391	979283.051	-21.956	-19.004
29.4673061	-95.3398056	979263.91	15.37	-14.784	979283.438	-22.563	-19.528
29.4715004	-95.3360291	979264.036	15.377	-14.981	979283.762	-22.763	-19.726
29.4763889	-95.3314133	979264.35	15.817	-14.909	979284.140	-22.914	-19.790
29.4575272	-95.3281937	979264.337	14.711	-13.804	979282.681	-21.249	-18.344
29.458889	-95.3231125	979264.17	15.108	-13.954	979282.787	-21.600	-18.617
29.4648609	-95.3172531	979264.275	15.539	-14.178	979283.248	-22.042	-18.973
29.4644718	-95.328476	979263.901	15.278	-14.603	979283.218	-22.334	-19.317
29.4694996	-95.3284454	979264.314	14.846	-14.712	979283.607	-22.225	-19.293
29.4848328	-95.3005295	979265.518	14.056	-14.938	979284.794	-22.051	-19.276
29.4420834	-95.302475	979264.45	14.429	-12.584	979281.487	-19.887	-17.037
29.4375553	-95.3000031	979264.532	13.782	-12.352	979281.137	-19.327	-16.605
29.4197216	-95.2681427	979265.123	13.192	-10.565	979279.759	-17.241	-14.636
29.4183884	-95.2553635	979265.135	13.045	-10.495	979279.656	-17.097	-14.521
29.4200287	-95.2323303	979265.539	12.902	-10.262	979279.782	-16.791	-14.243
29.4301395	-95.214386	979266.835	10.531	-10.479	979280.564	-15.808	-13.729

Latitude	Longitude	Observed Gravity_G _{obs} (mGal)	Elevation_(m)	Free Air Anomaly (mGal)	Theoretical Gravity_Gn (mGal)	Simple Bouguer Anomaly (mGal)	Residual Gravity Anomaly (mGal)
29.4329453	-95.202858	979267.359	9.46	-10.502	979280.781	-15.290	-13.422
29.4352493	-95.1763611	979268.176	7.096	-10.593	979280.959	-14.184	-12.783
29.4331398	-95.2270584	979266.516	11.264	-10.804	979280.796	-16.504	-14.280
29.4433327	-95.2346115	979266.714	10.961	-11.487	979281.584	-17.034	-14.870
29.4931107	-95.206192	979268.28	9.715	-14.156	979285.434	-19.073	-17.154
29.4903889	-95.2021408	979268.32	8.859	-14.170	979285.224	-18.653	-16.904
29.4980831	-95.2024689	979268.744	8.829	-14.350	979285.819	-18.819	-17.075
29.4969444	-95.1909409	979269.531	7.364	-13.927	979285.731	-17.654	-16.200
29.4906387	-95.1970825	979268.667	9.141	-13.755	979285.243	-18.381	-16.576
29.4899158	-95.1814423	979269.284	6.699	-13.836	979285.187	-17.226	-15.903
29.5002785	-95.1809998	979270.115	6.897	-13.746	979285.989	-17.236	-15.874
29.5162773	-95.1902771	979270.404	7.017	-14.658	979287.228	-18.209	-16.824
29.5200005	-95.1978607	979270.565	5.009	-15.405	979287.516	-17.940	-16.951
29.5158062	-95.1966934	979269.829	7.683	-14.991	979287.191	-18.879	-17.362
29.5170002	-95.1920547	979270.273	6.615	-14.969	979287.284	-18.317	-17.011
29.5518608	-95.3260574	979269.821	15.584	-15.354	979289.984	-23.241	-20.163
29.5520287	-95.3191376	979269.769	15.638	-15.402	979289.997	-23.316	-20.228
29.5524998	-95.3136139	979269.481	15.246	-15.848	979290.034	-23.563	-20.553
29.5523605	-95.3064194	979269.338	14.85	-16.102	979290.023	-23.617	-20.685
29.5525837	-95.2984467	979269.196	14.005	-16.522	979290.040	-23.610	-20.844
29.5563049	-95.2977219	979269.487	13.67	-16.623	979290.328	-23.541	-20.841
29.5510826	-95.2960815	979269.188	13.824	-16.470	979289.924	-23.466	-20.736
29.5599174	-95.2976379	979269.64	14.528	-16.485	979290.608	-23.837	-20.968
29.5594997	-95.2921982	979269.405	13.667	-16.953	979290.576	-23.870	-21.171
29.5583057	-95.2898026	979269.241	13.616	-17.041	979290.483	-23.931	-21.242
29.550972	-95.2903061	979268.775	13.523	-16.967	979289.915	-23.811	-21.140
29.5597229	-95.2854156	979269.212	14.996	-16.754	979290.593	-24.343	-21.381
29.5599174	-95.2808075	979269.226	13.989	-17.065	979290.608	-24.145	-21.382
29.5599995	-95.2753067	979269.206	13.519	-17.237	979290.615	-24.079	-21.409
29.5545826	-95.282608	979268.848	14.145	-16.982	979290.195	-24.140	-21.347
29.548111	-95.2777481	979268.347	14.612	-16.837	979289.693	-24.232	-21.346
29.5422497	-95.2743912	979268	14.026	-16.911	979289.239	-24.009	-21.239
29.5340004	-95.2754135	979267.449	13.591	-16.957	979288.600	-23.835	-21.151
29.5311661	-95.2663879	979267.449	12.759	-16.994	979288.381	-23.451	-20.932
29.5268898	-95.2640839	979267.207	12.892	-16.864	979288.049	-23.388	-20.842
29.521944	-95.2600021	979266.886	12.591	-16.895	979287.666	-23.267	-20.780

Latitude	Longitude	Observed Gravity_G _{obs} (mGal)	Elevation_(m)	Free Air Anomaly (mGal)	Theoretical Gravity_Gn (mGal)	Simple Bouguer Anomaly (mGal)	Residual Gravity Anomaly (mGal)
29.5251102	-95.2558594	979267.265	12.787	-16.701	979287.912	-23.172	-20.647
29.5291119	-95.251442	979267.576	12.537	-16.777	979288.222	-23.121	-20.646
29.5151386	-95.2561646	979266.882	12.416	-16.426	979287.139	-22.709	-20.257
29.5105286	-95.2528076	979266.838	12.697	-16.026	979286.782	-22.452	-19.944
29.5047226	-95.2492752	979267.283	11.816	-15.404	979286.333	-21.383	-19.050
29.5021381	-95.2491379	979267.297	11.272	-15.357	979286.133	-21.062	-18.836
29.5019722	-95.2559738	979266.722	11.954	-15.709	979286.120	-21.759	-19.398
29.5018063	-95.2648315	979266.361	12.619	-15.852	979286.107	-22.238	-19.746
29.5067215	-95.2655563	979266.536	12.494	-16.096	979286.488	-22.419	-19.952
29.5117493	-95.2657471	979266.629	12.757	-16.311	979286.877	-22.767	-20.248
29.501667	-95.2752762	979266.196	13.262	-15.808	979286.096	-22.520	-19.900
29.5022507	-95.2837219	979266.382	11.087	-16.338	979286.142	-21.949	-19.760
29.5034447	-95.2609482	979266.456	12.522	-15.914	979286.234	-22.251	-19.778
29.5090275	-95.2613907	979266.689	12.507	-16.118	979286.666	-22.447	-19.977
29.5091381	-95.2575836	979266.786	12.337	-16.082	979286.675	-22.325	-19.889
29.509222	-95.2526932	979266.929	12.384	-15.931	979286.681	-22.198	-19.752
29.5132504	-95.2613602	979266.943	12.594	-16.164	979286.993	-22.537	-20.050
29.513916	-95.2567749	979266.977	12.57	-16.189	979287.045	-22.550	-20.068
29.5141106	-95.2493591	979267.304	12.084	-16.027	979287.060	-22.142	-19.756
29.5108604	-95.2431946	979267.506	12.044	-15.585	979286.808	-21.681	-19.302
29.4937496	-95.2433319	979267.189	11.763	-14.665	979285.484	-20.618	-18.295
29.491972	-95.2413635	979267.202	11.469	-14.605	979285.346	-20.409	-18.144
29.4941673	-95.2333298	979267.706	10.442	-14.588	979285.516	-19.872	-17.810
29.4985008	-95.2276382	979267.939	10.529	-14.663	979285.851	-19.992	-17.912
29.5032501	-95.225502	979268.176	9.789	-15.022	979286.219	-19.976	-18.043
29.4925003	-95.2462234	979267.046	11.456	-14.806	979285.387	-20.603	-18.341
29.4845562	-95.2459412	979266.857	11.623	-14.328	979284.772	-20.211	-17.915
29.4747772	-95.2460556	979266.672	11.365	-13.836	979284.016	-19.588	-17.344
29.4731388	-95.2358627	979266.745	11.074	-13.726	979283.889	-19.331	-17.144
29.4666939	-95.230835	979266.845	11.618	-12.960	979283.390	-18.840	-16.545
29.4678059	-95.2453079	979266.741	11.188	-13.283	979283.476	-18.945	-16.735
29.470417	-95.2529755	979266.545	11.544	-13.571	979283.678	-19.413	-17.133
29.4624729	-95.2514725	979266.586	11.324	-12.983	979283.064	-18.714	-16.478
29.4581661	-95.240448	979266.798	11.037	-12.527	979282.731	-18.112	-15.933
29.451889	-95.2448044	979266.652	11.217	-12.132	979282.245	-17.808	-15.593
29.4436111	-95.2451401	979266.433	11.397	-11.655	979281.605	-17.423	-15.172

Latitude	Longitude	Observed Gravity_G _{obs} (mGal)	Elevation_(m)	Free Air Anomaly (mGal)	Theoretical Gravity_Gn (mGal)	Simple Bouguer Anomaly (mGal)	Residual Gravity Anomaly (mGal)
29.4524174	-95.2269974	979267.184	11.293	-11.617	979282.286	-17.332	-15.102
29.4419727	-95.2262802	979267.051	10.698	-11.126	979281.478	-16.540	-14.427
29.4406662	-95.2179184	979267.193	10.105	-11.066	979281.377	-16.180	-14.184
29.440527	-95.2100525	979267.425	9.597	-10.980	979281.367	-15.837	-13.942
29.433528	-95.2180557	979267.001	10.406	-10.613	979280.826	-15.880	-13.825
29.4249992	-95.2208328	979266.268	11.535	-10.339	979280.166	-16.176	-13.898
29.4172497	-95.2369995	979265.484	12.033	-10.370	979279.568	-16.460	-14.084
29.409111	-95.2418594	979265.262	12.321	-9.874	979278.939	-16.110	-13.677
29.3988342	-95.2474442	979265.087	10.496	-9.819	979278.145	-15.131	-13.058
29.3739166	-95.2617493	979264.118	9.251	-9.248	979276.221	-13.930	-12.103
29.4055004	-95.2342529	979264.994	11.206	-10.208	979278.660	-15.879	-13.666
29.4171391	-95.2274475	979265.746	11.899	-10.141	979279.559	-16.163	-13.813
29.4059162	-95.2179413	979265.535	11.366	-9.649	979278.692	-15.402	-13.157
29.4353886	-95.1915283	979267.836	8.533	-10.500	979280.969	-14.819	-13.133
29.4414444	-95.1769409	979268.232	8.109	-10.703	979281.438	-14.807	-13.206
29.4481106	-95.1772766	979268.524	7.9	-10.991	979281.953	-14.989	-13.429
29.4546947	-95.1775589	979268.636	7.877	-11.395	979282.462	-15.382	-13.826
29.4238338	-95.175972	979267.565	8.447	-9.905	979280.076	-14.180	-12.511
29.4127502	-95.1747513	979267.039	9.153	-9.356	979279.220	-13.988	-12.181
29.4025841	-95.1755524	979266.29	9.272	-9.283	979278.434	-13.976	-12.144
29.4116116	-95.2010574	979266.147	10.784	-9.657	979279.132	-15.115	-12.985
29.3968048	-95.2489471	979265.035	10.208	-9.803	979277.988	-14.969	-12.953
29.3433609	-95.2821121	979263.158	8.216	-8.169	979273.863	-12.327	-10.705
29.3641949	-95.2902756	979263.417	8.759	-9.350	979275.470	-13.783	-12.053
29.3833065	-95.2837524	979263.934	9.894	-9.958	979276.946	-14.966	-13.012
29.3988609	-95.2523346	979265.063	10.724	-9.774	979278.147	-15.202	-13.084
29.3425827	-95.2799759	979263.176	8.505	-8.002	979273.802	-12.306	-10.626
29.3231392	-95.2931976	979262.44	7.088	-7.675	979272.303	-11.263	-9.863
29.4551945	-95.3391953	979264.048	14.166	-14.081	979282.501	-21.250	-18.453
29.4539165	-95.3286667	979264.304	14.247	-13.701	979282.402	-20.912	-18.098
29.4457226	-95.329834	979264.078	13.625	-13.486	979281.768	-20.381	-17.690
29.4467506	-95.3085861	979264.396	14.015	-13.127	979281.848	-20.220	-17.452
29.4392776	-95.3158035	979264.29	13.669	-12.762	979281.270	-19.680	-16.980
29.4260006	-95.3022766	979264.494	12.68	-11.837	979280.244	-18.254	-15.750
29.4307785	-95.2866364	979264.941	13.19	-11.602	979280.613	-18.277	-15.672
29.4245834	-95.281723	979264.894	13.18	-11.173	979280.134	-17.843	-15.240

Latitude	Longitude	Observed Gravity_G _{obs} (mGal)	Elevation_(m)	Free Air Anomaly (mGal)	Theoretical Gravity_Gn (mGal)	Simple Bouguer Anomaly (mGal)	Residual Gravity Anomaly (mGal)
29.4191952	-95.2870865	979264.912	11.901	-11.133	979279.718	-17.156	-14.806
29.4121952	-95.2941971	979264.678	11.357	-10.994	979279.177	-16.742	-14.499
29.4083881	-95.3091354	979264.223	11.375	-11.150	979278.883	-16.906	-14.660
29.403223	-95.3199692	979263.694	11.339	-11.291	979278.484	-17.029	-14.790
29.3968334	-95.3333588	979263.298	11.118	-11.261	979277.990	-16.888	-14.692
29.3984451	-95.3409729	979263.305	10.781	-11.483	979278.115	-16.939	-14.810
29.4052773	-95.345253	979263.413	11.089	-11.807	979278.643	-17.419	-15.230
29.3898335	-95.3411407	979263.051	10.24	-11.239	979277.450	-16.421	-14.399
29.3876667	-95.3456421	979262.892	10.164	-11.254	979277.282	-16.398	-14.390
29.3902779	-95.3248062	979263.189	10.71	-10.990	979277.484	-16.410	-14.295
29.3982773	-95.3070526	979263.894	10.748	-10.891	979278.102	-16.330	-14.208
29.4016113	-95.2995834	979264.207	11.245	-10.682	979278.359	-16.373	-14.152
29.4033337	-95.2842484	979264.519	10.877	-10.617	979278.492	-16.121	-13.973
29.414278	-95.2733612	979265.138	12.308	-10.402	979279.338	-16.631	-14.200
29.4118614	-95.2613602	979265.141	12.699	-10.091	979279.151	-16.518	-14.010
29.4054165	-95.2675552	979265.06	11.119	-10.162	979278.653	-15.789	-13.593
29.399334	-95.2727509	979264.726	11.025	-10.055	979278.183	-15.635	-13.457
29.3925285	-95.277916	979264.376	10.155	-10.148	979277.658	-15.287	-13.282
29.3865833	-95.2904968	979263.989	10.07	-10.102	979277.199	-15.198	-13.210
29.3830547	-95.2979202	979263.666	10.167	-10.123	979276.926	-15.268	-13.260
29.3772221	-95.3103027	979263.335	9.442	-10.227	979276.476	-15.006	-13.141
29.3720837	-95.322197	979263.187	7.791	-10.488	979276.079	-14.431	-12.892
29.3678894	-95.3299179	979262.464	8.589	-10.641	979275.755	-14.988	-13.291
29.3624439	-95.3413086	979261.689	10.112	-10.526	979275.335	-15.643	-13.646
29.3577213	-95.3576965	979261.178	10.664	-10.502	979274.971	-15.899	-13.793
29.3681946	-95.3596954	979261.651	10.282	-10.955	979275.779	-16.159	-14.128
29.3810558	-95.3659973	979262.134	10.06	-11.533	979276.772	-16.625	-14.638
29.3962784	-95.3775864	979262.29	11.17	-12.210	979277.947	-17.863	-15.657
29.3508339	-95.3470001	979261.046	10.908	-10.027	979274.439	-15.547	-13.393
29.3428059	-95.3419418	979260.938	11.025	-9.479	979273.820	-15.059	-12.882
29.3325558	-95.337944	979260.905	9.776	-9.107	979273.029	-14.055	-12.124
29.3351936	-95.3248367	979261.482	9.485	-8.823	979273.232	-13.624	-11.750
29.3399448	-95.3146973	979262.083	8.802	-8.800	979273.599	-13.254	-11.516
29.3525276	-95.3015518	979263.028	8.07	-9.051	979274.570	-13.136	-11.542
29.3720551	-95.2841644	979263.627	9.606	-9.486	979276.077	-14.347	-12.450
29.369833	-95.2753601	979263.803	9.067	-9.304	979275.905	-13.893	-12.102

Latitude	Longitude	Observed Gravity_G _{obs} (mGal)	Elevation_(m)	Free Air Anomaly (mGal)	Theoretical Gravity_Gn (mGal)	Simple Bouguer Anomaly (mGal)	Residual Gravity Anomaly (mGal)
29.3745556	-95.2929688	979263.624	9.582	-9.689	979276.270	-14.538	-12.646
29.3869991	-95.2727814	979264.241	9.809	-9.963	979277.231	-14.927	-12.990
29.3965549	-95.2654724	979264.795	10.182	-10.032	979277.969	-15.185	-13.174
29.377306	-95.2597198	979264.242	9.086	-9.436	979276.482	-14.035	-12.240
29.3568611	-95.2720566	979263.477	8.202	-8.896	979274.904	-13.047	-11.427
29.3465271	-95.2782211	979263.253	8.156	-8.337	979274.107	-12.465	-10.854
29.3335552	-95.2861099	979263.133	7.017	-7.808	979273.106	-11.359	-9.973
29.2896938	-95.3237228	979259.419	7.833	-7.888	979269.724	-11.852	-10.305
29.3351669	-95.2716675	979263.128	7.134	-7.901	979273.230	-11.511	-10.102
29.3247509	-95.2613297	979262.982	6.668	-7.387	979272.427	-10.762	-9.445
29.3407784	-95.2577209	979263.58	7.277	-7.838	979273.663	-11.520	-10.083
29.3537216	-95.2564163	979263.786	8.435	-8.273	979274.662	-12.542	-10.876
29.3689728	-95.2548599	979264.185	8.489	-9.034	979275.839	-13.330	-11.654
29.3853607	-95.2456131	979264.868	9.551	-9.289	979277.104	-14.122	-12.236
29.393362	-95.2377472	979264.999	10.66	-9.434	979277.722	-14.828	-12.723
29.3811111	-95.2325287	979265.062	10.094	-8.599	979276.776	-13.708	-11.714
29.3699436	-95.2240829	979264.918	8.569	-8.352	979275.914	-12.688	-10.996
29.3592491	-95.228775	979264.77	7.649	-7.958	979275.089	-11.829	-10.319
29.3465271	-95.2330856	979264.253	7.611	-7.505	979274.107	-11.357	-9.854
29.3303051	-95.2444458	979263.559	6.455	-7.304	979272.855	-10.571	-9.296
29.3211937	-95.2529449	979263.126	7.932	-6.579	979272.153	-10.593	-9.027
29.3556938	-95.2086105	979264.603	7.407	-7.925	979274.814	-11.674	-10.211
29.3493881	-95.20047	979264.353	8.312	-7.409	979274.328	-11.616	-9.975
29.3444176	-95.1940536	979264.236	7.406	-7.423	979273.944	-11.171	-9.708
29.3681393	-95.2097244	979265.142	8.385	-8.045	979275.775	-12.289	-10.633
29.3633614	-95.2041702	979264.769	9.098	-7.829	979275.406	-12.434	-10.637
29.3746948	-95.191864	979265.523	7.668	-8.391	979276.281	-12.272	-10.758
29.3737507	-95.181778	979265.399	8.555	-8.169	979276.208	-12.498	-10.809
29.3904724	-95.1841125	979265.64	10.487	-8.623	979277.499	-13.930	-11.859
29.3966389	-95.1781693	979266.173	10.285	-8.628	979277.975	-13.833	-11.802
29.3782768	-95.1997757	979265.507	8.906	-8.302	979276.557	-12.809	-11.050
29.3828888	-95.2070313	979265.343	10.089	-8.457	979276.913	-13.563	-11.570
29.3907509	-95.211586	979265.462	10.63	-8.778	979277.521	-14.158	-12.059
29.3973064	-95.2083588	979265.446	11.242	-9.112	979278.027	-14.801	-12.581
29.3994713	-95.1947479	979265.671	11.474	-8.982	979278.194	-14.789	-12.523
29.3998337	-95.1843643	979266.241	10.227	-8.825	979278.222	-14.001	-11.981

Latitude	Longitude	Observed Gravity_G _{obs} (mGal)	Elevation_(m)	Free Air Anomaly (mGal)	Theoretical Gravity_Gn (mGal)	Simple Bouguer Anomaly (mGal)	Residual Gravity Anomaly (mGal)
29.3805008	-95.2152481	979265.018	10.264	-8.544	979276.729	-13.738	-11.711
29.393055	-95.2254715	979265.164	10.912	-9.167	979277.698	-14.689	-12.534
29.4025555	-95.2318344	979265.015	11.405	-9.898	979278.432	-15.670	-13.417
29.5435009	95.3330002	979269.116	15.678	-15.382	979289.336	-23.316	-20.220
29.5418892	-95.3416977	979268.891	16.605	-15.196	979289.211	-23.600	-20.320
29.5465279	-95.3438644	979269.436	16.17	-15.145	979289.571	-23.328	-20.135
29.5500278	-95.3469467	979269.803	15.995	-15.103	979289.842	-23.198	-20.039
29.5434723	-95.3478622	979269.122	16.137	-15.232	979289.334	-23.399	-20.212
29.5377769	-95.3476105	979268.477	16.201	-15.416	979288.893	-23.615	-20.416
29.5336952	-95.3391113	979268.043	16.259	-15.516	979288.577	-23.745	-20.534
29.5271397	-95.3361664	979267.563	16.42	-15.439	979288.069	-23.749	-20.506
29.5246658	-95.3412781	979267.089	16.932	-15.563	979287.877	-24.132	-20.788
29.5165825	-95.3359756	979266.479	16.837	-15.576	979287.251	-24.097	-20.772
29.5290546	-95.3471909	979267.427	16.641	-15.655	979288.217	-24.076	-20.790
29.5195274	-95.3519745	979266.379	17.497	-15.701	979287.479	-24.556	-21.100
29.5154724	-95.3414459	979266.261	17.106	-15.625	979287.165	-24.282	-20.904
29.5118332	-95.3513031	979265.851	17.319	-15.688	979286.883	-24.453	-21.032
29.5061398	-95.3501358	979265.048	18.022	-15.833	979286.443	-24.954	-21.395
29.5099716	-95.3463898	979265.855	16.36	-15.836	979286.739	-24.115	-20.884
29.4990826	-95.3570251	979265.018	17.248	-15.556	979285.896	-24.285	-20.878
29.5015564	-95.3644409	979265.199	17.378	-15.526	979286.088	-24.321	-20.889
29.5096111	-95.3723602	979265.803	17.539	-15.496	979286.711	-24.372	-20.908
29.5191383	-95.3663864	979266.13	18.378	-15.648	979287.449	-24.949	-21.319
29.5192509	-95.3575821	979266.321	17.351	-15.782	979287.458	-24.563	-21.137
29.5193615	-95.3490829	979266.358	17.853	-15.599	979287.466	-24.634	-21.108
29.5300827	-95.3570862	979267.401	17.127	-15.610	979288.297	-24.278	-20.896
29.5297508	-95.3735275	979267.223	17.864	-15.535	979288.271	-24.576	-21.048
29.5356941	-95.3658905	979267.957	17.373	-15.413	979288.731	-24.205	-20.774
29.5401115	-95.3598328	979268.521	17.069	-15.285	979289.074	-23.924	-20.553
29.5436935	-95.3561401	979268.841	17.402	-15.140	979289.351	-23.947	-20.510
29.5515842	-95.365387	979269.814	16.553	-15.040	979289.963	-23.418	-20.149
29.5586948	-95.3525009	979270.599	16.056	-14.960	979290.514	-23.085	-19.915
29.5589447	-95.3427505	979270.624	16.033	-14.961	979290.533	-23.075	-19.909
29.559	-95.3284454	979270.469	15.859	-15.174	979290.537	-23.200	-20.068
29.5591946	-95.3151703	979270.156	14.547	-15.907	979290.552	-23.269	-20.396
29.5623894	-95.3078079	979270.214	14.663	-16.061	979290.800	-23.482	-20.586

Latitude	Longitude	Observed Gravity_G _{obs} (mGal)	Elevation_(m)	Free Air Anomaly (mGal)	Theoretical Gravity_Gn (mGal)	Simple Bouguer Anomaly (mGal)	Residual Gravity Anomaly (mGal)
29.5695	-95.3015518	979270.542	14.35	-16.381	979291.351	-23.643	-20.809
29.5690002	-95.2949142	979270.149	14.199	-16.782	979291.312	-23.967	-21.163
29.569416	-95.2869186	979269.988	14.849	-16.774	979291.345	-24.289	-21.357
29.5692787	-95.2767487	979269.752	13.345	-17.464	979291.334	-24.217	-21.582
29.5693607	-95.2707748	979269.797	13.2	-17.470	979291.340	-24.150	-21.543
29.5725555	-95.2629166	979270.099	13.164	-17.427	979291.588	-24.089	-21.489
29.5675831	-95.2581406	979269.778	11.881	-17.758	979291.203	-23.771	-21.425
29.5592785	-95.2606125	979269.057	12.86	-17.533	979290.559	-24.042	-21.502
29.5529995	-95.2670593	979268.548	14.223	-17.135	979290.072	-24.333	-21.524
29.5582218	-95.2685852	979268.868	14.022	-17.282	979290.477	-24.378	-21.609
29.565834	-95.2681427	979269.616	13.114	-17.404	979291.067	-24.041	-21.451
29.5696106	-95.262558	979269.81	8.901	-18.803	979291.360	-23.308	-21.550
29.5639992	-95.2836075	979269.332	14.108	-17.239	979290.925	-24.379	-21.593
29.563055	-95.2938309	979269.685	13.904	-16.876	979290.852	-23.912	-21.167
29.5704994	-95.2945023	979270.235	14.667	-16.667	979291.429	-24.090	-21.194
29.5816116	-95.2950287	979270.882	13.859	-17.131	979292.290	-24.145	-21.408
29.5901108	-95.295639	979271.343	13.845	-17.334	979292.949	-24.340	-21.606
29.5869446	-95.2867813	979271.143	13.561	-17.376	979292.704	-24.239	-21.561
29.5951385	-95.2862778	979271.641	13.471	-17.541	979293.339	-24.359	-21.698
29.5784168	-95.2866364	979270.54	14.112	-17.147	979292.042	-24.289	-21.502
29.5709991	-95.2864456	979270.003	14.101	-17.113	979291.467	-24.249	-21.464
29.5741386	-95.2773895	979270.085	12.956	-17.628	979291.711	-24.184	-21.626
29.5850563	-95.2779465	979270.927	13.252	-17.541	979292.557	-24.247	-21.630
29.5946388	-95.2773895	979271.769	12.516	-17.669	979293.300	-24.003	-21.531
29.5906658	-95.2659454	979271.248	13.213	-17.667	979292.992	-24.354	-21.744
29.5757504	-95.265419	979270.155	13.193	-17.609	979291.836	-24.286	-21.681
29.5756111	-95.2559433	979270.324	13.021	-17.483	979291.825	-24.072	-21.501
29.583416	-95.2486954	979270.855	12.938	-17.582	979292.430	-24.130	-21.575
29.5843048	-95.2378922	979271.468	11.223	-17.568	979292.499	-23.247	-21.031
29.5927773	-95.2428055	979272.087	12.144	-17.321	979293.156	-23.467	-21.069
29.5785828	-95.2340851	979271.208	10.649	-17.561	979292.055	-22.950	-20.847
29.5760555	-95.2227249	979271.451	10.023	-17.315	979291.859	-22.388	-20.408
29.5813885	-95.2167206	979271.962	9.821	-17.280	979292.273	-22.250	-20.311
29.5773621	-95.2047195	979272.14	9.206	-16.980	979291.961	-21.639	-19.821
29.5671673	-95.2056656	979271.553	8.83	-16.892	979291.170	-21.361	-19.617
29.5674725	-95.2178574	979270.813	11.201	-16.924	979291.194	-22.593	-20.381

Latitude	Longitude	Observed Gravity_G _{obs} (mGal)	Elevation_(m)	Free Air Anomaly (mGal)	Theoretical Gravity_Gn (mGal)	Simple Bouguer Anomaly (mGal)	Residual Gravity Anomaly (mGal)
29.5706673	-95.2282257	979270.706	11.558	-17.169	979291.442	-23.018	-20.736
29.5563049	-95.2405853	979269.445	11.665	-17.284	979290.328	-23.187	-20.883
29.5642509	-95.3078918	979270.279	14.577	-16.167	979290.944	-23.544	-20.665
29.5766659	-95.3080292	979271.023	14.351	-16.455	979291.907	-23.718	-20.884
29.5874443	-95.3098068	979271.752	14.216	-16.603	979292.742	-23.798	-20.990
29.5871391	-95.3210526	979271.975	15.014	-16.110	979292.719	-23.709	-20.744
29.5681114	-95.3208618	979270.916	14.858	-15.742	979291.243	-23.262	-20.327
29.5651951	-95.3269196	979270.829	15.4	-15.436	979291.017	-23.230	-20.188
29.5737782	-95.3296127	979271.438	15.49	-15.465	979291.683	-23.304	-20.245
29.5818882	-95.3336411	979272.18	14.896	-15.535	979292.312	-23.073	-20.132
29.5857773	-95.3404465	979272.753	14.675	-15.331	979292.613	-22.758	-19.860
29.5745564	-95.3505859	979272.016	15.918	-14.815	979291.743	-22.871	-19.727
29.5903053	-95.353447	979273.709	15.02	-14.620	979292.964	-22.222	-19.255
29.5820274	-95.3715591	979272.422	18.302	-14.252	979292.322	-23.515	-19.900
29.6028614	-95.2858887	979272.355	13.399	-17.448	979293.938	-24.229	-21.583
29.6095009	-95.2854462	979272.879	13.21	-17.498	979294.453	-24.183	-21.574
29.6111946	-95.2775574	979273.296	13.096	-17.247	979294.585	-23.875	-21.289
29.6121387	-95.2710037	979273.383	13.729	-17.038	979294.658	-23.986	-21.275
29.6068897	-95.2602463	979273.026	13.944	-16.922	979294.251	-23.978	-21.225
29.6106949	-95.2569199	979273.744	12.863	-16.832	979294.546	-23.342	-20.802
29.604084	-95.2496643	979273.194	13.185	-16.770	979294.033	-23.443	-20.839
29.6109715	-95.2422485	979274.357	12.026	-16.499	979294.567	-22.585	-20.210
29.604166	-95.2435532	979273.274	12.527	-16.900	979294.039	-23.239	-20.765
29.6110287	-95.2289429	979274.693	11.16	-16.435	979294.572	-22.083	-19.879
29.6111393	-95.222641	979274.804	10.543	-16.523	979294.580	-21.859	-19.776
29.6179714	-95.2291412	979275.196	12.842	-15.952	979295.111	-22.451	-19.915
29.6278057	-95.2328873	979276.793	10.744	-15.765	979295.874	-21.203	-19.081
29.6193619	-95.2421417	979275.368	12.17	-16.095	979295.218	-22.254	-19.850
29.6273613	-95.2474747	979276.014	13.082	-15.788	979295.839	-22.409	-19.825
29.619194	-95.2498627	979275.019	12.476	-16.336	979295.205	-22.650	-20.186
29.6268616	-95.2586975	979275.747	13.041	-16.029	979295.801	-22.629	-20.054
29.6263885	-95.2718887	979275.574	13.165	-16.127	979295.764	-22.790	-20.190
29.6246662	-95.2856979	979274.818	14.446	-16.354	979295.630	-23.665	-20.812
29.620945	-95.3037796	979274.004	14.782	-16.776	979295.341	-24.257	-21.337
29.6204166	-95.3177795	979274.352	14.874	-16.358	979295.300	-23.886	-20.948
29.6078053	-95.3320312	979273.975	15.223	-15.649	979294.322	-23.353	-20.347

Latitude	Longitude	Observed Gravity_G_{obs} (mGal)	Elevation_(m)	Free Air Anomaly (mGal)	Theoretical Gravity_Gn (mGal)	Simple Bouguer Anomaly (mGal)	Residual Gravity Anomaly (mGal)
29.6078606	-95.3526077	979274.996	16.052	-14.376	979294.326	-22.500	-19.330
29.6082497	-95.3662491	979275.63	16.119	-13.752	979294.356	-21.910	-18.726
29.6123047	-95.3758316	979275.899	17.01	-13.523	979294.671	-22.131	-18.772
29.6210003	-95.3671112	979276.778	15.094	-13.910	979295.346	-21.548	-18.568
29.6207771	-95.3600845	979276.776	15.223	-13.854	979295.328	-21.559	-18.552
29.6262226	-95.3440552	979277.06	12.83	-14.732	979295.751	-21.225	-18.691
29.626667	-95.3531113	979277.466	13.51	-14.150	979295.785	-20.987	-18.319
29.6260548	-95.3388367	979276.614	14.339	-14.699	979295.738	-21.956	-19.124
29.6258049	-95.3276138	979276.025	12.646	-15.791	979295.718	-22.191	-19.693
29.625473	-95.3171692	979275.404	12.966	-16.287	979295.693	-22.849	-20.289
29.6281109	-95.2997513	979274.885	15.227	-16.313	979295.897	-24.020	-21.012
29.6264172	-95.2900314	979274.974	14.607	-16.284	979295.766	-23.677	-20.792
29.6252232	-95.2858353	979274.821	14.741	-16.303	979295.673	-23.763	-20.852
29.6418896	-95.2882767	979277.592	13.072	-15.341	979296.967	-21.957	-19.375
29.6556396	-95.2895279	979279.498	11.889	-14.868	979298.035	-20.885	-18.537
29.6458893	-95.3138351	979278.471	11.025	-15.404	979297.278	-20.984	-18.807
29.6445007	-95.3354187	979278.921	11.086	-14.828	979297.170	-20.438	-18.249
29.6480827	-95.3549728	979279.895	11.284	-14.071	979297.448	-19.781	-17.553
29.6451111	-95.365387	979279.602	11.368	-14.107	979297.217	-19.860	-17.615

APPENDIX B – PACES GRAVITY DATASET IN NAD 83

Latitude	Longitude	Elevation (m)	Observed Gravity_ G_{obs} (mGal)	Theoretical Gravity_ G_n (mGal)	FAA (mGal)	Complete Bouguer Anomaly (mGal)
29.3269059	-95.4535496	12.8	3257.8	980969.9403	-9.95	-11.41
29.3269059	-95.4535496	12.8	3259.8	980969.9403	-7.95	-9.41
29.3332376	-95.3283772	10.7	3260.9	980970.8876	-7.99	-9.21
29.34007	-95.150042	5.2	3262.9	980971.9096	-8.21	-8.81
29.340236	-95.15021	5.2	3264.9	980971.9344	-6.23	-6.83
29.3450704	-95.2335409	7.8	3264.1	980972.6572	-6.6	-7.49
29.3452364	-95.2335409	7.8	3264.1	980972.682	-6.61	-7.5
29.3500724	-95.5785535	14.3	3255.1	980973.4049	-13.98	-15.61
29.3502394	-95.5785535	14.3	3257.1	980973.4299	-11.99	-13.62
29.3522391	-95.4990534	13.5	3259.1	980973.7288	-10.39	-11.93
29.3565689	-95.1707109	7.3	3264.8	980974.3768	-6.94	-7.78
29.3682338	-95.0895392	7.7	3264.14	980976.1213	-8.38	-9.26
29.3682338	-95.0897062	7.6	3264.14	980976.1213	-8.41	-9.28
29.3682337	-95.0890432	7.9	3264.06	980976.1213	-8.39	-9.3
29.3683998	-95.0898743	8	3264.05	980976.1461	-8.39	-9.3
29.3715676	-95.0893713	7.5	3264.42	980976.6198	-8.41	-9.27
29.3849	-95.1252077	10	3265.79	980978.6129	-7.3	-8.45
29.3853999	-95.1252077	9.6	3265.79	980978.6877	-7.46	-8.56
29.3899022	-95.1418783	9.7	3266.39	980979.3607	-7.18	-8.29
29.3902332	-95.1410392	9.4	3266.39	980979.4102	-7.3	-8.38
29.3969019	-95.1800416	11.6	3265.9	980980.4069	-7.63	-8.95
29.3969019	-95.1802096	11.6	3265.9	980980.4069	-7.63	-8.95
29.4029007	-95.1790427	11.2	3266.39	980981.3036	-7.72	-9
29.4030687	-95.1790427	11	3266.4	980981.3288	-7.79	-9.04
29.406901	-95.1918761	10.3	3266.3	980981.9015	-8.4	-9.58
29.406901	-95.1918761	10.3	3266.3	980981.9015	-8.4	-9.58
29.4135691	-95.3400512	7.6	3263.5	980982.8982	-12.55	-13.42
29.4135691	-95.3402112	7.6	3265.5	980982.8982	-10.55	-11.42
29.4197356	-95.2280485	11.9	3266.1	980983.8197	-9.1	-10.46
29.4199016	-95.2282085	12.1	3266.1	980983.8445	-9.05	-10.43
29.42357	-95.243544	15.2	3265	980984.3927	-9.47	-11.2
29.42407	-95.244047	14.7	3265.44	980984.4674	-9.23	-10.9
29.4242316	-95.09237	5.4	3270.1	980984.4922	-7.45	-8.08

Latitude	Longitude	Elevation (m)	Observed Gravity_ G_{obs} (mGal)	Theoretical Gravity_ G_n (mGal)	FAA (mGal)	Complete Bouguer Anomaly (mGal)
29.4260645	-95.091371	5.3	3268.96	980984.7662	-8.76	-9.38
29.4268975	-95.0918741	5.4	3268.94	980984.8907	-8.82	-9.45
29.4367369	-95.2490453	12.4	3266.43	980986.3604	-9.93	-11.34
29.4369019	-95.2490453	12.2	3266.41	980986.3851	-10.02	-11.41
29.441065	-95.0923703	5.3	3270.1	980987.0079	-8.78	-9.4
29.4552296	-95.0672076	3	3270.9	980989.1246	-9.79	-10.15
29.4552296	-95.0668726	3.3	3270.89	980989.1246	-9.7	-10.1
29.4603958	-95.0518722	4.1	3271	980989.8965	-9.75	-10.23
29.4605618	-95.0513762	3.9	3271	980989.9213	-9.82	-10.28
29.4649005	-95.2232118	11.6	3267.29	980990.5687	-11.49	-12.82
29.4652286	-95.0507052	4.3	3271.28	980990.6186	-9.78	-10.29
29.4652286	-95.0497062	4	3271.28	980990.6186	-9.87	-10.35
29.4660685	-95.2232118	11.4	3267.29	980990.7432	-11.64	-12.95
29.4685678	-95.3550522	16.2	3263.1	980991.1167	-14.55	-16.39
29.4685678	-95.3552192	16.2	3265.1	980991.1167	-12.55	-14.39
29.4787284	-95.0627068	5.7	3271.75	980992.6354	-9.92	-10.59
29.4788944	-95.0627068	5.5	3271.76	980992.6602	-9.99	-10.63
29.4798988	-95.2620462	12.3	3266.54	980992.8098	-13.19	-14.59
29.4798988	-95.2622142	12.1	3266.54	980992.8098	-13.25	-14.63
29.4800648	-95.2635492	13	3266.1	980992.8346	-13.42	-14.91
29.4802308	-95.2635492	13	3266.1	980992.8594	-13.44	-14.92
29.4867284	-95.0703751	5.8	3272.19	980993.8304	-10.07	-10.75
29.4868964	-95.0705421	5.8	3272.19	980993.8555	-10.08	-10.76
29.4893996	-95.2127137	9.9	3268.31	980994.2286	-12.89	-14.02
29.4948989	-95.1728785	8.7	3269.3	980995.0503	-12.7	-13.69
29.4973963	-95.0798736	6.6	3272.44	980995.4238	-10.4	-11.17
29.4973963	-95.0798736	6.4	3272.44	980995.4238	-10.46	-11.21
29.5012339	-95.2687146	13	3266.53	980995.996	-14.63	-16.11
29.5014019	-95.2688826	12.7	3266.53	980996.0211	-14.74	-16.19
29.5014024	-95.3292175	18.1	3264.8	980996.0211	-14.8	-16.86
29.5072366	-95.5020522	19.9	3266.6	980996.8923	-12.9	-15.16
29.5082304	-95.092043	7.5	3272.75	980997.0414	-10.65	-11.52
29.5082304	-95.092211	7.3	3272.76	980997.0414	-10.7	-11.55
29.5109026	-95.5262228	19.1	3268.16	980997.4397	-11.87	-14.04
29.5110706	-95.5263908	18.8	3268.16	980997.4648	-11.97	-14.11

Latitude	Longitude	Elevation (m)	Observed Gravity_ G_{obs} (mGal)	Theoretical Gravity_ G_n (mGal)	FAA (mGal)	Complete Bouguer Anomaly (mGal)
29.5129032	-95.4593868	20.1	3266.42	980997.7386	-13.45	-15.74
29.5130692	-95.4593868	19.9	3266.43	980997.7634	-13.52	-15.78
29.5219006	-95.2593842	13.4	3267.21	980999.0826	-15.43	-16.96
29.5232369	-95.5315558	18.8	3269.29	980999.2818	-11.78	-13.93
29.5249017	-95.4543895	22.1	3266.71	980999.5304	-13.48	-15.99
29.5252357	-95.4532225	22.4	3266.71	980999.5803	-13.41	-15.96
29.5255688	-95.5332189	18.8	3269.29	980999.63	-11.97	-14.11
29.5257313	-95.1683774	7.4	3271.46	980999.6548	-13.33	-14.18
29.5257314	-95.1685454	7.3	3271.46	980999.6548	-13.36	-14.2
29.5265641	-95.1082105	4.5	3273.97	980999.7793	-11.77	-12.31
29.527064	-95.1077065	4.7	3273.96	980999.854	-11.76	-12.31
29.5375639	-95.1175408	8.5	3273.6	981001.4218	-11.76	-12.75
29.5377309	-95.1177089	8.5	3273.56	981001.4468	-11.82	-12.8
29.5402319	-95.1202119	7.6	3273.54	981001.8202	-12.31	-13.19
29.5457347	-95.5487222	20.8	3269.98	981002.6412	-12.22	-14.59
29.5457347	-95.5488902	20.6	3269.99	981002.6412	-12.27	-14.62
29.5460665	-95.282715	14.2	3268.61	981002.6911	-15.65	-17.27
29.5487308	-95.1287112	8.1	3273.6	981003.0891	-12.75	-13.69
29.5488968	-95.1288792	7.9	3273.61	981003.1139	-12.82	-13.73
29.54973	-95.0955452	5.4	3275.05	981003.2384	-12.21	-12.84
29.549897	-95.0957052	5.6	3275.04	981003.2633	-12.17	-12.83
29.5515638	-95.089708	4.7	3275.35	981003.5122	-12.27	-12.82
29.5520638	-95.089541	4.9	3275.35	981003.5868	-12.25	-12.82
29.5523959	-95.0967052	5.3	3275.21	981003.6364	-12.29	-12.91
29.552396	-95.0968722	5.1	3275.21	981003.6364	-12.35	-12.95
29.553565	-95.2818839	14.7	3269	981003.8106	-15.69	-17.37
29.553565	-95.2818839	14.7	3269	981003.8106	-15.69	-17.37
29.5562307	-95.1357074	9.3	3273.49	981004.2088	-13.07	-14.15
29.5563987	-95.1357074	9.1	3273.5	981004.2338	-13.14	-14.19
29.5565681	-95.5565573	20.6	3270.48	981004.2586	-12.62	-14.97
29.5574011	-95.5572213	20.3	3270.48	981004.383	-12.78	-15.09
29.5633996	-95.2870491	15	3269.53	981005.2788	-15.83	-17.54
29.5638986	-95.2877121	15.1	3269.53	981005.3533	-15.84	-17.56
29.5648955	-95.0527049	3.7	3276.85	981005.5026	-12.11	-12.55
29.5648955	-95.0527049	3.6	3276.85	981005.5026	-12.14	-12.57

Latitude	Longitude	Elevation (m)	Observed Gravity_G _{obs} (mGal)	Theoretical Gravity_G _n (mGal)	FAA (mGal)	Complete Bouguer Anomaly (mGal)
29.5660679	-95.4377188	19.3	3270.8	981005.6768	-13.44	-15.64
29.5669019	-95.4365518	19.6	3270.8	981005.8013	-13.41	-15.64
29.5677296	-95.1468768	9	3273.78	981005.9253	-13.77	-14.81
29.5698995	-95.5668885	20.3	3271.71	981006.2488	-12.52	-14.83
29.5710665	-95.5688876	20.3	3271.71	981006.423	-12.61	-14.92
29.5733965	-95.1518749	7.6	3274.28	981006.7712	-14.14	-15.02
29.5735645	-95.1518749	7.4	3274.28	981006.7963	-14.21	-15.07
29.5802332	-95.5822239	20.4	3272.71	981007.7912	-12.29	-14.61
29.5802332	-95.5820559	20.7	3272.71	981007.7912	-12.2	-14.55
29.5820634	-95.1592072	7.5	3274.58	981008.0648	-14.54	-15.41
29.5822314	-95.1593742	7.4	3274.58	981008.0899	-14.58	-15.44
29.585234	-95.4302185	19.2	3272.93	981008.5377	-12.83	-15.01
29.585566	-95.4298835	18.8	3272.93	981008.5872	-12.97	-15.12
29.5882319	-95.5938892	21.1	3273.33	981008.9851	-12.07	-14.47
29.5882319	-95.5933931	21.4	3273.32	981008.9851	-11.99	-14.43
29.5928973	-95.1687135	8.4	3274.79	981009.6818	-14.89	-15.87
29.5930633	-95.1688735	8.2	3274.79	981009.7065	-14.97	-15.92
29.598233	-95.6198908	21.4	3272.9	981010.4776	-13.19	-15.63
29.598233	-95.6218899	21.3	3272.9	981010.4776	-13.22	-15.65
29.6003962	-95.1768767	10.5	3274.64	981010.8009	-14.98	-16.19
29.6005642	-95.1765417	10.3	3274.64	981010.8259	-15.05	-16.24
29.6058996	-95.4467219	19.1	3275.43	981011.6218	-11.96	-14.14
29.6060656	-95.4468899	18.7	3275.44	981011.6465	-12.09	-14.22
29.6062333	-95.4342165	17.2	3275.8	981011.6716	-12.2	-14.17
29.6063993	-95.4343845	16.8	3275.81	981011.6964	-12.33	-14.25
29.6128997	-95.4645524	17.4	3276.78	981012.6663	-11.68	-13.67
29.6130657	-95.4647194	17.4	3276.78	981012.691	-11.69	-13.68
29.6133987	-95.4198881	16.8	3276.61	981012.7409	-12.07	-14
29.6138987	-95.4193851	16.4	3276.61	981012.8155	-12.23	-14.11
29.6140652	-95.3977164	16.9	3276.64	981012.8404	-12.06	-14
29.6140652	-95.3977164	16.5	3276.64	981012.8404	-12.19	-14.08
29.6168965	-95.1668744	11.8	3275.06	981013.2631	-15.44	-16.79
29.6198967	-95.3433857	15	3276.28	981013.7107	-13.46	-15.18
29.6198958	-95.3052146	15.5	3274.14	981013.7107	-15.45	-17.21
29.6198956	-95.2933812	15	3273.96	981013.7107	-15.78	-17.49

Latitude	Longitude	Elevation (m)	Observed Gravity_G _{obs} (mGal)	Theoretical Gravity_G _n (mGal)	FAA (mGal)	Complete Bouguer Anomaly (mGal)
29.6203958	-95.3045515	15.3	3274.15	981013.7853	-15.54	-17.28
29.6207298	-95.3047115	15.5	3274.15	981013.8352	-15.5	-17.27
29.6207298	-95.3055506	15.6	3274.14	981013.8352	-15.48	-17.26
29.6207295	-95.2932132	15.1	3273.96	981013.8352	-15.81	-17.54
29.6210636	-95.3432177	14.6	3276.28	981013.8849	-13.67	-15.35
29.6217307	-95.219878	12.6	3276.11	981013.9842	-14.51	-15.96
29.6218947	-95.3050466	16	3273.9	981014.009	-15.69	-17.51
29.6218947	-95.3052146	16	3273.9	981014.009	-15.69	-17.51
29.6223987	-95.220213	12.7	3276.12	981014.0839	-14.52	-15.98
29.6228986	-95.6187237	22.5	3272.93	981014.1583	-14.73	-17.3
29.6230646	-95.6188917	22.2	3272.94	981014.1831	-14.82	-17.36
29.6232301	-95.5252231	21.7	3276.99	981014.2082	-10.94	-13.41
29.6232301	-95.5257182	21.2	3277	981014.2082	-11.09	-13.5
29.6233971	-95.1978813	12.9	3275.99	981014.2329	-14.67	-16.15
29.6235631	-95.1980414	13	3275.99	981014.2577	-14.65	-16.15
29.6252277	-95.2668834	13.9	3275.46	981014.5064	-15.03	-16.63
29.6253937	-95.2670434	14.1	3275.46	981014.5312	-14.99	-16.6
29.6265633	-95.5803926	24.7	3274.78	981014.7053	-12.49	-15.3
29.6265634	-95.5805526	24.3	3274.78	981014.7053	-12.61	-15.37
29.6282313	-95.6183876	25.6	3272.21	981014.954	-14.91	-17.82
29.6282305	-95.5898909	24.4	3274.22	981014.954	-13.27	-16.04
29.6282321	-95.4657194	18.8	3277.96	981014.954	-11.26	-13.41
29.6282305	-95.5910589	24	3274.23	981014.954	-13.38	-16.11
29.6282321	-95.4657194	18.8	3277.96	981014.954	-11.26	-13.41
29.6293963	-95.5102227	20.8	3277.96	981015.1283	-10.73	-13.1
29.6298982	-95.6188916	25.3	3272.21	981015.2027	-15.13	-18.01
29.641896	-95.2152079	11.2	3278.62	981016.9928	-14	-15.29
29.64573	-95.219046	10.1	3279.36	981017.5647	-13.9	-15.06
29.64573	-95.219046	9.9	3279.37	981017.5647	-13.95	-15.09
29.6473984	-95.4632162	19.2	3279.31	981017.8134	-11.27	-13.47
29.6473984	-95.4632162	19.2	3279.31	981017.8134	-11.27	-13.47
29.6502267	-95.2835469	15.2	3278.66	981018.236	-13.37	-15.12
29.6502265	-95.2785497	15	3278.71	981018.236	-13.39	-15.11
29.6508944	-95.3137138	11.3	3279.44	981018.3354	-13.85	-15.15
29.6510604	-95.3138818	10.9	3279.44	981018.3602	-13.99	-15.24

Latitude	Longitude	Elevation (m)	Observed Gravity_ G_{obs} (mGal)	Theoretical Gravity_ G_n (mGal)	FAA (mGal)	Complete Bouguer Anomaly (mGal)
29.6540592	-95.2748796	15.2	3278.9	981018.8077	-13.43	-15.18
29.6540592	-95.2748796	15.2	3278.87	981018.8077	-13.46	-15.21
29.6540593	-95.2765507	15.2	3278.83	981018.8077	-13.5	-15.25
29.6543932	-95.2763826	15	3278.89	981018.8575	-13.53	-15.24
29.6615624	-95.6183875	26.91	3272.23	981019.9264	-17.07	-20.13
29.6615625	-95.6190585	26.51	3272.24	981019.9264	-17.19	-20.2
29.6622283	-95.3303852	13.2	3280.21	981020.026	-13.37	-14.89
29.6630639	-95.2352134	9	3280.89	981020.1502	-14.05	-15.09
29.6633959	-95.2352134	9.2	3280.89	981020.1997	-14.02	-15.08
29.6645629	-95.2367165	10.1	3280.89	981020.3738	-13.83	-15
29.6647289	-95.2368765	9.9	3280.89	981020.3986	-13.91	-15.05
29.6652304	-95.4148827	16.7	3278.79	981020.4734	-13.95	-15.86
29.6652304	-95.4148827	17	3278.78	981020.4734	-13.86	-15.81
29.665395	-95.1670425	13.2	3280.6	981020.4982	-13.23	-14.74
29.6675627	-95.3935501	16.4	3279.8	981020.8214	-13.21	-15.09
29.6677287	-95.3935501	16.4	3279.76	981020.8461	-13.26	-15.14
29.6695646	-95.4618891	17.2	3280.82	981021.1197	-12.1	-14.07
29.6697305	-95.4618891	16.7	3280.82	981021.1444	-12.27	-14.18
29.6708979	-95.2427126	8.7	3281.89	981021.3186	-13.75	-14.76
29.6710639	-95.2427126	8.5	3281.89	981021.3434	-13.83	-14.81
29.6715622	-95.6267266	26.21	3272.75	981021.4178	-17.55	-20.53
29.6715622	-95.6268866	25.91	3272.76	981021.4178	-17.63	-20.58
29.6733943	-95.3877139	14.5	3280.94	981021.6911	-13.11	-14.77
29.6735623	-95.3877139	14.1	3280.94	981021.7162	-13.25	-14.86
29.6808961	-95.459386	16.3	3281.46	981022.8096	-12.62	-14.48
29.6810641	-95.459386	15.5	3281.47	981022.8347	-12.87	-14.64
29.6827249	-95.2527149	6.7	3283.85	981023.0833	-13.33	-14.12
29.6832279	-95.3552189	13.1	3283.1	981023.1578	-12.15	-13.65
29.6832279	-95.3552189	13.1	3283.1	981023.1578	-12.15	-13.65
29.6883968	-95.220213	8.5	3284.51	981023.9283	-12.56	-13.54
29.6888958	-95.220549	8.4	3284.53	981024.0027	-12.61	-13.58
29.692725	-95.0552073	7	3281.71	981024.5744	-16.16	-16.97
29.693057	-95.0548723	6.9	3281.71	981024.6239	-16.21	-17.01
29.6935586	-95.3300492	12.1	3284.1	981024.6985	-12.26	-13.65
29.6935587	-95.3302172	12.1	3284.1	981024.6985	-12.26	-13.65

Latitude	Longitude	Elevation (m)	Observed Gravity_ G_{obs} (mGal)	Theoretical Gravity_ G_n (mGal)	FAA (mGal)	Complete Bouguer Anomaly (mGal)
29.6945595	-95.3270511	11.2	3284.58	981024.8477	-12.13	-13.42
29.6947255	-95.3272181	11.4	3284.6	981024.8725	-12.06	-13.38
29.6957232	-95.0668737	9.1	3281.6	981025.0214	-15.85	-16.9
29.6957232	-95.0668737	9	3281.61	981025.0214	-15.87	-16.91
29.6958905	-95.2652123	8.1	3285.01	981025.0465	-12.76	-13.71
29.6960584	-95.3268831	11.1	3284.71	981025.0712	-12.15	-13.43
29.6960565	-95.2652123	7.9	3285.03	981025.0712	-12.82	-13.74
29.6998914	-95.079378	8.1	3282.29	981025.6429	-15.79	-16.73
29.7023914	-95.2745435	9.4	3285.8	981026.0158	-12.08	-13.16
29.7023914	-95.2747115	9.2	3285.81	981026.0158	-12.13	-13.2
29.7040577	-95.0947065	8.7	3282.96	981026.264	-15.26	-16.27
29.7043907	-95.0948745	8.8	3282.96	981026.3137	-15.26	-16.28
29.7095611	-95.219542	8.2	3286.98	981027.084	-11.82	-12.78
29.7097271	-95.219382	8.1	3286.98	981027.1088	-11.87	-12.82
29.7098919	-95.3312162	12.6	3285.53	981027.1338	-11.94	-13.39
29.7098919	-95.3313842	12.3	3285.53	981027.1338	-12.03	-13.45
29.7107286	-95.2030465	8.8	3287.07	981027.2581	-11.64	-12.66
29.7107261	-95.114711	7	3284.46	981027.2581	-14.8	-15.62
29.7112259	-95.1452069	6.5	3286.12	981027.3325	-13.34	-14.11
29.7113919	-95.1447109	6.4	3286.12	981027.3573	-13.38	-14.13
29.7113915	-95.1302065	7.7	3285.28	981027.3573	-13.82	-14.71
29.7115616	-95.2028785	9	3287.07	981027.3823	-11.64	-12.68
29.7115604	-95.1602143	8.3	3286.54	981027.3823	-12.39	-13.35
29.7115604	-95.1598783	8.2	3286.54	981027.3823	-12.42	-13.37
29.7118915	-95.1298785	7.8	3285.28	981027.4318	-13.83	-14.73
29.7127274	-95.1977134	7.4	3287.51	981027.5562	-11.79	-12.66
29.7127274	-95.1973774	7.5	3287.51	981027.5562	-11.76	-12.64
29.7127268	-95.1753737	8.8	3286.98	981027.5562	-11.88	-12.9
29.7127268	-95.1752137	8.7	3286.98	981027.5562	-11.92	-12.92
29.7132261	-95.1882151	7.5	3287.33	981027.6306	-11.97	-12.85
29.7132261	-95.1873751	7.4	3287.35	981027.6306	-11.99	-12.85
29.714894	-95.21871	4.5	3288.24	981027.8791	-12.12	-12.66
29.714894	-95.218878	4.4	3288.25	981027.8791	-12.14	-12.67
29.7178899	-95.2833788	10.6	3286.85	981028.3265	-11.86	-13.08
29.7182228	-95.2837148	11.5	3286.85	981028.3761	-11.61	-12.93

Latitude	Longitude	Elevation (m)	Observed Gravity_G _{obs} (mGal)	Theoretical Gravity_G _n (mGal)	FAA (mGal)	Complete Bouguer Anomaly (mGal)
29.7185608	-95.4018822	18	3283.72	981028.4259	-12.76	-14.81
29.7190616	-95.2118818	6.3	3288.56	981028.5004	-11.57	-12.31
29.7195616	-95.2123778	6.4	3288.55	981028.575	-11.59	-12.34
29.7243916	-95.112712	4.1	3286.56	981029.2954	-14.66	-15.16
29.7252246	-95.113376	4.1	3286.55	981029.4196	-14.74	-15.23
29.7258937	-95.221213	3.2	3289.46	981029.5189	-12.16	-12.55
29.7260617	-95.221381	3.1	3289.46	981029.5439	-12.2	-12.58
29.7287214	-95.2582161	2.3	3289.51	981029.9413	-12.6	-12.9
29.7287214	-95.257377	2.4	3289.39	981029.9413	-12.69	-13
29.7288874	-95.2582161	2.2	3289.53	981029.966	-12.63	-12.91
29.7288873	-95.257377	2.2	3289.39	981029.966	-12.77	-13.05
29.7290556	-95.2637092	7.9	3288.25	981029.9911	-12.16	-13.08
29.7292216	-95.2640452	8.2	3288.25	981030.0158	-12.08	-13.03
29.7298905	-95.293381	9.4	3287.68	981030.1154	-12.33	-13.43
29.7298905	-95.293045	9.2	3287.69	981030.1154	-12.39	-13.46
29.7307263	-95.2128808	4.8	3290.03	981030.2393	-11.47	-12.04
29.7310603	-95.2122098	4.7	3290.04	981030.2891	-11.52	-12.08
29.7320621	-95.2415456	8.2	3288.81	981030.4383	-11.74	-12.7
29.7322281	-95.2415456	8	3288.82	981030.463	-11.81	-12.75
29.7332273	-95.2157119	5.4	3290	981030.6121	-11.51	-12.15
29.7332273	-95.2140488	4.4	3290.35	981030.6121	-11.47	-12
29.7335611	-95.4285549	18	3282.96	981030.6618	-14.69	-16.75
29.733561	-95.4268838	18	3282.91	981030.6618	-14.74	-16.8
29.7338943	-95.2138808	4.3	3290.36	981030.7115	-11.54	-12.06
29.7340557	-95.3040473	9.9	3288.03	981030.7362	-12.15	-13.31
29.7340556	-95.3032153	9.7	3288.03	981030.7362	-12.22	-13.35
29.7353882	-95.2628782	11.1	3288.06	981030.9351	-11.86	-13.14
29.7355531	-95.2630462	10.9	3288.06	981030.9596	-11.93	-13.19
29.7368946	-95.4185526	18.4	3283.3	981031.1588	-14.48	-16.59
29.7368946	-95.4185526	18.4	3283.3	981031.1588	-14.48	-16.59
29.7377228	-95.3405474	13	3287.25	981031.2826	-12.26	-13.76
29.7378958	-95.4820533	18.9	3282.46	981031.3077	-15.25	-17.41
29.7380618	-95.4823894	18.6	3282.47	981031.3324	-15.34	-17.47
29.7383907	-95.3398833	13.1	3287.25	981031.3822	-12.28	-13.79
29.7432232	-95.3332151	12.4	3288.01	981032.1025	-12.12	-13.54

Latitude	Longitude	Elevation (m)	Observed Gravity_ G_{obs} (mGal)	Theoretical Gravity_ G_n (mGal)	FAA (mGal)	Complete Bouguer Anomaly (mGal)
29.7433892	-95.3332151	12.7	3288.01	981032.1273	-12.04	-13.5
29.7465547	-95.5233904	19.81	3281.53	981032.5994	-16.57	-18.83
29.7465547	-95.5232234	19.41	3281.54	981032.5994	-16.69	-18.9
29.7467221	-95.3078774	11.2	3288.65	981032.6242	-12.12	-13.41
29.7467213	-95.2852178	4	3290.22	981032.6242	-12.77	-13.25
29.7468881	-95.3080454	10.9	3288.65	981032.6489	-12.22	-13.48
29.7468873	-95.2848818	4.1	3290.22	981032.6489	-12.75	-13.25
29.7490566	-95.3505496	14.6	3287.28	981032.9719	-12.62	-14.3
29.750394	-95.2828827	10.4	3289.11	981033.1705	-12.19	-13.39
29.750562	-95.2830507	10.2	3289.11	981033.1956	-12.27	-13.45
29.7537282	-95.3482155	14.6	3287.28	981033.6674	-12.98	-14.66
29.7568931	-95.0885414	3	3287.5	981034.1392	-16.59	-16.96
29.7568931	-95.0885414	3	3289.5	981034.1392	-14.59	-14.96
29.758561	-95.3618799	16.7	3286.3	981034.3876	-13.69	-15.61
29.758561	-95.3618799	16.7	3286.3	981034.3876	-13.69	-15.61
29.7662282	-95.2227159	6.9	3292.47	981035.5303	-11.14	-11.96
29.7663942	-95.2227159	6.8	3292.47	981035.555	-11.19	-11.99
29.7702268	-95.2665481	10.9	3290.44	981036.1261	-12.25	-13.51
29.7702268	-95.2665481	11.1	3290.43	981036.1261	-12.2	-13.48
29.7703927	-95.1558801	7.4	3292.4	981036.1509	-11.38	-12.25
29.7705607	-95.1560401	7.5	3292.4	981036.1759	-11.37	-12.25
29.7708933	-95.3487184	14.8	3288.17	981036.2254	-13.37	-15.06
29.7715613	-95.3488784	14.5	3288.17	981036.3249	-13.51	-15.18
29.7815611	-95.3918865	16.2	3286.65	981037.8149	-15.29	-17.13
29.7815611	-95.3927185	15.8	3286.66	981037.8149	-15.4	-17.21
29.7828942	-95.409214	17.5	3285.76	981038.0135	-15.88	-17.86
29.7830602	-95.409717	17.3	3285.76	981038.0382	-15.95	-17.92
29.7832283	-95.4245494	16.8	3285.71	981038.0632	-16.17	-18.1
29.7832283	-95.4248844	16.3	3285.71	981038.0632	-16.33	-18.19
29.7833945	-95.4395488	18.9	3285.03	981038.0879	-16.22	-18.38
29.7835605	-95.4407159	18.5	3285.03	981038.1127	-16.35	-18.47
29.7842271	-95.5352245	24.91	3282.4	981038.212	-17.06	-19.9
29.7842278	-95.4870512	19.91	3284.29	981038.212	-16.71	-18.99
29.7842278	-95.4793829	20.81	3284.17	981038.212	-16.56	-18.93
29.7843931	-95.5335535	24.41	3282.41	981038.2368	-17.22	-20

Latitude	Longitude	Elevation (m)	Observed Gravity_ G_{obs} (mGal)	Theoretical Gravity_ G_n (mGal)	FAA (mGal)	Complete Bouguer Anomaly (mGal)
29.784393	-95.5265573	23.41	3283.04	981038.2368	-16.9	-19.57
29.7843938	-95.4872192	19.51	3284.3	981038.2368	-16.84	-19.07
29.7843938	-95.479887	20.31	3284.18	981038.2368	-16.71	-19.04
29.7843937	-95.4668856	19.71	3284.44	981038.2368	-16.64	-18.89
29.7845615	-95.5795518	27.71	3280.16	981038.2618	-18.46	-21.61
29.7845614	-95.5628893	22.01	3281.96	981038.2618	-18.42	-20.94
29.7847275	-95.5797198	27.21	3280.16	981038.2865	-18.63	-21.72
29.7847274	-95.5627213	21.51	3281.97	981038.2865	-18.58	-21.04
29.7847272	-95.5455548	25.41	3281.78	981038.2865	-17.57	-20.47
29.7848936	-95.5898901	28.01	3280.06	981038.3113	-18.5	-21.68
29.7848938	-95.4865551	25.91	3281.78	981038.3113	-17.42	-20.34
29.7852276	-95.5902181	27.51	3280.06	981038.361	-18.68	-21.8
29.7852275	-95.5857249	27.21	3280.1	981038.361	-18.73	-21.83
29.7852275	-95.5853889	27.71	3280.1	981038.361	-18.57	-21.73
29.785227	-95.5268853	23.91	3283.04	981038.361	-16.81	-19.54
29.7852276	-95.4668856	20.11	3284.43	981038.361	-16.59	-18.89
29.7883914	-95.0920433	8.3	3291.67	981038.8327	-13.24	-14.19
29.7885594	-95.0922113	8.2	3291.67	981038.8577	-13.28	-14.22
29.78906	-95.3123782	14.2	3290.29	981038.9322	-12.85	-14.48
29.789393	-95.3117152	14.5	3290.28	981038.9818	-12.79	-14.46
29.7932252	-95.3462161	15.5	3289.3	981039.5527	-13.76	-15.54
29.7932252	-95.3463841	15.5	3289.3	981039.5527	-13.76	-15.54
29.7967244	-95.2883835	13.5	3291.51	981040.0741	-12.44	-13.99
29.7990593	-95.2898785	13.2	3291.53	981040.4219	-12.7	-14.21
29.8000583	-95.3018798	14.6	3291.3	981040.5707	-12.57	-14.25
29.8002243	-95.3018798	14.6	3291.3	981040.5955	-12.58	-14.26
29.8043911	-95.0562072	9.6	3291.78	981041.2163	-13.97	-15.08
29.8043911	-95.0560392	9.5	3291.78	981041.2163	-14	-15.1
29.8048933	-95.4077178	19.8	3286.91	981041.2908	-15.73	-18
29.8052262	-95.4065507	20.2	3286.9	981041.3404	-15.65	-17.96
29.8063935	-95.1965459	9.5	3295	981041.5144	-10.94	-12.05
29.8065597	-95.5245501	26.71	3283.85	981041.5391	-16.79	-19.83
29.8068926	-95.5247181	26.91	3283.85	981041.5887	-16.76	-19.82
29.8078915	-95.2692098	13.4	3292.78	981041.7377	-12.07	-13.61
29.8080575	-95.2693778	13.3	3292.78	981041.7624	-12.12	-13.64

Latitude	Longitude	Elevation (m)	Observed Gravity_ G_{obs} (mGal)	Theoretical Gravity_ G_n (mGal)	FAA (mGal)	Complete Bouguer Anomaly (mGal)
29.8098939	-95.240546	13.1	3293.9	981042.0357	-11.2	-12.71
29.8098939	-95.240713	13.1	3293.91	981042.0357	-11.19	-12.7
29.8127252	-95.3502131	17.6	3289.67	981042.4575	-14.26	-16.28
29.813058	-95.2563774	11.5	3293.81	981042.5073	-12.03	-13.37
29.813392	-95.2565444	11.7	3293.8	981042.557	-12.01	-13.36
29.8177266	-95.2403779	11.3	3294.53	981043.2024	-11.74	-13.05
29.8177266	-95.2402099	11.1	3294.53	981043.2024	-11.8	-13.09
29.818226	-95.525885	27.11	3284.35	981043.2769	-17.08	-20.16
29.818226	-95.526053	26.41	3284.35	981043.2769	-17.3	-20.31
29.8183927	-95.4102207	22.6	3287.23	981043.3016	-15.6	-18.18
29.8188917	-95.4105487	22.2	3287.24	981043.3759	-15.75	-18.29
29.8193919	-95.4263872	22.6	3286.68	981043.4504	-16.23	-18.81
29.81956	-95.4370535	21.9	3286.76	981043.4754	-16.38	-18.88
29.819726	-95.4372135	21.5	3286.76	981043.5001	-16.51	-18.97
29.8198922	-95.4532209	20.31	3286.92	981043.5248	-16.74	-19.05
29.8198919	-95.4268832	23	3286.68	981043.5248	-16.15	-18.77
29.8205592	-95.4538849	20.51	3286.93	981043.6242	-16.72	-19.05
29.828226	-95.2195413	11.6	3295.12	981044.7662	-11.87	-13.22
29.828226	-95.2198773	11.3	3295.14	981044.7662	-11.94	-13.26
29.8300579	-95.5028893	26.61	3285.5	981045.0391	-17.01	-20.03
29.8307248	-95.2127131	12.6	3293.9	981045.1383	-12.98	-14.43
29.8363888	-95.2698816	13.1	3294.43	981045.9821	-12.74	-14.25
29.8365568	-95.2698816	13.4	3294.42	981046.0071	-12.67	-14.21
29.8365562	-95.056542	11.4	3294.85	981046.0071	-12.85	-14.16
29.8372222	-95.0577101	11.3	3294.85	981046.1063	-12.94	-14.24
29.8395566	-95.3340464	20.7	3291.1	981046.4537	-13.97	-16.34
29.841891	-95.1888774	12	3296.39	981046.8012	-11.54	-12.92
29.841891	-95.1883744	12.2	3296.39	981046.8012	-11.48	-12.89
29.8452227	-95.358217	20.9	3291.32	981047.2974	-14.13	-16.52
29.8452227	-95.358217	21	3291.31	981047.2974	-14.11	-16.51
29.8488905	-95.173542	12.1	3296.75	981047.8435	-11.7	-13.09
29.8490565	-95.17371	12.3	3296.74	981047.8682	-11.66	-13.08
29.852724	-95.532218	28.51	3285.82	981048.4144	-17.87	-21.12
29.852724	-95.5320499	29.11	3285.81	981048.4144	-17.69	-21
29.8540552	-95.059037	13.9	3295.71	981048.6128	-12.59	-14.18

Latitude	Longitude	Elevation (m)	Observed Gravity_ G_{obs} (mGal)	Theoretical Gravity_ G_n (mGal)	FAA (mGal)	Complete Bouguer Anomaly (mGal)
29.8543872	-95.058877	13.8	3295.72	981048.6623	-12.63	-14.22
29.855223	-95.1590455	12.5	3297.03	981048.7864	-11.79	-13.23
29.8565545	-95.2627092	16.2	3295.42	981048.9849	-12.36	-14.22
29.8565545	-95.2627092	16.3	3295.43	981048.9849	-12.32	-14.19
29.8597235	-95.1468762	13	3297.21	981049.4566	-11.81	-13.3
29.8602235	-95.1448782	13	3297.21	981049.531	-11.85	-13.34
29.8648886	-95.5502234	30.41	3286.31	981050.2255	-17.74	-21.2
29.8690557	-95.1253766	13.2	3297.78	981050.846	-11.9	-13.42
29.8693887	-95.1255446	13.1	3297.79	981050.8956	-11.95	-13.45
29.8752224	-95.364885	22.2	3293.1	981051.7639	-14.29	-16.82
29.8755564	-95.36638	22.1	3293.1	981051.8136	-14.34	-16.87
29.87822	-95.2583749	17.2	3297.1	981052.2104	-12.06	-14.03
29.8785546	-95.0968718	8.2	3298.9	981052.2601	-13.07	-14.02
29.8785546	-95.0968718	8.2	3300.9	981052.2601	-11.07	-12.02
29.8790538	-95.0615399	13.3	3298.14	981052.3346	-12.29	-13.82
29.8793878	-95.063539	13.1	3298.14	981052.3843	-12.38	-13.88
29.8807231	-95.5715559	33.91	3287.18	981052.5827	-17.03	-20.88
29.8807231	-95.5715559	33.21	3287.18	981052.5827	-17.24	-21.02
29.8810529	-95.2585429	16.9	3297.1	981052.6321	-12.38	-14.31
29.8915564	-95.2478765	16.3	3298.32	981054.195	-12.16	-14.03
29.8915564	-95.2480445	15.7	3298.33	981054.195	-12.34	-14.14
29.8968887	-95.5948875	36.21	3288.03	981054.9888	-16.73	-20.84
29.8968887	-95.5943915	35.71	3288.03	981054.9888	-16.88	-20.94
29.9023845	-95.0635389	14.9	3299.6	981055.8072	-12.16	-13.87
29.9023845	-95.0635389	14.9	3299.61	981055.8072	-12.15	-13.86
29.9040542	-95.37288	22.8	3294.46	981056.0553	-14.99	-17.6
29.9040542	-95.373048	22.7	3294.46	981056.0553	-15.02	-17.62
29.9087193	-95.0677039	13.7	3300.32	981056.7499	-12.3	-13.87
29.9090512	-95.0682079	13.7	3300.28	981056.7993	-12.37	-13.93
29.9145544	-95.6198891	39.41	3288.39	981057.6178	-16.76	-21.24
29.9147204	-95.6198891	39.11	3288.39	981057.6425	-16.86	-21.31
29.9168867	-95.3757189	23.4	3295.31	981057.9649	-14.96	-17.63
29.9198832	-95.0532075	15.5	3300.9	981058.4113	-12.04	-13.82
29.9213841	-95.0527045	15.4	3300.9	981058.6346	-12.19	-13.95
29.9248873	-95.5973894	38.81	3289.66	981059.1554	-16.48	-20.89

Latitude	Longitude	Elevation (m)	Observed Gravity_ G_{obs} (mGal)	Theoretical Gravity_ G_n (mGal)	FAA (mGal)	Complete Bouguer Anomaly (mGal)
29.9248844	-95.0718699	15	3301.47	981059.1554	-12.01	-13.74
29.9252193	-95.5967184	38.91	3289.66	981059.2048	-16.48	-20.9
29.9252164	-95.0718699	15.1	3301.47	981059.2048	-12.01	-13.74
29.9265552	-95.2115443	16.7	3301.25	981059.4034	-11.84	-13.75
29.9265552	-95.2115443	16.9	3301.26	981059.4034	-11.77	-13.71
29.9385538	-95.382379	24.2	3296.74	981061.1887	-14.97	-17.74
29.9398867	-95.3815469	24.1	3296.74	981061.387	-15.11	-17.86
29.9418866	-95.5705555	38.81	3291.06	981061.6847	-16.41	-20.82
29.9418866	-95.5698845	38.91	3291.06	981061.6847	-16.38	-20.8
29.9418846	-95.0752039	15.8	3303.08	981061.6847	-11.49	-13.3
29.9423835	-95.0752039	15.6	3303.08	981061.7589	-11.59	-13.38
29.9560485	-95.2665464	20.7	3300.1	981063.7917	-14.06	-16.43

APPENDIX C – PACES MAGNETIC DATASET

Latitude		Longitude		Total Intensity (nanoTesla)		Magnetic Station ID
29.664		-95.161003		-257.5		TEX70427
29.664		-95.177002		-252.33		TEX70426
29.664		-95.196999		-246.46		TEX70425
29.663		-95.216003		-240.61		TEX70424
29.663		-95.234001		-236.42		TEX70423
29.664		-95.25		-234.17		TEX70422
29.667		-95.266998		-233.25		TEX70421
29.669001		-95.280998		-232.95		TEX70419
29.67		-95.291		-232.82		TEX70418
29.67		-95.302002		-232.33		TEX70417
29.669001		-95.314003		-234.47		TEX70416
29.669001		-95.321999		-233.56		TEX71655
29.67		-95.331001		-237.73		TEX70415
29.669001		-95.348999		-243.07		TEX70414
29.669001		-95.362999		-246.68		TEX70413
29.669001		-95.378998		-249.28		TEX70412
29.667999		-95.396004		-253.35		TEX70411
29.653999		-95.321999		-239.95		TEX71654
29.639999		-95.321999		-247.78		TEX71653
29.639		-95.321999		-248.09		TEX71652
29.622999		-95.155998		-304.79		TEX70316
29.622999		-95.171997		-301.89		TEX70317
29.624001		-95.186996		-299.26		TEX70318
29.625		-95.202003		-296.31		TEX70319
29.624001		-95.218002		-293.39		TEX70320
29.628		-95.232002		-289.09		TEX70321
29.632999		-95.247002		-284.82		TEX70322
29.636		-95.262001		-273.9		TEX70323
29.638		-95.277		-262.1		TEX70324
29.638		-95.292		-258.47		TEX70325
29.635		-95.311996		-260.37		TEX70327
29.629999		-95.325996		-265.32		TEX70328
29.624001		-95.339996		-270.63		TEX70329

Latitude		Longitude		Total Intensity (nanoTesla)		Magnetic Station ID
29.618999		-95.353996		-276.69		TEX70330
29.613001		-95.367996		-279.35		TEX70331
29.613001		-95.384003		-284.22		TEX70332
29.612		-95.399002		-289.41		TEX70333
29.625		-95.322998		-260.71		TEX71651
29.610001		-95.322998		-284.27		TEX71650
29.594999		-95.322998		-308.24		TEX71649
29.579		-95.323997		-330.99		TEX71648
29.576		-95.152		-360.68		TEX70200
29.576		-95.170998		-357.44		TEX70199
29.575001		-95.188004		-355.25		TEX70198
29.575001		-95.205002		-354.51		TEX70197
29.575001		-95.223		-353.75		TEX70196
29.575001		-95.240997		-349.83		TEX70195
29.575001		-95.259003		-346.64		TEX70194
29.575001		-95.278		-345.63		TEX70193
29.576		-95.296997		-343.44		TEX70192
29.575001		-95.314003		-339.06		TEX70191
29.573999		-95.329002		-336.44		TEX70190
29.573999		-95.348		-334.45		TEX70189
29.575001		-95.362999		-333.44		TEX70188
29.575001		-95.377998		-331.71		TEX70187
29.575001		-95.382004		-331.43		TEX70186
29.575001		-95.399002		-331.77		TEX70185
29.563999		-95.323997		-341.71		TEX71647
29.549		-95.324997		-343.51		TEX71646
29.533001		-95.323997		-347.11		TEX71645
29.525		-95.142998		-379.11		TEX70087
29.525		-95.157997		-380.64		TEX70088
29.525		-95.164001		-380.77		TEX70089
29.525		-95.18		-380		TEX70090
29.525		-95.195		-378.18		TEX70091
29.525		-95.210999		-375.72		TEX70092
29.525999		-95.225998		-373.42		TEX70093
29.524		-95.241997		-368.4		TEX70094

Latitude		Longitude		Total Intensity (nanoTesla)		Magnetic Station ID
29.521		-95.257004		-363.26		TEX70095
29.521		-95.272003		-360.65		TEX70096
29.525999		-95.287003		-356.57		TEX70097
29.525		-95.302002		-350.6		TEX70098
29.525		-95.318001		-346.81		TEX70099
29.525999		-95.334		-345.79		TEX70100
29.525		-95.348999		-344.28		TEX70101
29.525		-95.364998		-343		TEX70102
29.525999		-95.379997		-342.03		TEX70103
29.525999		-95.396004		-341.09		TEX70104
29.518999		-95.324997		-352.71		TEX71644
29.504		-95.325996		-359.31		TEX71643
29.492001		-95.325996		-362.07		TEX71642
29.476999		-95.324997		-365.97		TEX71641
29.476999		-95.141998		-401.87		TEX70060
29.476999		-95.157997		-402.32		TEX70059
29.476999		-95.162003		-402.3		TEX70058
29.475		-95.181999		-401.7		TEX70057
29.473		-95.198997		-397.25		TEX70056
29.473		-95.217003		-388.82		TEX70055
29.473		-95.232002		-381.09		TEX70054
29.473		-95.247002		-377.02		TEX70053
29.473		-95.267998		-373.95		TEX70052
29.472		-95.289001		-370.74		TEX70051
29.472		-95.306999		-368.24		TEX70050
29.472		-95.320999		-366.08		TEX70049
29.472		-95.338997		-364.41		TEX70048
29.472		-95.356003		-362.94		TEX70047
29.472		-95.372002		-360.65		TEX70046
29.474001		-95.389999		-359.92		TEX70045
29.462999		-95.325996		-373.57		TEX71640
29.448		-95.325996		-381.03		TEX71639
29.437		-95.149002		-417.52		TEX69943
29.437		-95.18		-413.19		TEX69945
29.437		-95.195		-409.08		TEX69946

Latitude		Longitude		Total Intensity (nanoTesla)		Magnetic Station ID
29.437		-95.209999		-406.34		TEX69947
29.437		-95.225998		-402.23		TEX69948
29.437		-95.240997		-398.7		TEX69949
29.437		-95.255997		-396.16		TEX69950
29.437		-95.271004		-391.83		TEX69951
29.437		-95.302002		-385.78		TEX69953
29.437		-95.317001		-383.29		TEX69954
29.437		-95.333		-380.58		TEX69955
29.437		-95.348999		-379.28		TEX69956
29.437		-95.352997		-379.22		TEX69957
29.437		-95.367996		-380.29		TEX69958
29.437		-95.384003		-381.39		TEX69959
29.436001		-95.165001		-415.36		TEX69944
29.436001		-95.287003		-387.91		TEX69952
29.433001		-95.327003		-382.86		TEX71638
29.417999		-95.327003		-382.6		TEX71637
29.417		-95.327003		-382.45		TEX71636
29.402		-95.328003		-378.97		TEX71635
29.388		-95.142998		-412.77		TEX69903
29.389		-95.160004		-409.97		TEX69902
29.388		-95.178001		-407.45		TEX69901
29.388		-95.195999		-404.03		TEX69900
29.388		-95.212997		-400.44		TEX69899
29.388		-95.230003		-397.5		TEX69898
29.386999		-95.248001		-394.79		TEX69897
29.386999		-95.271004		-389.53		TEX69896
29.386999		-95.288002		-386.25		TEX69895
29.386999		-95.307999		-385.83		TEX69894
29.386999		-95.324997		-383.94		TEX69893
29.386999		-95.342003		-380.05		TEX69892
29.386999		-95.361		-377.37		TEX69891
29.386999		-95.375		-377.24		TEX69890
29.386999		-95.386002		-376.63		TEX69889
29.372999		-95.328003		-379.06		TEX71633
29.358		-95.328003		-385.39		TEX71632

Latitude		Longitude		Total Intensity (nanoTesla)		Magnetic Station ID
29.344999		-95.143997		-417.55		TEX69792
29.344		-95.158997		-416.17		TEX69793
29.344999		-95.175003		-414.61		TEX69794
29.344		-95.190002		-412.54		TEX69795
29.344		-95.206001		-409.08		TEX69796
29.344		-95.221001		-407.47		TEX69797
29.344		-95.236		-404.27		TEX69798
29.344		-95.251999		-400.79		TEX69799
29.343		-95.266998		-397.68		TEX69800
29.341999		-95.282997		-396		TEX69801
29.341999		-95.297997		-395.2		TEX69802
29.341999		-95.314003		-395.13		TEX69803
29.341999		-95.319		-395.44		TEX69804
29.341999		-95.334999		-397.08		TEX69805
29.341999		-95.349998		-397.17		TEX69806
29.341999		-95.365997		-397.51		TEX69807
29.341999		-95.369003		-397.4		TEX69808
29.341999		-95.385002		-396.12		TEX69809
29.327999		-95.329002		-389.72		TEX71630
29.323999		-95.329002		-388.1		TEX71629
29.308001		-95.330002		-382.75		TEX71628
29.302		-95.143997		-420.07		TEX69747
29.302		-95.165001		-414.67		TEX69746
29.302999		-95.183998		-410.91		TEX69745
29.302999		-95.199997		-407.84		TEX69744
29.304001		-95.216003		-405.15		TEX69743
29.304001		-95.233002		-401.81		TEX69742
29.299		-95.271004		-393.57		TEX69740
29.299		-95.288002		-391.68		TEX69739
29.299		-95.339996		-389.79		TEX69736
29.299		-95.353996		-389.93		TEX69735
29.299		-95.367996		-388.55		TEX69734
29.299		-95.383003		-385.34		TEX69733
29.299999		-95.252998		-397.07		TEX69741
29.299999		-95.304001		-390.37		TEX69738

Latitude		Longitude		Total Intensity (nanoTesla)		Magnetic Station ID
29.299999		-95.321999		-389.97		TEX69737
29.292999		-95.330002		-384		TEX71627
29.275999		-95.330002		-393.83		TEX71626

VITA

Francis Chiedu Okocha graduated from high school in 2002 and he earned a B.Sc. degree in Geology in 2006 from the University of Benin, Benin City, Edo State, Nigeria. After completion of his national youth corps service in 2007 with Oceanic Bank International PLC (now Ecobank Nigeria ltd), he was retained and employed as an officer of the bank in 2008. Francis has 5 years working experience in financial service and customer relationship. He enrolled for graduate school in geology at Stephen F. Austin State University in Nacogdoches, Texas, U.S.A., in the fall of 2014 and he was employed as a graduate teaching assistant at the department in 2015. Francis received a M.Sc. degree in May 2017 having satisfied his requirements for a master's degree.

Permanent Address: 3100 North Pecan Street
Nacogdoches, 75965, Texas

Style manual designation: Geological Society of America

This thesis was typed by Francis C. Okocha